Universität Rostock Traditio et Innovatio

INSTITUT FÜR PHYSIK

Imaging and motion detection at the nanometer scale: a data-driven approach

KUMULATIVE DISSERTATION

zur Erlangung des Akademischen Grades

Doctor rerum naturalium (Dr. rer. nat.)

der Mathematisch-Naturwissenschaftlichen Fakultät
der Universität Rostock

Vorgelegt von:	Andrii Trelin
Geboren am::	09.03.1998
Betreuer:	Prof. Dr. Friedemann Reinhard
Abgabedatum:	12.12.2024

https://doi.org/10.18453/rosdok_id00005764

Gutachter:
Dr. Dmitry Postnov, Aarhus University, Department of Clinical Medicine
Prof. Dr. Oliver Otto, Universität Greifswald, Institut für Physik
Jahr der Einreichung: 2024
Jahr der Verteidigung: 2025

Abstract

This doctoral thesis explores the potential of data-driven methodologies in physics, specifically for small signal detection. The work comprises two distinct applications: non-invasive optical detection of neuronal action potentials and nanoscale tomography of nitrogen-vacancy centers in diamonds, which have significant implications for fields ranging from neuroscience to quantum computing.

The main part of this work proposes ChiSCAT, an optical scheme combining interferometric sensitivity to cellular motions with high-NA illumination, supporting high-speed recording, but producing no interpretable image. This issue is resolved by the proposed ChiSCAT algorithm, which relies on data-driven techniques to extract the membrane motion signals associated with action potentials in electrically active cells. This approach has been experimentally validated on human iPSC-derived cardiomyocytes, successfully detecting action potentials in 71% of experiments. A continuation of this work involves a detailed experimental and theoretical analysis of the ChiSCAT scheme using human iPSC-derived neurons, determining exact detection limits and identifying potential directions for future research. Additionally, the measured data from cardiomyocytes and neurons have been published in open-source repositories, facilitating the development of improved algorithms.

The secondary part of the project focuses on the optimization of 3D nanoscale spin tomography for NV centers in diamonds. The research introduced a new approach to data collection and processing that exploits known signal structures to accelerate the measurements. This method resulted in a tenfold reduction in data collection time, thereby reducing errors from slow setup drift during experiments.

This work demonstrates the potential of integrating data-driven methods in experimental physics. It highlights how these approaches can contribute to scientific progress in different areas by overcoming specific limitations, such as when an exact signal model is unknown. The thesis advocates the use of sophisticated data processing to effectively utilize data previously considered uninterpretable, emphasizing the importance of interdisciplinary interplay between data processing and experimental design.

Zusammenfassung

Diese Doktorarbeit untersucht das Potenzial datengetriebener Methoden in der Physik, insbesondere für die Erkennung schwacher Signale. Die Arbeit umfasst zwei verschiedene Anwendungen: die nicht-invasive optische Detektion neuronaler Aktionspotenziale und die nanoskalige Tomographie von Stickstoff-Fehlstellen-Zentren (NV-Zentren) in Diamanten, die bedeutende Auswirkungen auf Bereiche wie Neurowissenschaften und Quantencomputing haben.

Der Hauptteil dieser Arbeit schlägt ChiSCAT vor, ein optisches Verfahren, das interferometrische Empfindlichkeit gegenüber Zellbewegungen mit hochnumerischer Apertur (high-NA)-Beleuchtung kombiniert und die Aufnahme mit hoher Geschwindigkeit unterstützt, jedoch kein interpretierbares Bild erzeugt. Dieses Problem wird durch den vorgeschlagenen ChiSCAT-Algorithmus gelöst, der auf datengetriebenen Techniken basiert, um die Membranbewegungssignale zu extrahieren, die mit Aktionspotenzialen in elektrisch aktiven Zellen assoziiert sind. Dieser Ansatz wurde experimentell an menschlichen, aus iPS-Zellen abgeleiteten Kardiomyozyten validiert, wobei in 71 % der Experimente erfolgreich Aktionspotenziale detektiert wurden. Eine Fortsetzung dieser Arbeit umfasst eine detaillierte experimentelle und theoretische Analyse des ChiSCAT-Verfahrens unter Verwendung von aus iPS-Zellen abgeleiteten menschlichen Neuronen, um die genauen Detektionsgrenzen zu bestimmen und potenzielle Forschungsrichtungen für die Zukunft zu identifizieren. Zusätzlich wurden die gemessenen Daten von Kardiomyozyten und Neuronen in Open-Source-Repositories veröffentlicht, um die Entwicklung verbesserter Algorithmen zu fördern.

Der sekundäre Teil des Projekts konzentriert sich auf die Optimierung der dreidimensionalen nanoskaligen Spin-Tomographie für NV-Zentren in Diamanten. Die Forschung führte einen neuen Ansatz zur Datenerfassung und -verarbeitung ein, der bekannte Signalstrukturen nutzt, um die Messungen zu beschleunigen. Diese Methode führte zu einer zehnfachen Reduktion der Datenerfassungszeit und verringerte somit Fehler, die durch langsames Driftverhalten der Apparatur während der Experimente entstehen.

Diese Arbeit zeigt das Potenzial der Integration datengetriebener Methoden in die experimentelle Physik. Sie verdeutlicht, wie solche Ansätze wissenschaftlichen Fortschritt in verschiedenen Bereichen fördern können, indem spezifische Einschränkungen überwunden werden, etwa wenn ein genaues Signalmodell unbekannt ist. Die Dissertation plädiert für die Anwendung fortschrittlicher Datenverarbeitung, um Daten effektiv zu nutzen, die zuvor als nicht interpretierbar galten, und betont die Bedeutung der interdisziplinären Verzahnung von Datenverarbeitung und experimentellem Design.

Contents

1 Introduction **1**

1.1 Small signal detection: a historical remark 1

1.2 Data driven signal detection: achievements and challenges 2

1.3 Detecting small signals: utilizing a priori information 4

2 Label-free action potential detection **8**

2.1 Intrinsic optical signals 8

2.2 Origin of IOS: membrane motion 9

2.3 Optical AP detection 11

2.4 Optical setup and algorithms for reflected-light phase-sensitive microscopy 14

2.5 Paper: "*ChiSCAT: Unsupervised Learning of Recurrent Cellular Micromotion*" 15

2.6 Paper: *"When can we see micromotion? Experimental and theoretical analysis of the ChiSCAT scheme"* 18

3 Localizing NV centers from intensity oscillations **20**

3.1 A short outlook of the field 20

3.2 3D magnetic resonance tomography: the signals observed 21

3.3 Algorithms to improve SNR / reduce time 23

3.4 Paper: *"Three-dimensional magnetic resonance tomography with sub-10 nanometer resolution"* 26

4 Conclusion **27**

5 Published articles **29**

5.1 ChiSCAT: Unsupervised Learning of Recurrent Cellular Micromotion 29

5.2 *When can we see micromotion? Experimental and theoretical analysis of the ChiSCAT scheme* 50

5.3 Three-dimensional magnetic resonance tomography with sub-10 nanometer resolution 62

5.4 Author contributions to individual articles 74

References **76**

Nomenclature

AP Action Potential

BSS Blind Source Separation

DSP Digital Signal Processing

ECG Electrocardiogram

EEG Electroencephalogram

ESR Electron Spin Resonance

ICA Independent Component Analysis

IOS Intrinsic Optical Signals

iPSC Induced Pluripotent Stem Cell

iSCAT Interferometric Scattering Microscopy

ML Machine Learning

MRFM Magnetic Resonance Force Microscopy

MRI Magnetic Resonance Imaging

NA Numerical Aperture

NMF Non-negative Matrix Factorization

NMR Nuclear Magnetic Resonance

NN Neural Network

PCA Principal Component Analysis

QPI Quantitative Phase Imaging

SNR Signal-to-Noise ratio

1 Introduction

1.1 Small signal detection: a historical remark

The small signal detection problem, i.e. observing tiny changes in some observable value, has been present in science since ancient times. One of the earliest examples of this problem is stellar observation, where minuscule changes in the angles of stellar bodies were detected as early as the 1st century AD [58]. For millennia, precise measurements relied on the human eye as the observation device, leading to the invention of increasingly complex machinery to make the changes easier to observe. Historical examples include, for instance, Galileo observation of Jupiter's moons [59] using a telescope, Cavendish experiment for measuring the gravitational constant [196] using a torsion balance, and the Michelson–Morley experiment [162] using a Michelson interferometer. The discovery of electromagnetic waves by Hertz [76] led to the creation of the first detection devices even for creating general physics-informed foundation models [107], similar to foundation models in language processing [33]. [54] that did not directly rely on human vision and opened the epoch of radio. However, decoding of the signal was still performed by humans. Advances in radio technology in the early 20th century, especially the invention of radar technology in the 1930s fueled by World War II, led to the creation of automatic signal detection systems and laid the foundation for modern signal detection theory [119]. Around the same period, the theoretical works of Fisher [52], and later Wiener [198] and Shannon [163], established a solid theoretical framework for understanding signal detection problem. Practical implementations, however, still mostly relied on analog detectors.

The digital revolution of the 1950s and 1960s fundamentally changed the approach to signal detection by transferring it from the realm of electrical engineering to the use of computers. The area of digital signal processing (DSP) was theoretically justified by the Nyquist-Shannon theorem [134, 164] and enabled previously impossible signal processing approaches, such as very high-order filtering [103] or fast numerical computation of the Fourier transform of arbitrary signal [37]. This facilitated the effective implementation of matched filtering, an optimal linear signal detection technique [133], which, together with the increasing availability of computing hardware, made optimal signal detection accessible to many researchers, leading to e.g. breakthroughs in radio astronomy [77] and other fields.

The increase in available computing power in the late 1970s and 1980s led to the development and widespread use of numerically more expensive methods capable of working with more complex data. Examples include wavelet transform [60], adaptive filtering [197], and Kalman filtering [91]. In the following decade, multidimensional signal processing, including principal component analysis (PCA, known since the

1930s) [82], non-negative matrix factorization (NMF) [138], and independent component analysis (ICA) [6], as well as other methods for blind source separation (BSS), became popular and revolutionized the processing of multidimensional biological signals, such as electrocardiograms (ECG) and electroencephalograms (EEG) [116, 203, 89]. The development of the backpropagation algorithm [156] opened doors for effective training of neural networks and, consequently, signal detection with neural networks (NNs) [99, 84, 26], bringing nonlinear approaches to signal processing. Another family of nonlinear methods invented in the 1990s is based on the kernel trick, including kernel PCA [123], kernel discriminant analysis [161], and kernel ICA [9].
The 2000s were characterized by increased usage of machine learning (ML) methods [95, 27] as well as the invention of compressed sensing, a method that allows full signal reconstruction with much smaller amounts of data collected [112, 124, 41]. Starting from the 2010s, the main research interest centered around deep learning for signal detection [202, 152, 146], achieving impressive results, for example, in detecting gravitational waves [205, 56, 55]. This area remains a topic of active investigation at the time of writing; however, the impressive success of transformer-based ML models [190], including their application in speech recognition [69] in the early 2020s, brought the idea of using transformers for signal processing [74], or even for creating general physics-informed foundation models [107], similar to foundation models in language processing [33].

1.2 Data driven signal detection: achievements and challenges

As mentioned above, modern signal processing methods are frequently data-driven, i.e., utilizing statistical or ML techniques to exploit properties of the data. These methods rely on available samples or the structure of the data itself instead of making strong assumptions about the exact data model. This allows for more effective pattern extraction even from data with complex noise, where linear methods are suboptimal [102]. Data-driven approaches effectively tackle complex and multidimensional data where a single analytical model is complicated or impossible [106]; adapt to non-stationary processes [139]; and integrate heterogeneous data from different sources [68]. Despite their power, the adaptation of data-driven approaches in the natural sciences is frequently connected with significant difficulties. Many data-driven approaches are data-hungry, as their name suggests, which is often problematic due to costly and time-consuming experiments. Large-scale ML approaches, such as foundation models, require a nontrivial amount of computational resources. The power of complex ML models usually comes with difficulties in interpretability [66], which questions the correctness and robustness of results obtained with them.

Finally, models trained on a small amount of data frequently cannot generalize to data collected under slightly different conditions [24]. However, the number of fields revolutionized by introducing data-driven signal detection is constantly growing, some examples of which are summarized below.

Gravitational wave detection Gravitational wave detection is arguably one of the largest triumphs of physics in the 21st century [2], made possible due to significant advances in measurement setups and data processing over the last decades. Despite advancements in experimental methods, gravitational wave signals are still extremely weak, requiring complicated data processing based on matched filtering [122]. While theoretically optimal in this specific case, the matched filtering approach is very computationally heavy, strongly complicating real-time detection. Incorporation of ML as an intermediate filter selecting potential candidate events has allowed for a significant increase in system throughput [55]. Moreover, replacing the existing matched filtering framework with an end-to-end ML model [57], demonstrated the same sensitivity as matched filtering while being much more computationally effective and resilient to artifacts (or *glitches* in jargon). Although true gravitational wave events are extremely rare, the theory predicts the exact shape of gravitational wave signals, allowing us to train ML models with simulated data injected into experimental noise and artifacts. Another data-driven approach employs ML to detect and classify glitches, providing a better understanding of their causes [205].

Nitrogen-vacancy (NV) centers in diamonds hold significant potential for room-temperature quantum computing [140], as well as magnetic [121] and electric [46] field sensing with unprecedented spatial resolution on the order of the size of a single atom. Moreover, the difference in fluorescence for different quantum states allows for reading out the NV center state by simple fluorescence intensity measurement. However, measurements, such as magnetic field quantification, require repeating and averaging the experiment hundreds of thousands of times to achieve a sufficient signal-to-noise ratio due to the fundamentally weak optical signal of the single NV, which limits the practical applications of this technology. Over the last year, several data-driven approaches have been applied to this problem, including a decrease in spin readout error [110, 147] by optimizing binning, detection of very weak nuclear magnetic resonance (NMR) signals [4] with accuracies exceeding Bayesian detection, and reconstruction of the magnetic field from optically-detected magnetic resonance (ODMR) [185]. Interestingly, the authors of the latter two articles declare that "blind" ML methods were found to be superior to relying on exact physical models of the system. Another branch of research is employing compressive sensing, a data-driven method allowing a significant reduction in the amount of data

required to reconstruct a sparse signal. Examples include compressive reconstruction of nanoscale NMR spectra [145], 2D magnetic field imaging [7], and combining compressed sensing with ML for a ten-fold acceleration of 2D NMR signal [200].

Label-free detection of action potentials (APs) in neurons by measuring tiny changes in optical properties, occurring when an action potential is fired, known as intrinsic optical signals [34, 35, 168]. Despite the successful detection of that signal in crustacean neurons since the 1960s, detection of propagating AP in cultured mammalian neurons has only been achieved in 2018 [108, 199]. In both cases, a data-driven approach and complicated averaging schemes have been employed due to the extreme weakness of the signal: in [108] the authors developed a self-reinforcing lock-in algorithm to detect the sign of the pixel before averaging (since the change in cell thickness can be either positive or negative in different cell locations); the authors of [199] used semi-automatic edge detection to average the signal along cell boundaries and axons where the sign of the signal change is known.
Two latter examples are listed here for a reason: both hold significant potential for improvement by applying more advanced data-driven approaches, and the progress in these areas would lead to very important practical implications. Successful detection of APs by combining non-invasive microscopy with advanced signal processing would open the door for chronical observation of neuron activity, potentially helping in understanding the neuronal communication, and, in turn, consciousness. Application of this technique *in vivo* can lead to non-invasive brain-computer interface, solving a decades-old challenge [131]. Improvements in collecting data from NV centers would assist in creating ultra-miniaturized sensors of electric and magnetic fields, nanoscale NMR (potentially down to a single molecule) and MRI, and potentially pave the way towards quantum computing. That is the main motivation for this PhD project to be focused on this two problems.

1.3 Detecting small signals: utilizing a priori information

When the SNR in the observed data is low, it is challenging to determine whether a signal is present in the measurements. However, if additional information about the data and/or noise is available, it may be possible to enhance the SNR to a level at which the signal can be reliably detected. If one knows nothing about the properties of signal and noise there is no other way to recover it than to improve the measurement until sufficiently high SNR is reached. This might also mean multiple averages of the signal, since the observation noise is frequently independent and zero centered, thus by the law of large numbers average will converge to the true signal [171]. However, when more information about signal or noise properties are available, reliable small signal detection without averaging might be possible. An

outlook of how information about signals can be used is given below, focusing on the time series signals, being most relevant to the above-mentioned problems.

1D signals are very abundant, rather straightforward to process and have numerous real-life applications, which made them the main focus of research for decades. The simplest example of weak signal detection is frequency filtering: when both noise and signal spectra are known and significantly different, one can selectively suppress noise-containing frequencies [169]. As soon as exact signal shape is known, under moderate assumptions about noise properties (independence and zero-center) matched filtering provides optimal linear signal detection [133]. If the signal properties are known up to a constant (for example, it is known that the signal is Gaussian wavepacket, but it's exact scale and frequency are not known) the optimal signal detection is still achievable by brute force, usually implemented as bank of templates covering the parameter space [137]. Instead of using discrete bank of templates, wavelet transform can be used to convert the signal to time-frequency space [5]. When sparsity of the signal is assumed the similar idea of matching a signal against a bank of predefined templates (called *dictionary* in this context) allows to quickly find minimal sparse representation of the signal, known as matching pursuit [117] or its extensions [47, 182]. Sparse dictionary learning algorithms [51, 3] does not require predefined dictionary but uses data-driven approach to builds automatically. Both approaches are tightly connected to compressive sensing [12], a method that utilizes signal sparseness to recover the signal from highly undersampled data. When physical model of the signal generating system (both linear t[90] or nonlinear [88, 191]) is available, Kalman filter can be used to perform optimal real-time signal filtering as well as estimation of hidden system parameters.

Multidimensional signals are playing increasing role over the last several decades. Examples of multidimensional signals include e.g. networks of weather sensors at different geographical locations [136], detected signals in particle physics [16, 166], radio telescope arrays data in astrophysics [187], sensor arrays in analytical chemistry [44, 11], electroencephalogram data [159], or videos. All of the listed above methods for 1D signal processing can be applied to individual components of multidimensional signal, however, this is frequently suboptimal. Majority of the methods have been generalized to multidimensional case, including multidimensional Fourier [120] and wavelet [87] transforms, matching pursuit [48], sparse dictionary learning [207], and compressed sensing [21]. Special methods have been developed for processing multidimensional data, such as PCA [25], that exploits differences in explained variance by different components of multidimensional signal. When the signal is spatially sparse (e.g. when only some of the sensors generate relevant data), sparseness-informed version of PCA can be applied [208]. Knowledge that

multidimensional signal is a linear combination of smaller number of indpendent non-Gaussian true signals can be used by ICA [100] to find solution to BSS problem, i.e. to recover true signals. When additional properties of the signals are known, e.g. smoothness or temporal sparsity, corresponding versions of ICA can exploit this properties [31]. If non-negativity of the signal is given and small number of true signals is expected (similar to ICA case), NMF can recover them [45]. Finally, when signal contains spatial patterns, like for the case of video, classical computer vision algorithms [183] or vision ML models [22] can detect them and extract from the video. When both spatial and temporal patterns are expected ML approaches can learn their extraction given that enough training data is available [127].
Summary of algorithms making use of a priori information is given in the Table 1.

Technique	Domain	Required of a priori Information	References
Frequency Filtering	1D / ND	Known signal and noise spectra	[169]
Matched Filtering	1D	Known exact signal shape	[133]
Template Bank	1D	Known signal shape (up to parameters), parameters range	[137]
Fourier / Wavelet Transform	1D / ND	Periodicity / specific time-frequency relation	[5]
Matching Pursuit	1D / ND	Sparse representation of signal from predefined dictionary exists	[117, 48]
Sparse Dictionary Learning	1D / ND	Sparse representation of signal exists	[51, 3, 207]
Kalman Filter	1D / ND	Known physical model of the system	[90, 88, 191]
Fourier and Wavelet Transforms	ND	Periodicity / specific time-frequency relation	[120, 87]
PCA	ND	Observed signal is mixture of true signals, variance significantly differs	[25]
Sparse PCA	ND	True signals are concentrated on small subset of observed signals	[208]
ICA	ND	Independent non-Gaussian signals	[100]
Extended ICA	ND	Independent non-Gaussian signals, signal smoothness, temporal sparsity, etc	[31]
NMF	ND	Observed signal is mixture of true signals, non-negativity	[45]
Computer Vision and ML	Video	Spatial patterns are present	[183, 22]
Spatiotemporal ML	Video / ND	Spatiotemporal patterns are present	[127]

Table 1: Comparison of signal processing techniques employing a priori information

2 Label-free action potential detection

2.1 Intrinsic optical signals

Intrinsic optical signals (IOS), a minuscule changes in cellular optical properties during AP propagation, show significant potential for label-free, non-invasive detection of action potentials, making them well-suited for chronic observation of neuronal communication. The first observations of optical properties changing during AP firing were reported as early as the late 1940s [78], just 10 years after the very first modern measurement of AP [79]. In their experiments, the authors were able to measure a slow (on the order of 1 minute) change of opacity (scattering) after electrical stimulation of the nerve trunk of the walking leg of the shore crab, consisting of hundreds of axons. Two decades later, action potentials (with timescales of 1-10 ms) were detected in the crab nerve trunk as well as in single squid giant axons by observing changes in light scattering and birefringence [34]. Several years later, another report was published, combining scattering intensity measurements with voltage clamping, analyzing the correlation between potential, current, and the optical signal, concluding that IOS is highly correlated with action potential [35, 36]. Another decade later, a conclusive demonstration of the microscale motion of the membrane during AP firing was published [86]. Soon afterwards, theoretical models explaining this phenomenon were created, suggesting the presence of piezoelectric [67] or ferroelectric [105] behavior of the neuronal membrane. Approximately at the same time, experimental evidence for the pressure increase inside the axon was presented [172, 176], with some even demonstrating a direct relation between membrane potential and pressure [177]. A review article published as early as 1986 [192] compiled evidence about mechanical, thermal, and several kinds of optical (changes in scattering, birefringence, and optical rotation) intrinsic signals. It is important to note that all of the above-mentioned works used non-myelinated invertebrate nerves, which allow direct observation/measurement of the axonal membrane, impossible for myelinated axons.

In 1991, Stepnoski et al. reported [168] AP detection from IOS of a cultured sea hare neuron. Although this work was one of the first not using giant crab or squid axons, the diameter of the axon used in experiments (4-6 µm) was still significantly larger than vertebrate axons (approximately 1 µm). However, several years earlier, the first observation of IOS in mouse nerve terminals had been published [158]. Interestingly, another article, investigating IOS in the rat brain [64] reports that IOS had been so strong it interfered with voltage dye measurements. Another observation of IOS in rat brain slices was reported several years later [115], followed by multiple similar reports in the 1990s [80, 179, 142] and 2000s [149, 148, 186], although none of them dealt with single cells. The situation changed only in 2012

when the recently developed quantitative phase imaging (QPI) [143] was applied to the membrane potential detection problem [135]. The authors clearly demonstrated QPI-detected propagation of electric potential through the cell membrane and between the cells, however, an external signal was applied instead of spontaneous neuronal electrical activity. In a 2017 article, Batabyal et al. [13] reported the first IOS-based optical measurement of AP in cultured mammalian neurons by analyzing changes in the white light interference pattern between two coverslides, with neurons placed between them. In 2018, two articles simultaneously reported the detection of individual APs in mammalian neuron cultures using QPI [108, 199] combined with advanced data processing algorithms. A follow-up article reported the exact measurement of neuron membrane deformation with interferometric microscopy [109]. The most up-to-date study, at the time of writing this thesis, has achieved transcranial detection of AP in groups of neurons (similar to IOS detection in tissues described in the 1990s) with a phase-sensitive optical scheme [101].

2.2 Origin of IOS: membrane motion

Despite numerical experimental evidence of the existence of optical, mechanical, and thermal changes [1, 174, 173], a generally accepted theory of the non-electrical aspects of AP is still missing. Moreover, it is unclear if IOS can be explained by a purely mechanical increase in cell thickness, causing increase in optical thickness and changes in light scattering pattern, or if other purely optical changes (e.g. birefringence) are present as well. Taking into account that the most successful AP measurements in cultured mammal neurons [108, 199, 109] rely exclusively on the changes in neuron thickness, the focus of this outlook will be on mechanical effects. However, this does not mean that other components of IOS, such as birefringence changes, do not hold potential for label-free AP detection.

Electromechanical membrane movement

One of the earliest explanations for the change of axon thickness during AP propagation was given in 1980 [86], focusing on water uptake by the axon followed by its release; however, no mathematical model for this hypothesis has been developed. A later article [67] presented simple calculations that rendered the water uptake theory improbable and suggested a different mechanism for membrane movement based on electrostrictive and piezoelectric properties of the membrane. The former model, based on the fact that all dielectrics slightly elongate in electric field, predicted a motion amplitude of 2-10 Å, while the latter model, assuming piezoelectric behavior of the membrane (later experimentally demonstrated [73]) predicted motion as large as 6 µm, which is orders of magnitude larger than any experimental evidence. An-

other model [104] proposed electrodiffusion (viewing total ionic flux as the sum of diffusive and electromigrational components described by the Nernst-Planck equation) as the primary mechanism for AP propagation. This model is based on the observation that, by combining the Nernst-Planck equation with Gauss's law of electrostatics and applying suitable boundary conditions, one arrives at an equation having nonlinear wave solutions. Although these solutions are similar to AP, they are not sufficiently consistent with experimental data. This motivated the authors to assume the presence of ferroelectric units in the neuron membrane [105], i.e. some components that have spontaneous electric polarization, which could explain electromechanical and thermal effects of AP propagation as well as birefringence change by simple analogies with behavior of macroscopic ferroelectrics. For example, both ferroelectrics and neurons exhibit current-voltage hysteresis, and the birefringence of both is sensitive to electric fields. Unfortunately, the authors did not present a mathematical description of this model. Zhang et al. [206] proposed a thermodynamic model, based on the Lippmann equation, that quantifies surface tension change under applied electrical potential, viewing surface tension as a source for membrane stability, and proved its validity experimentally (direct measurement of membrane tension was performed later [128]). A different explanation [75] was proposed in 2005, treating action potential as soliton propagation, supported by membrane nonlinearities in the vicinity of phase transition, thus viewing AP propagation as a mechanic-thermodynamical phenomenon. This theory explains both the heat effects and change in the axon diameter, which fits well with the experimentally observed values. A 2011 article [157] views AP as the propagation of both electric and mechanical waves, caused by contraction of actin-myosin filaments, but focuses on predicting the velocity of propagation rather than amplitude. The work of Griesbauer et al. [61] experimentally demonstrated the propagation of AP-like pressure pulses in lipid monolayers, suggesting that the same mechanisms can exist in cells. Flexoelectricity, i.e., change of membrane curvature under applied potential in liquid crystal systems, has been proposed as a potential mechanism for the electromechanical component of AP too [129, 29], successfully matching the experimental values of membrane motion. El Hady and Machta proposed a model [50], viewing AP as mechanical waves co-propagating with electrical waves, similarly to [157], but focusing on potential-induced change of membrane tension as a source of the mechanical wave instead of actin-myosin contraction. The model explains both mechanical and thermal aspects of AP and predicts significant ($\approx$ 50 nm) lateral displacement of axoplasm, which has not been measured experimentally.

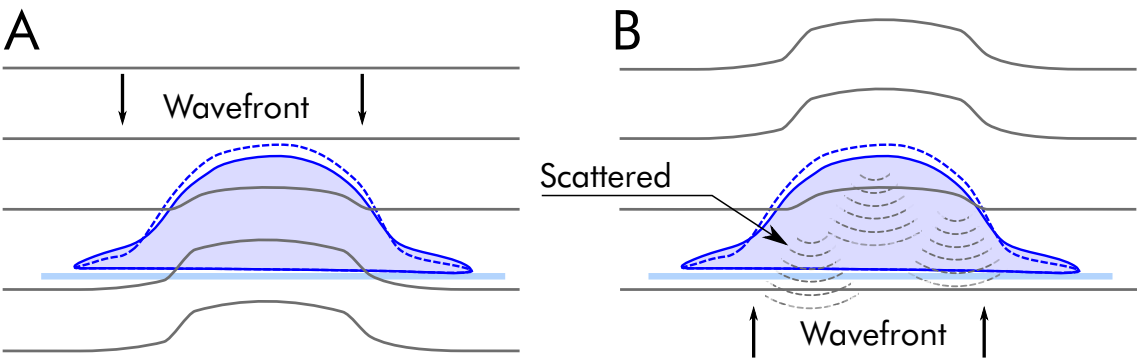


Figure 1: Comparison of transmission (A) and reflection (B) microscopy for observing tiny changes in the cell. In transmission geometry, wavefront accumulates phase delay as it passes trough the cell, thus directly bearing information about cell optical thickness. In reflection geometry, the light reflected/scattered from every point inside the cell leading to uninterpretable speckle-like pattern.

2.3 Optical AP detection

Assuming that membrane motion is the dominant mechanism for IOS, label-free AP detection can be achieved by choosing an optical scheme sensitive enough to detect these motions. Taking into account the fact that the majority of mammalian cells have negligible absorbance [98], phase-sensitive microscopy is required. Since the membrane motion amplitude is on the order of 1 nm [192, 94, 108, 109], this necessitates an extremely sensitive microscopy scheme. The action potential occurs on the timescale of 1 ms, which implies the use of a wide-field scheme since achieving the frame rate required to match the AP timescale in a confocal arrangement is barely possible [194, 111]. Without going into the details of specific microscopy techniques, it is possible to derive some general relations for two distinct cases: transmission illumination and reflection illumination. For both cases, three simple assumptions are made:

1. The neuron is surrounded by a physiological medium with a refractive index difference between the neuron and the medium Δn on the order of 1% [32], and the membrane moves by $\Delta z \approx 1$ nm.

2. Ideal detection of the phase is achievable, i.e., one can perfectly convert change of phase into relative change in illumination intensity: $\Delta I/I = \Delta\phi$.

3. The intensity measurement is limited by the photon shot noise.

Transmission phase-sensitive microscopy is the only optical technique known from the literature [199, 108] for which the label-free detection of AP signals has

been reported. One can calculate the SNR of phase-sensitive microscopy under the assumptions listed above: given that the illumination wavelength λ is on the order of 10^3 nm, the observed relative intensity change due to membrane movement is

$$\Delta\phi = \frac{\Delta I}{I} = \frac{\Delta n \Delta z}{\lambda} \approx \frac{10^{-2} \times 1}{10^3} = 10^{-5}$$

where $\Delta n \Delta z$ is the difference in optical thickness, i.e., the phase accumulated by the wavefront when passing through the cell (Fig. 1, A). Using the shot noise limit assumption, implying that the noise level is $\sqrt{I}$, the SNR can be calculated as

$$\mathrm{SNR} = \frac{\Delta I}{\sqrt{I}} = \sqrt{I}\Delta\phi.$$

In other words, the SNR grows with the square root of illumination power, as predicted by the shot noise properties. The cell can typically handle several mW of illumination power [141], or on the order of 10^{13} photons for a 1 kHz frame rate. One can estimate that on the order of 100×100 pixels can be resolved within an area of a cell of a size of several tens of µm, leading to around $10^{13}/(100 \times 100) = 10^9$ reaching every pixel. In this case, the single pixel SNR will be on the order of $\sqrt{10^9} \times 10^{-5} \approx 0.3$. If the signal can be optimally averaged from all these pixels, the SNR can be enhanced by a factor of 100, giving a final SNR ≈ 30, making AP detection a fairly easy problem. However, this would require a camera capable of collecting 10^{13} photons in 100×100 pixels, i.e., having a full well capacity on the order of 10^9 e^- which is three orders of magnitude higher than the best of existing specialized cameras [81]. For this reason, the authors of [108] needed to use an extreme frame rate of 50 kHz, only achievable with highly complicated and expensive cameras, and significantly complicating data collection, storage, and processing.

Reflection phase-sensitive microscopy holds great promise for label-free optical AP detection, which can be demonstrated with a simple calculation using the assumptions listed above. Given that the cell is illuminated in a reflection scheme (Fig. 1, B), the phase change of the reflected light will be much larger since it is not scaled by the refractive index difference between the cell and the medium, i.e.,

$$\Delta\phi = \frac{\Delta I_r}{I_r} = \frac{\Delta z}{\lambda} \approx 10^{-3}$$

where I_r is reflected light intensity (note that the additional factor of 2 due to the double pass of light through the cell is ignored). The observed intensity, however, will be significantly smaller than illumination intensity I_0

$$I_\mathrm{r} = RI_0,$$

where R is cell reflectivity, that can be derived from the Fresnel equation

$$R = \left(\frac{n_1 - n_2}{n_1 + n_2}\right)^2,$$

which leads to $R \approx 10^{-5}$ for $n_1 = 1.33$ (water) and n_2 approximately 1% higher. A single pixel SNR is then given by

$$\text{SNR} = \frac{\Delta I_r}{\sqrt{I_r}} = \sqrt{I_r}\Delta\phi = \sqrt{RI_0}\Delta\phi.$$

For the same illumination intensity of 10^9 photons per ms per pixel, one would get $\text{SNR} = \sqrt{10^{-5} \times 10^9} \times 10^{-3} \approx 0.1$, or around 10 for a 100×100 pixels field of view assuming ideal detection. While this is lower than SNR of the transmission scheme, the requirement for full-well capacity is reduced by a factor of 10^5 to be only 10^4 e^-, which is easily achievable by the majority of even entry-level cameras. The authors of [108] hypothesize that the camera full-well capacity is the limiting factor for intensity, and not the stability of the cells. This is confirmed by optical tweezers experiments [141] , which demonstrate that cultured neurons can withstand illumination powers as high as as 100 mW at $\lambda = 980$ nm without noticeable damage for at least 1 minute. Thus, it is possible to safely increase illumination intensity by at least an order of magnitude, matching the expected SNR with transmission illumination geometry, while keeping the full-well capacity requirements (10^5 e^-) still realistically achievable by many general-purpose high-speed cameras [81, 113] and by majority of specialized ones [175].

The potential of using reflection geometry has been recognized in [108], however, the authors did not continue to prove it experimentally. An important complication of the reflection scheme is the difficulty in interpreting the reflected light phase pattern [83], which arises from the interference of light reflected at every depth plane of the cell. It is probable that understanding the reflected light field as inherently chaotic has discouraged other researchers from adopting it as an experimental technique, as demonstrated by the following quotation from [83]:

> The relationship between the phase, thickness, and refractive index of the object is completely obscured, and the phase map is a speckle distribution.

It is important to note that the reflected light field pattern encodes a “fingerprint” of the specific refractive index distribution inside the cell and is therefore much more information-rich compared to the transmitted light phase delay, which only provides information about the optical thickness of the cell. It is not immediately clear whether this richness of information is advantageous or disadvantageous for the AP detection problem. Experimentally determining this was one of the main goals of this PhD project.

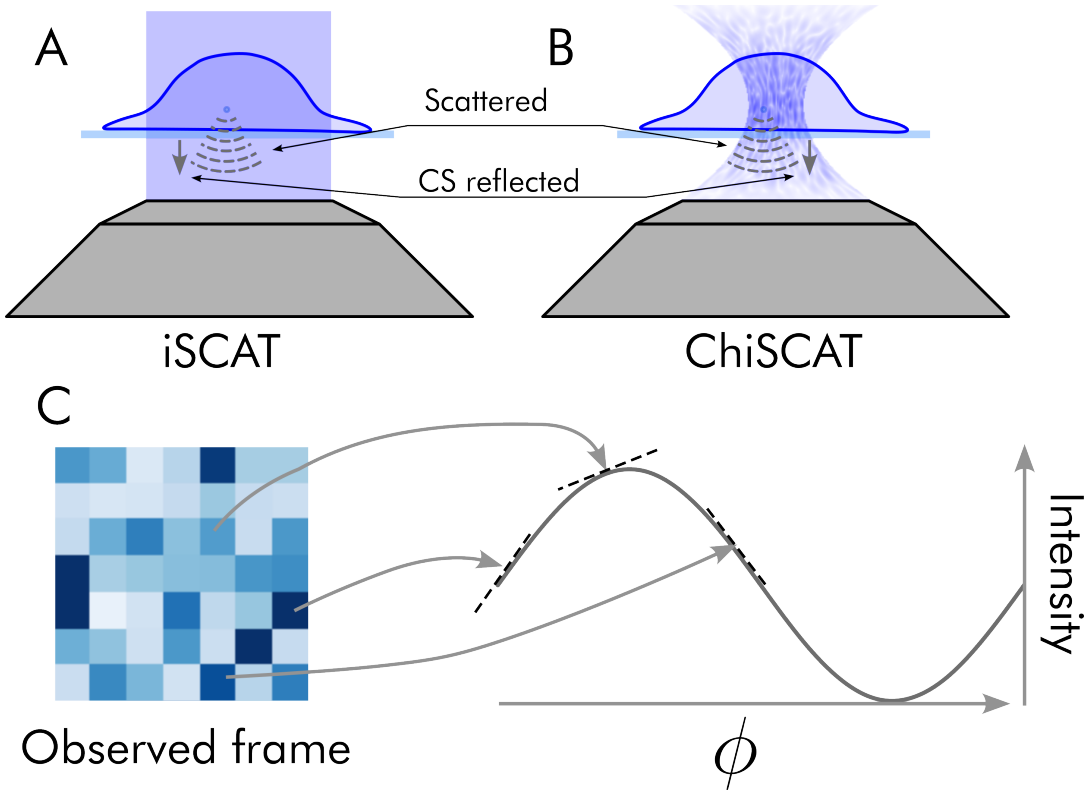


Figure 2: Comparison of iSCAT microscopy (A) to ChiSCAT microscopy (B), proposed in this project. In iSCAT scheme the collimated light beam (NA = 0) illuminates the sample, the observed signal is formed by interference of light scattered by the particle inside the sample and light reflected from the coverslide (CS). ChiSCAT replaces collimated beam with high-NA random light field, achieving higher resolution. Structure of the recorded signal (C): the random phase background makes it impossible to predict the sign of the given pixel intensity change caused by membrane motion .

2.4 Optical setup and algorithms for reflected-light phase-sensitive microscopy

Difficulties in interpreting phase patterns reflected from transparent 3D objects such as cells have mostly limited the application of phase-sensitive microscopy techniques to transmission illumination. These techniques have achieved great success in biology, where they have become the de-facto standard. Examples include Zernike phase-contrast microscopy [204], Nomarski differential interference contrast microscopy [132], and quantitative phase microscopy [144]. Reflected light phase-sensitive methods have mainly been applied to reflective surfaces, for instance, in the semiconductor industry, such as Mirau interferometry [38], phase-shifting interferometry [18, 97], and the reflective version of QPI [49]. Applications of reflective

phase-sensitive schemes in biology have been reported but did not gain popularity [14, 114, 92], with three important exceptions. Interference reflection microscopy [39] can visualize the cell membrane adherent to coverslides by relying on internal total reflection. Optical coherence tomography [85] has found numerous applications, not only in research but also in practical medicine. Interferometric scattering microscopy (iSCAT, [96]) is widely used for tracking individual particles in cells [201], including viruses, proteins, nanoparticles, etc. The latter has several desirable properties, making it suitable for label-free AP detection: it incorporates common-path interferometry, which makes it phase-sensitive by utilizing reflections from the coverslide, while suppressing vibration influence. It allows for fast wide-field imaging and is conceptually simple and easy to build, however, a significant disadvantage of iSCAT is its use of low numerical aperture (NA) illumination, which reduces its spatial resolution and depth selectivity. These issue is resolved in the modification of iSCAT proposed in the article published as a part of this PhD project [181], which will be discussed later.

Regardless of the exact optical scheme chosen, the collected data for whole-cell measurement (for both iSCAT and ChiSCAT) is a speckle pattern, which is not visually interpretable. Nevertheless, it encodes the specific distribution of the refractive index inside the cell. Thus, under the assumption of small amplitude movement $\Delta(x, y, z) \ll \lambda$, one can expect a linear change in each pixel intensity when the cell membrane moves due to AP firing. However, it is impossible to predict the sign of the change since neither the direction of the membrane motion nor the phase background created by scatterers inside the cell is known. Due to the differing signs of intensity change in different pixels (Fig. 2, C), naive signal averaging will not increase SNR. Thus, the only possible way to recover the AP signal is to use a data-driven signal detection method capable of learning unknown pixel signs from the available data. Developing a suitable algorithm capable of extracting these weak signals from the recorded videos is another important part of this PhD project.

2.5 Paper: "*ChiSCAT: Unsupervised Learning of Recurrent Cellular Micromotion*"

Full text of this publication [181] is attached to this PhD thesis. The core contribution of the paper is the development of the ChiSCAT optical scheme, its application to the measurement of electrically active cells (cardiomyocytes with muscle contraction disabled by the paralyzing drug blebbistatin), and the development of an algorithm capable of detecting the AP signals from the measurements.

Optical setup suggested in this article employs random light illumination (Fig. 2, Fig. 1 in [181]) to achieve high sensitivity to motion in any volumetric point of the

cell in any direction. The random light field, created by imaging a holographic diffuser surface into the back focal plane of the objective, achieves wide-field high-NA illumination of the cell volume. Moreover, the random field illumination effectively doubles the achievable resolution [70]. However, these advantages are obtained at the price of losing direct imaging ability, thus requiring a complicated data processing algorithm to extract the information. On the other hand, while the absence of imaging makes data interpretation more challenging, it allows for imaging through scattering tissues, potentially in the living brain. Intriguingly, the conversion of the recorded video into frequency space allowed for recovering certain imaging capabilities, including the detection of subcellular structures, potentially the nucleus or reticulum (Fig. 2 in [181]).

Data processing is another important contribution of this article. Several approaches have been tested, including:

- Semi-supervised matched filtering, achieved by calculating spike-averaged movies on half of the recorded video and using it to recover the AP signal from the other half of the video (Fig. 3 in [181]). This approach was found to work only in some cases, perhaps when residual muscle contraction from incomplete paralysis is present.

- Power detection, i.e., calculation of average RMS power along all pixels under the assumption that AP firing should transiently increase every pixel activity due to membrane motion. Like the previous method, it only produced meaningful data in a minority of cases, which can again be explained by imperfect disabling of cardiomyocyte beating.

- The ChiSCAT algorithm, based on the combination of frequency filtering and eigendecomposition of the modified Gramian matrix. This algorithm has demonstrated clear superiority to others, achieving AP recovery in 71% of experiments. A simple theoretical model developed and presented in this article clearly demonstrated the superiority of the ChiSCAT algorithm over naive power detection.

Dataset

The data collected during this project includes several hundred high-speed recordings of different cells measured with various versions of the experimental setup. This is another important contribution of this project, encouraging others to validate the data processing algorithms and potentially extract additional insights. A selected subset of this data is publicly available at the Zenodo repository (https://zenodo.org/records/10978122),

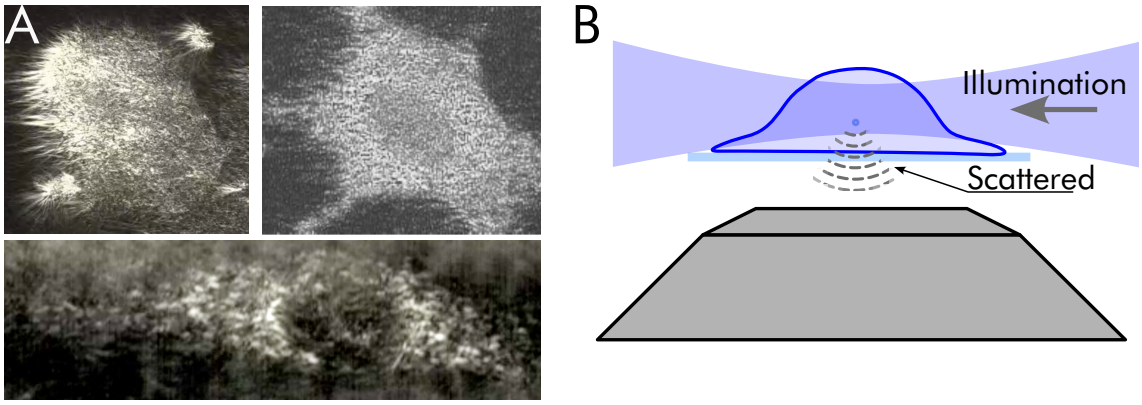


Figure 3: Examples of images obtained with laser side illumination (A); schematic representation of the optical setup used to obtain these images (B)

while the rest can be requested from the authors. Only part of the data is made available due to the excessive size of the full dataset (several TB).

Unpublished Results These include several optical schemes and data processing approaches that were either unsuccessful or their detailed investigation was beyond the resources available. The first experiments used white-light bright-field transmission microscopy as the optical scheme due to its simplicity and ease of interpretation of the obtained images. The detection of AP from data collected with this microscopy setup was unsuccessful, which is not surprising since cells are phase objects and absorb light very weakly. Another tested optical scheme was side illumination (a laser beam illuminating the sample from the side of the Petri dish at almost a 90° angle), allowing for capturing high-contrast images of the cells, potentially being sensitive enough for practical AP measurement. This scheme is somewhat similar to scattering setups [168], although it illuminates full cellular bodies, not just axons. Another practical advantage of this optical scheme is its immunity to reflections from planar surfaces in the setup, in contrast to reflection illumination, where reflections create an additional background due to antireflective coating imperfections. Examples of the images and setup are shown in Fig. 3.

Different architectures of neural networks (NNs) for data processing have been tested without success. These include 1D temporal convolutional NNs and 3D spatiotemporal NNs with different mechanisms of integrating information over frame size dimensions, such as simple averaging, weighted average, or attention. Their failure can be explained by either the insufficient amount of data collected for NN training or simply by the fact that a random phase background rendered spatial pattern recognition methods ineffective. However, this does not mean that applying machine learning methods will always be unsuccessful, and this approach should be reconsidered in future work.

2.6 Paper: *"When can we see micromotion? Experimental and theoretical analysis of the ChiSCAT scheme"*

The full text of this publication is attached to this PhD thesis [180]. This article builds upon the previous one by performing a detailed analysis of the ChiSCAT setup, answering theoretical questions about the ChiSCAT algorithm, and discussing the potential for better alternatives. From an experimental perspective, this article compares three different types of lasers as illumination sources and characterizes various noise sources, including the inherent cell noise of cultured human neurons. These experiments clearly demonstrate that cell noise is the dominant source of noise, approximately an order of magnitude higher than the shot noise limit obtainable with the equipment used in this experiment. The second part of the article focuses on the theoretical analysis of ChiSCAT algorithm performance under two different noise models: shot-noise-like random noise and correlated noise arising from the random motion of particles inside the cell. The application of spiked random matrix theory to the shot-noise limited model allowed for the derivation of a straightforward limit of detection, which predicts that label-free AP detection is indeed achievable with the ChiSCAT algorithm. However, this limit of detection is not achievable when cell noise dominates due to different noise properties. Nevertheless, this analysis allowed for the construction of a solid framework for understanding the limits of detection in different scenarios and suggested several other algorithms that hold great promise for recovering the AP signal from ChiSCAT measurements, which will be experimentally tested in future work. This part of the project also contributes to the field by publicly providing important high-speed recordings of human neurons, available in the Zenodo repository (https://zenodo.org/uploads/14275371), encouraging other researchers to develop and validate alternative data extraction algorithms.

Mechanism	**Description**	**Explained Observations**	**References**
Membrane electrostriction and piezoelectricity	Voltage-induced change of membrane geometry due to electrostrictive and piezoelectric behavior	Membrane motion	[67]
Membrane ferroelectricity	Voltage-induced change of membrane geometry due to ferroelectric behavior	Membrane motion, birefringence change, thermal effects	[105]
Voltage induced membrane tension change	Voltage-induced change of membrane geometry due to electrocapillarity	Membrane motion	[206, 128]
Near melting soliton propagation	Views AP as soliton propagation, supported by membrane phase transition	Membrane motion, thermal effects	[75]
Actin-myosin contraction	Views AP as co-propagation of electrical and mechanical waves and due to actin-myosin filament contraction	Membrane motion	[157]
Flexoelectricity	Voltage-induced change of membrane geometry due to flexoelectric behavior	Membrane motion	[129, 29]
Voltage induced membrane tension change + wave propagation	Views AP as co-propagation of electrical and mechanical waves due to electrocapillarity	Membrane motion, thermal effects	[50]

Table 2: Comparative table of mechanisms explaining electromechanical membrane movement during action potential propagation.

3 Localizing NV centers from intensity oscillations

3.1 A short outlook of the field

Scaling down magnetic resonance imaging (MRI) to the nanoscale paves the way towards extremely valuable measurement devices, capable of revolutionizing material science, biology, and medicine. While macroscale MRI became standard medical practice several decades ago [15], scaling it down to the nanoscale is still a challenge [19]. The first realistic setup, based on magnetic coupling between spin and the vibrating cantilever (magnetic resonance force microscopy, MRFM), allowing MRI to scale down to the nanoscale, was proposed by Sidles in 1991 [165] and implemented the following year at IBM [154], achieving 19 µm 1D resolution for electron spin resonance (ESR,) scans at liquid helium temperature. Actual nuclear MRI was demonstrated by the same group in 1994 [155], achieving 2.6 µm resolution in 1D at room temperature. Two years later, 3D scanning with 3 µm axial resolution was achieved [209].

A resolution of 170 nm in a semiconducting GaAs sample at cryogenic temperature (1D) was reported in 2003 [178], as well as the application of this technique to 3D imaging of spin-labeled liposomes, modeling a biological cell [184], achieving a spatial resolution around 1 µm. These improvements were mostly achieved by advancing the sensitivity of the setup, e.g., making the cantilever thinner and softer. An impressive 3D resolution of 80 nm was achieved by improvements in the reconstruction algorithm, another demonstration of the power of signal processing, albeit for ESR measurement [28]. Improvements in both technical parameters of the setup (magnetic field gradient, cantilever sensitivity) and reconstruction algorithms allowed achieving resolutions below 10 nm and performing single virus imaging [42]. Over the following years, the sensitivity of cantilevers was pushed to the limit by using carbon nanotubes [160, 126], suspended graphene sheets [20], or nanowires [130, 151]. Recent articles report 1D resolutions down to 2 nm [150] or even sub-nanometer [65] thanks to technical improvements in reducing noise and improving stability. The 2022 article by Haas et al. [71] reported sub-angstrom resolution for nuclear magnetic resonance diffraction, however, this technique cannot be categorized as imaging in the conventional sense.

Another branch of research is devoted to developing microcoils, which are probably the most straightforward way to miniaturize conventional MRI setups. While they find some application in biology and medicine [193, 125], their resolution is limited to several µm [188], with a fundamental limit at around 3 µm [30]. Performing the measurement at cryogenic temperatures allowed further decrease of resolution to 1.7 µm [30], but it is still orders of magnitude higher than the resolution achievable by other methods.

Using NV centers to perform nanoscale MRI was proposed in 2008 [10], relying on the magnetic dipole-dipole interaction between spins in the sample and optically readable NV spin, instead of magnetic coupling between spin and vibrating cantilever. Compared to MRFM, this approach has significant advantage: the NV centers' sensitivity to magnetic fields is extremely high, even at room temperature, thus the measurement does not require complicated cryogenics. Using this method, detection of an NMR signal from volumes as low as 5 nm^3 was achieved by two research groups [167, 118], although it has not been applied to imaging tasks. Imaging with 3D resolution of around 1 nm has been achieved for electron spins in 2014 [63]. In the following year, three important achievements were reported: proton MRI with 2D resolution of 10 nm [153], chemically resolved MRI of ^{1}H and ^{19}F nuclei with 10 nm 1D imaging resolution [72], as well as subnanometer 1D measurement of the adsorbate layer thickness on the diamond and 2D spatial imaging of ^{1}H, ^{19}F, and ^{31}P nuclei with 500 nm resolution [43]. Another article published the same year [7] suggested a method for accelerated localization of NV centers, called Fourier magnetic imaging, that achieved 30 nm resolution in 2D. The same technique was used to perform 3D imaging of individual NV centers in diamond with submicrometer resolution [8]. Precisely locating NV centers has applications, e.g., in quantum computing, quantum memory, or to perform imaging of single spin-labelled proteins as proposed in [170]. It is important to note that resolution of this method fundamentally only depends on the magnitude of the magnetic field gradient, which can be scaled almost arbitrarily.

3.2 3D magnetic resonance tomography: the signals observed

The core idea of NV localization relies on the fact that its fluorescence intensity depends on the spin state and that the spin will precess in a magnetic field (Larmor precession). Converting this precession into a readable change in fluorescence brightness requires a cleverly engineered readout technique, however, discussing it is beyond the scope of this thesis. Practically, this means the observed brightness of NV centers in a magnetic field will oscillate at a frequency defined by the strength of the magnetic field at the NV location. The frequency is given by

$$\omega(\vec{r}) = \omega(\vec{B}(\vec{r})) \approx \gamma B_z(\vec{r}) + \omega_0$$

where γ is the electron gyromagnetic ratio, $B_z(\vec{r})$ is the projection of the magnetic field at NV location $\vec{r}$ on the NV axis, and ω_0 is the oscillation frequency in the absence of an external magnetic field (zero-field splitting). An important implication of this is that as soon as the magnetic field distribution is known, the positions of individual NV centers along the field gradient axis can be determined from the corresponding oscillation frequencies (Fig. 4). This approach can be relatively easily

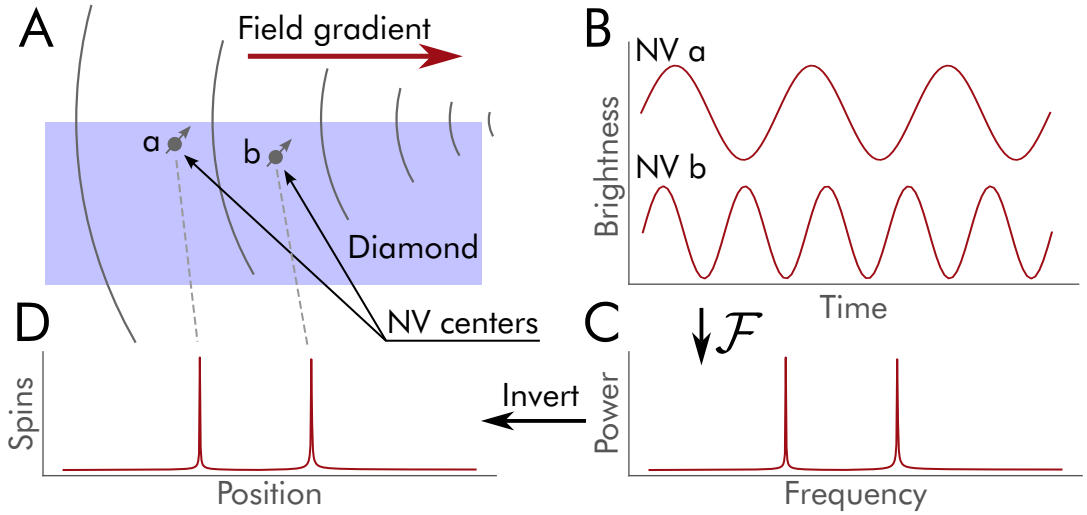


Figure 4: When magnetic field gradient is applied to a diamond sample containing NV centers (A), the frequency of their brightness oscillation (B) will be affected by the field in the given position. Thus, by measuring the brightness oscillations, performing Fourier transform (C) and converting the observed frequencies to positions (from the known magnetic field distribution) it is possible to localize NV centers with accuracy only limited by magnetic field gradient (D).

generalized to a 3D case by repeating the measurement three times in orthogonally oriented magnetic fields, since each measurement will localize the NV position in one dimension. Moreover, this method allows for simultaneous localization of multiple NV centers because the oscillation frequency of each can be effectively recovered from the mixed signal using a Fourier transform. Importantly, the minimal resolved distance between two nearby NV centers is defined only by the accuracy of determining the oscillation frequency (given by the fundamental properties of the NV center) and the magnetic field gradient, thus allowing for the resolution of features significantly below the diffraction limit, down to angstrom resolution if the field gradient is sufficiently strong.

Despite being conceptually simple, this experiment is rather difficult to perform in practice. NV centers have extremely low brightness (single photon, thus requiring a single-photon detector, such as an avalanche photodiode), which necessitates repeating the experiment approximately 10^5 times to achieve sufficient SNR. This leads to significant time requirements for the localization measurements (on the order of 10^0 to 10^1 hours). Because of this measurement timescale, the observed NV oscillation frequency can change slightly during the measurement due to the slow drift of the setup, leading to an increase in localization error. Besides that, due to fundamental noise sources and setup imperfections, both amplitude noise and phase noise are present, further complicating the measurement (Fig. 5 A-B).

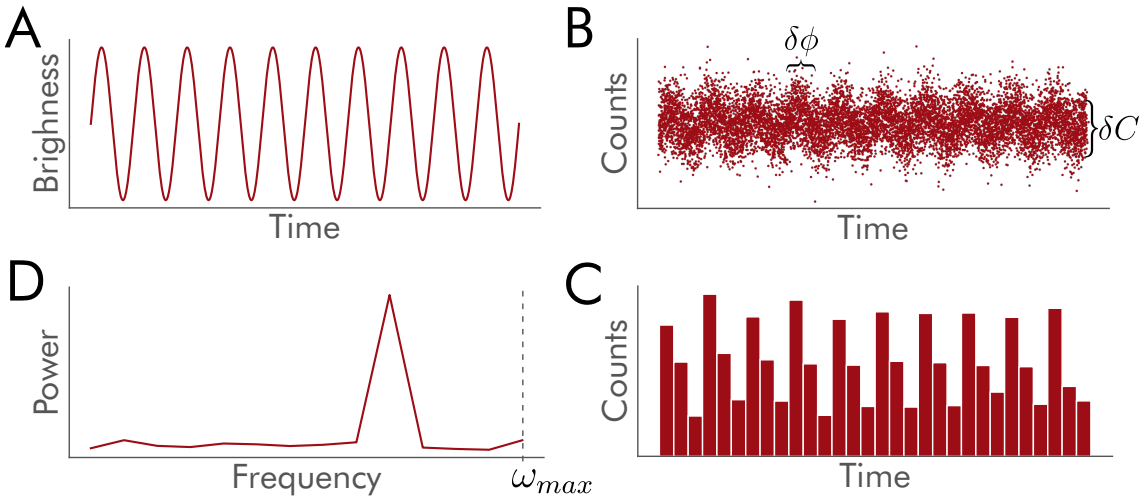


Figure 5: Models of ideal (A) and measured (B) NV fluorescence signals. Fundamental and instrumental noises add uncertainty in amplitude (δC) and phase ($\delta\phi$). Due to extremely low intensity of single atom emitter, the measurement needs to be repeated multiple times and binned (C), such that each bin contains on the order of 10^5 individual measurements. The obtained histogram is then Fourier-transformed to get an estimate of NV oscillation frequency (D), and, consequently, position.

To perform averaging in the presence of phase noise, the signal is binned, and the data is averaged within each bin, producing equally time-spaced samples used to obtain frequencies with a Fourier transform (Fig. 5 C-D). Since the number of averaged measurements inside each bin is proportional to the bin width, to improve SNR (or, equivalently, decrease measurement time), it makes sense to make the bins as wide as possible, up to a limit defined by the Nyquist-Shannon theorem. This means that the signal peak in frequency space will be located near the maximal observable frequency (Nyquist frequency $\omega_{\max}$).
In general, the time required to perform tomography measurements is a significant drawback, limiting the practical applicability of the method and decreasing the resolution due to the aforementioned slow setup drift. Thus, the main goal of the author of this PhD thesis was to investigate data processing approaches that can reduce the time requirements.

3.3 Algorithms to improve SNR / reduce time

Compressed sensing

This approach is based on the theorem [23], which states that a priori sparsity information can be used to recover a signal with a significantly smaller number of available samples than required by the Nyquist-Shannon theorem. Compressed sens-

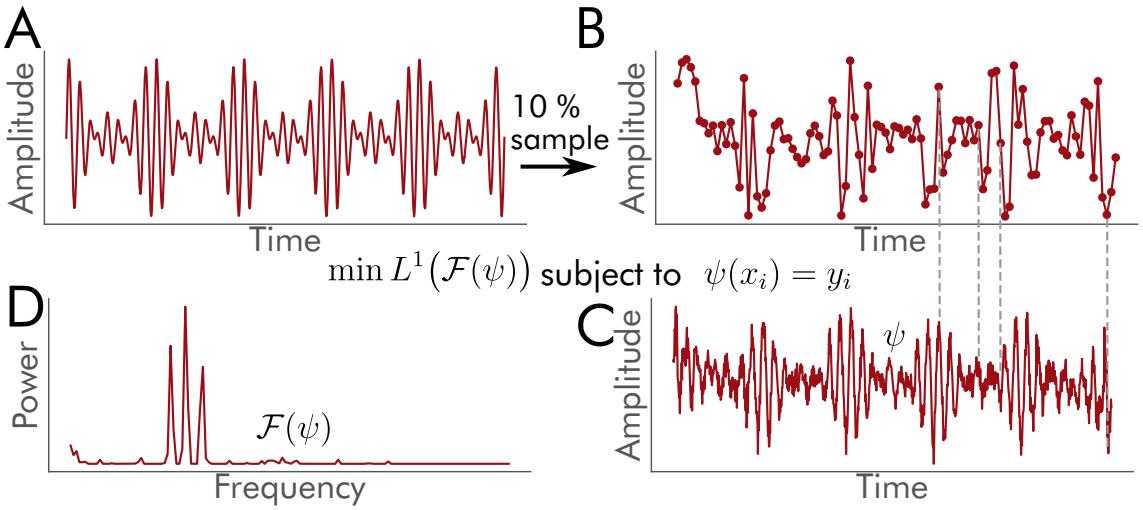


Figure 6: The illustration of compressed sensing approach. A true signal (A) is sampled at random time. When number of samples N_s is significantly smaller than Nyquist-Shannon theorem requirement, an obtained measurements (t_i, y_i), $i \in [0...N_s]$ form uninterpretable waveform (B). However, by finding the function ψ (C) satisfying $\psi(t_i) = y_i$ which minimizes L^1 norm of the signal spectrum (D), the true waveform can be recovered.

ing is widely used to reduce data acquisition time for medical MRI [112], making it a potential candidate for accelerating nanoMRI, already demonstrated before [7]. The core idea of compressed sensing is sparsity-inducing minimization of the L^1 norm of a signal, ψ, recovered from an incomplete set of measurements (t_i, y_i), $i \in [0...N_s]$, constrained such that the recovered signal ψ satisfies the available samples, i.e., $\psi(t_i) = y_i$ (Fig. 6). Literature [112, 7] suggests that this approach can reduce the time required to collect the data by a factor of 5-10. Despite impressive results, the practical applications of compressed sensing require some care. Firstly, the available samples must be randomly distributed in time (a requirement of the original theorem [23]), which is challenging to achieve with measurement devices optimized for periodic sampling. Multiple sampling strategies have been developed [17, 189, 93], but reconstruction results remain unstable under different choices of sampling strategy [93]. Secondly, practical experiments with compressed sensing for NV fluorescence showed that reconstruction is additionally destabilized when the measurements have low SNR. Finally, the reconstruction algorithm is computationally expensive (fast algorithms exist [40], but require tuning hyperparameters). Thus, as part of this PhD project, a simple aliasing-based scheme for reducing the volume of collected data was proposed, relying on a simple model of NV fluorescence signal and not requiring any additional processing.

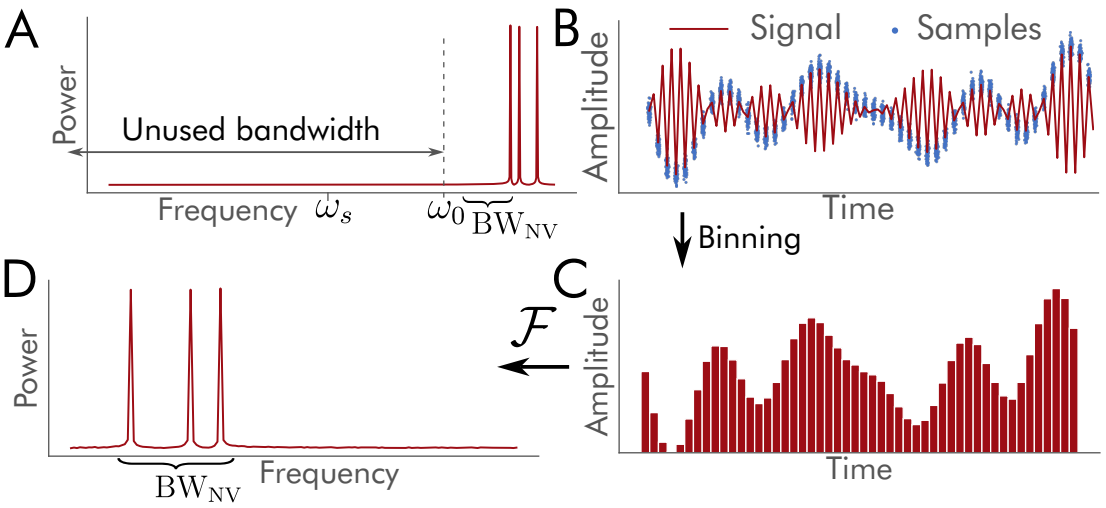


Figure 7: The illustration of aliased sensing approach. When the NV signal is sampled with frequency above the Nyquist rate, the majority of the signal bandwidth remains unused (A) due to zero-field splitting frequency ω_0. Instead, one can sample the NV intensity oscillations with smaller frequency ω_s, leading to creation of aliased waveform (B). When these samples are binned (C) and Fourier transformed (D), the positions of the NVs can be recovered. One can imagine it as "folding" of the original frequency space (A) around sampling frequency ω_s to get (D), thus the order of NV peaks is inverted.

Aliased sensing

As explained above (subsection 3.2), while binning the observed photon counts, wide bins are preferred to maximize SNR. In the limiting case, bins can be as wide as half of the oscillation period, satisfying the Nyquist criterion of 2 samples per oscillation. Due to zero-field splitting, NV intensity oscillations have a frequency of at least ω_0, while the bandwidth of the NV signal, $\mathrm{BW_{NV}}$ (the difference between the lowest and highest frequency of NV), is much smaller due to their proximity. Thus, only a small part of the frequency spectrum actually encodes NV positions. In other words, sampling at the Nyquist rate (twice the highest NV oscillation frequency) is excessive, leading to a majority of the bandwidth being unused (Fig. 7, A).

Is it possible to sample only a subset of the frequency space corresponding to NV locations? This problem is very similar to that of FM radio reception, solved for almost a century [53], where the task is to detect an audio signal (bandwidth ≈100 kHz) modulating the carrier wave (in the $10^0..10^2$ MHz range) frequency. An important step before detection, called downconversion, i.e. reducing the carrier frequency is usually solved by mixing the signal with a reference frequency (heterodyne). At the same time, sampling the signal at discrete intervals creates aliasing, effectively con-

verting the signal frequency to a lower one, similar to superheterodyne conversion where the sampling frequency plays the role of the heterodyne [195].
This principle is shown in Fig. 7: when the NV brightness signal is sampled with a frequency lower than the Nyquist frequency, it creates an aliased waveform, which still encodes information about NV positions that can be recovered as soon as the undersampling factor is known. These samples can be binned in the same manner as full sampling and Fourier transformed to obtain NV frequencies. This method can effectively decrease the number of bins required to measure the NV oscillation frequency by a factor of $\approx \omega_0/\mathrm{BW}_{\mathrm{NV}}$. Recovery of true NV frequencies does not require any complicated algorithms and can be calculated with a simple formula. Details can be found in the article [170].

3.4 Paper: *"Three-dimensional magnetic resonance tomography with sub-10 nanometer resolution"*

Full text of this publication [170] is attached to this PhD thesis. This articles demonstrates 3D localization of NV centers in diamond with position uncertainties $\delta\vec{r} = (5.9, 9.9, 14.7)$ along real-space axis. The achieved resolution is two orders of magnitude higher than the previously reported results [8], mainly achieved due to technical improvements in generating magnetic field gradient. Aliased sensing scheme applied to here allowed to reduce amount of data required to localize NVs by an order of magnitude. This brings additional improvements in localization accuracy due to smaller setup drift over the measurement time.

4 Conclusion

Despite significant advances in both fundamental development of data-driven methods (including AI boom happening at the moment of writing this thesis [62]) and their applications, natural sciences still can significantly benefit from tighter incorporation of data-driven approaches. The room for improvement of existing techniques is significant, ranging from fundamental physics and astrophysics to chemistry and biology. In this PhD project, the potential of data-driven approaches have been demonstrated on two very different examples. During the main phase of the project, the data processing algorithm for decoding uninterpretable speckle pattern was developed and applied to reflected-light phase-sensitive microscopy data, which have been previously considered impossible to interpret. This demonstrated possibility of label-free detection of action potentials in electrically active cells, relying only on minuscule intrinsic optical signals, arising from nanoscale membrane movement. Specifically, it was demonstrated that proposed algorithm is capable to recover of action potentials in 71% of experiments, significantly higher than baseline signal detection approaches applied to the same data. During the secondary phase, the optimized data collection strategy and data processing scheme for 3D nanoscale spin tomography of NV centers in diamond have been proposed and experimentally validated. The approach exploits a priori known structure of the experimental data to derive positions of NV centers from the minimal number of measurements, demonstrating decrease of data collection time requirements by an order of magnitude. Moreover, the resolution of proposed tomography scheme is have been improved by two orders of magnitude compared to the previously reported literature data, although author of this thesis played a secondary role in reaching this resolution (by decreasing time requirements, thus reducing scale of the setup drift during experiments).

Besides results in the area of data processing, a suitable microscopy setup have been built and optimized for performing reflected-light interferometric microscopy. Improvements in existing optical schemes have been made, leading to development of ChiSCAT, a chaotic speckle pattern microscopy sensitive to motion in every voxel of the observed cell in every direction and allowing high-speed imaging. Experiments have been performed with two types of cells: human iPSC-derived cardiomyocytes and human iPSC-derived neurons. The collected data have been made publicly available to facilitate development of other data processing techniques for the task of action potential detection. During the second step of this project, the detailed theoretical analysis of the suggested algorithm was performed, and lead to identification of promising future direction of research, providing a basis for future exploration by other scientists.

In conclusion, the author believes that potential impact of this project extends be-

yond the immediate results achieved, demonstrating that data-driven techniques are indispensable tools in the toolbox of natural scientists, capable of bringing new capabilities in multiple scientific fields. This PhD project highlights the synergy of integrating innovative data processing with ad hoc experimental design, demonstrating the important role of data-driven methodologies in accelerating scientific discovery during the age of data.

5 Published articles

5.1 ChiSCAT: Unsupervised Learning of Recurrent Cellular Micromotion

Authored by **Andrii Trelin**, Sophie Kussauer, Paul Weinbrenner, Anja Clasen, Robert David, Christian Rimmbach, and Friedemann Reinhard
Journal: Nano Letters 24, no. 40 (2024): 12374-12381.
Published: 24.09.2024
DOI: 10.1021/acs.nanolett.4c02425
Reference: [181]

NANO LETTERS

pubs.acs.org/NanoLett Letter

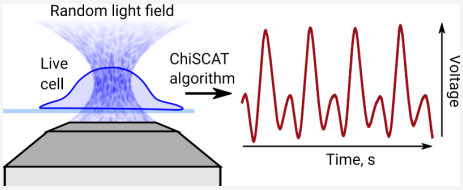
ChiSCAT: Unsupervised Learning of Recurrent Cellular Micromotion Patterns from a Chaotic Speckle Pattern

Andrii Trelin, Sophie Kussauer, Paul Weinbrenner, Anja Clasen, Robert David, Christian Rimmbach, and Friedemann Reinhard*

Cite This: *Nano Lett.* 2024, 24, 12374−12381 Read Online

ACCESS | Metrics & More | Article Recommendations | Supporting Information

ABSTRACT: There is considerable evidence that action potentials are accompanied by "intrinsic optical signals", such as a nanometer-scale motion of the cell membrane. Here we present ChiSCAT, a technically simple imaging scheme that detects such signals with interferometric sensitivity. ChiSCAT combines illumination by a **ch**aotic speckle pattern and interferometric scattering microscopy (**iSCAT**) to sensitively detect motion in any direction. The technique features reflective high-NA illumination, common-path suppression of vibrations, and a large field of view. This approach maximizes sensitivity to motion, but does not produce a visually interpretable image. We show that unsupervised learning based on matched filtering and motif discovery can recover underlying motion patterns and detect action potentials. We demonstrate these claims in an experiment on blebbistatin-paralyzed cardiomyocytes. ChiSCAT opens the door to action potential measurement in scattering tissue, including a living brain.



KEYWORDS: *action potential, label-free imaging, interferometric microscopy, iSCAT, time series analysis*

Downloaded via UNIV ROSTOCK on December 3, 2024 at 13:43:30 (UTC).
See https://pubs.acs.org/sharingguidelines for options on how to legitimately share published articles.

Literature data suggest that action potentials are accompanied by "intrinsic optical signals", tiny changes in the optical properties of a cell that can be detected by label-free optical imaging.[1−12] The most accepted mechanism is a nanometer-scale motion of the cell membrane,[7] occurring due to various factors, including the flexoelectric effect or voltage-induced changes in membrane tension.[13] Detecting action potentials by direct label-free observation of nanoscale cell motions in interferometric microscopy is highly promising, since it provides several unique advantages over dye-based voltage or calcium imaging: it does not suffer from photobleaching, which enables prolonged observation. Moreover, the illumination wavelength can be freely chosen and can be optimized to minimize cellular damage or to minimize optical scattering and hence allow chronical imaging through multiple tissue layers, e.g., the cortex of the brain. Intrinsic signals are small fluctuations on a large background. Past studies have established that the average scale of membrane movement is $\Delta z \approx 1$ nm.[7,11,12,14,15] In a suitable phase sensitive interferometric microscopy technique, this translates into an intensity change of

$$\frac{\Delta I_{\text{signal}}}{I} \approx \Delta\phi \approx \frac{\Delta n}{n}\frac{\Delta z}{\lambda} \approx 10^{-5}$$

assuming a relative refractive index change between cell and medium $\Delta n/n \approx 10^{-2}$ (according to ref 16) and a relative phase change of $\Delta z/\lambda \approx 1 \times 10^{-3}$. Intriguingly, such a signal could be easily detected in a single shot. The quantum shot noise limit of interferometry is

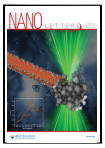
$$\frac{\Delta I_{\text{shot noise}}}{I} = \sqrt{\frac{1}{N}}$$

where $N = P\Delta t/(\hbar\omega)$ denotes the number of photons employed. Assuming $P = 1$ mW of illumination power and an integration time of $\Delta t = 1$ ms, matching the time scale of an action potential (AP), the quantum shot noise limit is on the order of $\Delta I_{\text{shot noise}}/I \approx 10^{-7}$, and the expected signal-to-noise ratio (SNR) is around 100.

However, existing experiments on label-free AP detection still fall short of this limit. Published results have been obtained on nonmammalian large axons and nerves,[4] or had to resort to invasive techniques like atomic force microscopy.[17] plasmon imaging[18] or spike-triggered averaging of multiple APs to reveal the signal with SNR ≥ 1.[10−12]

Presumably, a major reason is that increasing the SNR is more challenging than simply increasing the excitation power. In transmission microscopy, the full-well capacity of the imaging camera sets a limit for excitation power at a level of nanowatts. This can be overcome by a reflective illumination scheme, promising a great gain in sensitivity.[12] However, existing reflective schemes either restrict acquisition to a single

Received: May 23, 2024
Revised: September 17, 2024
Accepted: September 17, 2024
Published: September 24, 2024



ACS Publications

© 2024 The Authors. Published by American Chemical Society

https://doi.org/10.1021/acs.nanolett.4c02425
Nano Lett. 2024, 24, 12374−12381

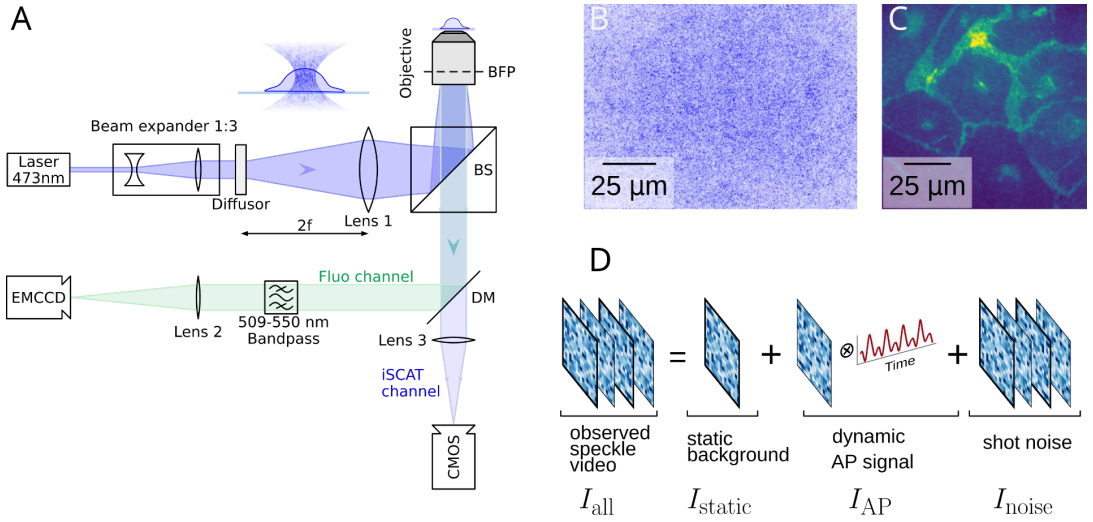


Figure 1. Experimental setup and exemplary data. (A) Optical setup, combining iSCAT microscopy with speckle illumination (ChiSCAT) and a fluorescence voltage imaging path for reference. Both cameras are synchronized. (B) Raw ChiSCAT image, (C) raw fluorescence image, and (D) model of the ChiSCAT signal. A static speckle pattern background ("static speckle") is superimposed with a periodically modulated speckle pattern ("AP speckle"), which repeats for every action potential and arises from cellular micromotion.

diffraction-limited plane,[19,20] reducing the signal, or merely produce an unspecific speckle pattern, which cannot be easily interpreted:[21] the reflected beam contains interfering signals from all depth levels inside the cell, which leads to a chaotic speckle-like appearance.

Here, we overcome this limitation. We present an unsupervised learning scheme to recover AP signals from a speckle pattern without *a priori* knowledge of the timing of the action potentials or the spatial pattern of motion triggered during an AP. Moreover, we intentionally maximize the chaotic nature of the image by illuminating the specimen with a speckle pattern. This creates a random 3D light field in the cell, making the technique sensitive not just to the motion in height but also to motion in the $X-Y$ plane, achieving interferometric sensitivity to motion in any illuminated voxel. In other words, the observed image is a "fingerprint" of the cell geometry and exact volume distribution of intracellular scatterers.

Since ChiSCAT is not based on a visually interpretable image, it paves the way to detecting action potentials even in scattering tissue, including the living brain: a signal passing through multiple layers of scatterers will change, but the nature of a cell shape "fingerprint" will be conserved. By this fingerprint, a detected action potential could be assigned to a specific cell or group of cells, even though no imaging information about its position could be obtained from a strongly scattered speckle pattern. The technique would thus provide information similar to spike sorting in electrophysiology. We will now demonstrate this by successfully detecting action potentials in blebbistatin-paralyzed cardiomyocytes.

Our setup (Figure 1 A) is based on wide-field interferometric scattering microscopy (iSCAT[22]). We illuminated the cell with coherent light. The resulting image is an interference of light scattered by the cell and light scattered at the cover slide−immersion medium (water) interface, providing a common-path suppression of vibrations in the setup. Light scattered in random parts of the cell interferes with the light reflected from the cover slide, forming a speckle signal. In iSCAT, this speckle background is usually removed during the data processing step, e.g., to highlight motion of a single nanoparticle.[23,24] Tracking the motion of a single membrane from the speckle background in iSCAT has also been reported in the literature[25] by using different processing of the speckle background, where it served as a tool to quantify background motion while tracking a single particle. Past work, however, has remained limited to tracking single membranes or particles in a wide-field regime or required switching to the confocal regime.

ChiSCAT takes the opposite approach. It does not aim to track a single particle or membrane but to generate a holistic and interferometrically sensitive "motion fingerprint" of all components in an entire cell and extract meaningful information by data analysis. To achieve this, we maximize the speckle background by employing speckle illumination (Figure 1A,B). This is achieved by a holographic diffusor in the excitation path and serves several purposes. First, speckle illumination uses the full numerical aperture of the microscope.[26] Both illumination and detection have a high numerical aperture, yielding a higher resolution than classical wide-field iSCAT or quantitative phase imaging, which employ a parallel, i.e., low-NA, excitation beam. ChiSCAT thus combines the spatial resolution of confocal iSCAT with the field of view of wide-field iSCAT. Second, erasing direct imaging information creates a demanding test case for the detection algorithm, which mimics the signals obtained in scattering tissue such as the brain.

The setup features a correlative path for fluorescence voltage imaging (Figure 1A,C), which is only needed as a ground-truth reference to benchmark the processing algorithms. We employ this setup to perform experiments on human-induced pluripotent stem cell derived cardiomyocytes, with mechanical contraction disabled by the myosin inhibitor blebbistatin. Since this inhibition might not be perfect, these cells can potentially exhibit larger micromotion in response to an AP than neurons. Most likely, the motion is larger than a few nanometers but still significantly below the optical diffraction limit (≈ 240 nm).

https://doi.org/10.1021/acs.nanolett.4c02425
Nano Lett. 2024, 24, 12374−12381

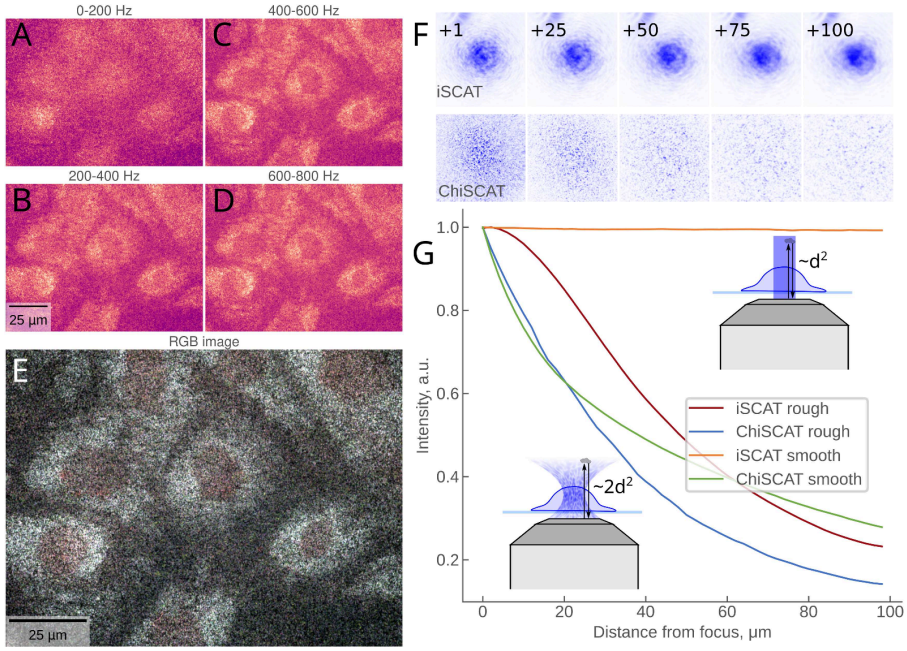


Figure 2. Frequency-resolved cellular dynamics imaging by ChiSCAT imaging. A–D: rms activity in a band-pass-filtered ChiSCAT recording. E: visualization as an RGB image (red channel = B, green channel = C, blue channel = D); a region with reduced high-frequency fluctuations is visible in the center of the cell, presumably the nucleus and/or reticulum. F: Measurement of depth-selectivity. The data presented are camera images of a cover slide moving out of focus for iSCAT and ChiSCAT illumination. The number in the corner denotes the distance from the focal plane in μm. G: observed signal intensity as a function of distance from focus, obtained by integrating across a region of interest in F. We compare a smooth sample (cover slide, traces "iSCAT smooth", "ChiSCAT smooth") and a rough sample (polymer microspheres, "iSCAT rough", "ChiSCAT rough"). In all cases, the ChiSCAT signal intensity drops significantly faster then iSCAT.

In the ChiSCAT channel, we expect a signal as sketched in Figure 1 D. It consists of three components: a static speckle background created mainly by light scattered from the cover slide, a speckle pattern that is modulated by the time-dependent and repeating AP signal, and noise that for sufficiently strong illumination is dominated by photon shot noise.

Mathematically, the superposition of two of these three components in the camera plane can be modeled as complex (phasor) electric fields:

$$E_{\mathrm{all}} = E_{\mathrm{static}} + E_{\mathrm{AP}} + E_{\mathrm{fluct}}$$

Here, E_{static} refers to light reflected from the cover slide and static parts of the cell, E_{AP} to light scattered from cellular components varying along the AP, e.g., a vibrating plasma membrane, and E_{fluct} to light scattered from other moving parts of the cell such as diffusing vesicles. All fields $E_{\mathrm{all|static|AP|fluct}}(x, y, t)$ are random speckle fields in the spatial coordinates x and y, and they can depend on time (t). The intensity recorded by the camera is then given by

$$I_{\mathrm{all}} = E_{\mathrm{all}}^{*} E_{\mathrm{all}} \approx I_{\mathrm{static}} + I_{\mathrm{AP}} + I_{\mathrm{noise}}$$

Here, the noise term I_{noise} includes non-AP fluctuations (the term $\mathrm{Re}[E_{\mathrm{all}}^{*} E_{\mathrm{fluct}}]$) as well as detection noise such as photon shot noise or readout noise of the camera. Crucially, the AP signal can be factorized as follows:

$$E_{\mathrm{AP}}(x, y, t) = E_{\mathrm{AP}}(x, y) \otimes a(t);$$

$$I_{\mathrm{AP}}(x, y, t) = \mathrm{Re}[E_{\mathrm{all}}(x, y)^{*} E_{\mathrm{AP}}(x, y)] \otimes a(t) \overset{|E_{\mathrm{static}}| \gg |E_{\mathrm{AP}}|, |E_{\mathrm{fluct}}|}{\approx}$$

$$\mathrm{Re}[E_{\mathrm{static}}(x, y)^{*} E_{\mathrm{AP}}(x, y)] \otimes a(t) =: I_{\mathrm{AP}}(x, y) \otimes a(t)$$

where $a(t)$ denotes action potential amplitude, likely following a similar time trace as the trans-membrane voltage. In a simplified picture, whenever $a(t)$ spikes, a characteristic pattern of $I_{\mathrm{AP}}(x, y)$ appears in the ChiSCAT recording.

The ChiSCAT recording is interferometrically sensitive to motion, and meaningful images can be reconstructed from the chaotic speckle pattern by data processing. As a simple example, temporal band-pass filtering of the video stream reveals an easily recognizable image of individual cells (Figure 2, A–E). Fluctuations at high (>300 Hz) frequencies are markedly reduced in or around the nucleus, possibly due to restricted diffusion in the nucleus and reticulum, confirming recent observations by refractive index tomography.[27] ChiSCAT is depth-selective. The signal observed in a region of interest arises mainly from a range of depths comparable to the size of the region, because ChiSCAT, in contrast to existing wide-field schemes,[21,28] employs high-NA illumination.

This can be understood by considering that, for low-NA schemes, illumination intensity is approximately constant, and depth selectivity is mainly achieved through the quadratic decay of the signal scattered from small particles with a roughly spherical scattering pattern. For flat surfaces, low-NA illumination offers minimal depth selectivity, sometimes

https://doi.org/10.1021/acs.nanolett.4c02425
Nano Lett. 2024, 24, 12374−12381

causing artifacts from reflections at the medium−air interface to be as far as 10 mm away. High-NA illumination, however, is inherently depth-selective because its intensity quickly decays outside the focus. We demonstrate this by measuring the suppression of light scattered from a movable out-of-focus plane (Figure 2, F and G).

We now turn to the main goal of this work: label-free detection of action potentials from a visually noninterpretable ChiSCAT recording. In mathematical terms, the goal is finding $a(t)$, the time-varying amplitude of AP activity with a maximum signal-to-noise ratio.

It is known that the optimal linear solution to this problem is matched filtering.[29] This scheme provides an estimate $a_{MF}(t)$ of $a(t)$ by convolving the signal (in our case a ChiSCAT movie I_{all}) with a time-reversed elementary template a_{el}:

$$a_{MF} = I_{all} \otimes_t a_{el} = \sum_{x,y,t} I_{all}(x, y, t) I_{el}(x, y, -t)$$

In our case, $I_{el} = I_{AP} \otimes a_{el}(t)$ can be thought of as a noise-free ChiSCAT movie of a perfect single action potential. Crucially, neither I_{AP} nor a_{el} is known in advance.

One way to obtain I_{AP} is supervised learning by spike-triggered averaging of the ChiSCAT signal, which we demonstrate in Figure 3. We first extracted a fluorescence trace by spatially averaging the fluorescence movie. Fluorescence peaks, corresponding to individual APs, are detected and used to extract slices from the ChiSCAT movie (only training subset), which are then averaged to produce an estimation of I_{AP}. The original speckle movie is then convolved with this extracted matched filter to produce the recovered signal $a_{MF}(t)$.

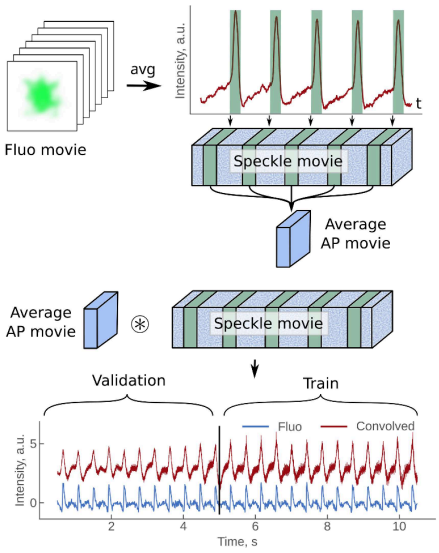


Figure 3. Supervised match filtering approach. The ground truth AP signal is extracted from the training subset of the fluorescence movie to calculate the average spike-triggered speckle movie. The latter is then used as convolution filter on the rest of the speckle signal, allowing to extract AP from the validation part of the movie.

As visible from Figure 3, this approach is indeed able to recover individual APs; however it suffers from two problems: first, it requires a known ground truth signal for training (fluorescence in our case), which undermines the concept of label-free microscopy. Second, this approach is only optimal under assumption of static background (static speckle I_{static} in Figure 1, D) and a perfectly repeating dynamic pattern I_{AP}, while in reality both slowly drift on a scale of 2−3 s due to slow motion of the cell. This makes the spike-triggered average incoherent and reduces the intensity of the signal. In an experiment on 64 regions of cells, supervised learning was successful in 36% of the regions.

The most central discovery of this work is an unsupervised learning scheme that can efficiently recover repeating patterns of motion without requiring ground truth information. It instead exploits the *a priori* information that APs are recurring events and that the approximate temporal amplitude pattern a_{el} of an AP is known.

The full algorithm is visualized in Figure 4, A. It is based on a combination of temporal matched filtering and motif discovery. The algorithm begins by convolving the raw ChiSCAT movie along the time axis with a 1D model of signal a_{el}. For simplicity, a zero-mean Gaussian function was chosen, the width σ of which was adapted to the typical time scale of an AP.

The resulting convolved movie was subsequently cropped to a region of interest (ROI), identified from pixels with high temporal variability. This is accomplished by computing the standard deviation along the time axis, followed by Gaussian smoothing and thresholding.

We then search for recurring patterns in the resulting movie by calculating the dot product between every possible pair of frames, forming a Gramian matrix. A recurring event, i.e., a set of two similar frames occurring some time apart, will produce an off-diagonal peak in this matrix because the frames are strongly correlated with each other, whereas each of them is uncorrelated with the noise. This approach to identifying recurring events is reminiscent of a recurrence plot,[30] only using a dot product rather than a difference as a metric for similarity. APs can be detected as off-diagonal peaks of the Gramian matrix, and a column or row crossing of one of the peaks is a time trace of AP activity.

Due to the slow fluctuations of the cell, the cross-correlation between two frames both containing an AP decreases with increasing temporal distance between them and vanishes for time scales larger than a few seconds, which can be seen as decay in the off-diagonal peak amplitude when plotting a single row of the Gramian (Figure 4, A, "cross-correlation decay"). To reconstruct a nondecaying AP trace over the ChiSCAT movie, we use a rank-one approximation; that is, we find a vector a_{rec}, such that its outer product with itself $a_{rec}a_{rec}^T$ approximates the Gramian matrix. One can imagine this as finding a checkerboard pattern in the matrix which best approximates the experimentally observed Gramian. Technically, this is achieved by finding the largest eigenvector of the Gramian. Before the eigendecomposition, the diagonal of the Gramian matrix is zeroed out to reduce the influence of random nonrecurrent events. Importantly, the low-rank approximation aggregates information from multiple action potentials and hence improves the signal-to-noise ratio over what could be obtained in a single correlation of one pair of frames.

Applying the algorithm to a set of cell regions (Figure 4 B), we find that it indeed recovers action potentials, even for regions where supervised learning has failed. Overall, detection

https://doi.org/10.1021/acs.nanolett.4c02425
Nano Lett. 2024, 24, 12374−12381

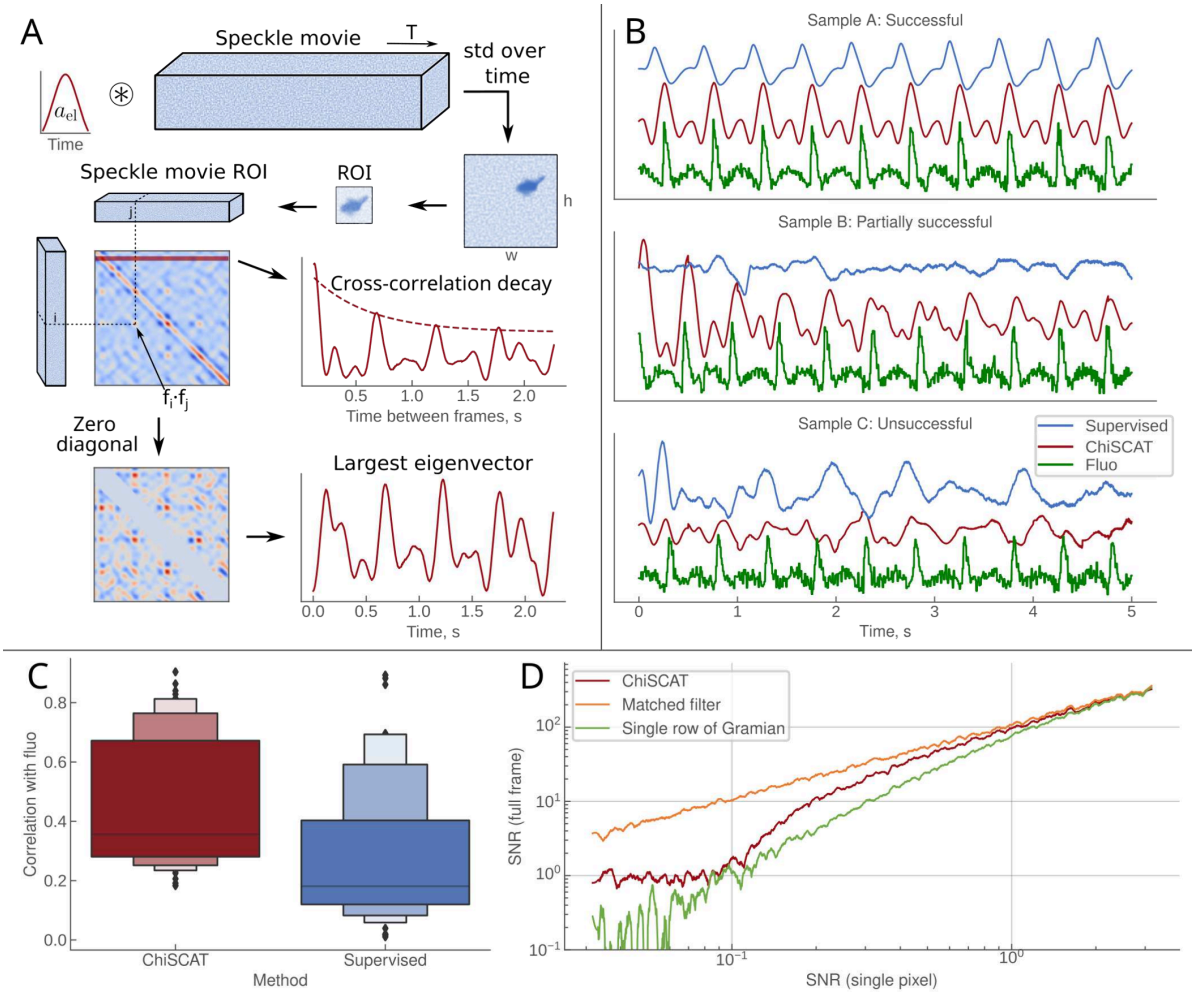


Figure 4. Unsupervised reconstruction of action potentials. (A) Signal processing pipeline. The ChiSCAT movie is matched-filtered by convolution with a temporal template of the action potential a_{el}. Recurring events are identified by computing the Gramian matrix $G_{ij} = f_i \cdot f_j$ for each pair of frames f_i, f_j. Recurring events appear as off-diagonal peaks in this matrix, and a column or row crossing one of the peaks ("cross-correlation trace") is a time trace of the AP activity. A full-length AP trace ("largest eigenvector") is obtained by eigendecomposition of G. (B) Reconstructed AP activity for different samples of cells. (C) Distribution of correlation coefficient between extracted signal and ground truth for different samples of cells. ChiSCAT restores the AP signal in the majority of cases. (D) Simulated SNR of the extracted signal for different algorithms as a function of SNR in a single pixel ($N_{px} = 100^2$, 9 APs in the simulated data). The full ChiSCAT algorithm demonstrates an intermediate performance between matched filtering with a perfect template and simple extraction of off-diagonal peaks in the Gramian.

succeeds in 71% of the regions (Figure 4, C), which is a marked improvement over supervised detection.

We can confirm this improvement by a simple numerical model (Figure 4, D, and SI). It models the frames $\vec{f}_i = I_{all}(x, y, t_i)$ of the speckle movie as random Gaussian noise with an additional fixed zero-mean random pattern $\vec{p}$ periodically superimposed onto some selected frames to model the AP signal fingerprint ($\vec{p} = I_{AP}(x, y)$). This effectively models action potentials as a train of delta functions in time. From this synthetic data set we compute three time traces: (1) The time series $r_i = \vec{f}_i \cdot \vec{p}$, effectively modeling spatial matched filtering with a perfect template $\vec{p}$; (2) the time series $r_i = \vec{f}_s \cdot \vec{f}_i$, where $\vec{f}_s$ is a signal frame containing both the signal pattern $\vec{p}$ and Gaussian noise, effectively modeling a single column or row of the Gramian matrix in Figure 4; (3) the time series obtained from the full ChiSCAT algorithm, i.e., all steps of Figure 4, A. For all series, we compare the height of a signal peak with the rms noise of a signal-free region. As expected, spatial matched filtering performs best and can be fully matched by the other schemes only if a signal-to-noise ratio larger than 1 is already obtained in a single-pixel time trace. Unsupervised detection correlates the movie with a signal frame instead of the perfect pattern $\vec{p}$. For weaker signals, this signal frame is dominated by noise, which leads to an inferior performance. A simple analytical estimate (SI) suggests that this overhead is a factor of $\sqrt[4]{N_{px}}$ in SNR, where N_{px} is the number of pixels in a frame. Due to the slow $\sqrt[4]{}$ scaling, this overhead is not excessive, reducing the SNR by one order of

https://doi.org/10.1021/acs.nanolett.4c02425
Nano Lett. 2024, 24, 12374−12381

magnitude for a 100 × 100 pixel movie. The full ChiSCAT algorithm recovers for part of this loss because it searches for an extended pattern of cross-peaks in the Gramian matrix and hence aggregates information from multiple action potentials. Over a wide range of single-pixel signal-to-noise ratios, the resulting performance approaches matched filtering.

In summary, we have demonstrated an unsupervised learning algorithm that can recover action potentials from a microscopy movie, even from a chaotic speckle pattern, without *a priori* information about the timing and the exact spatial pattern of an AP. With this tool at hand, we detect action potentials with interferometric sensitivity in an experimentally simple microscopy scheme. The combination of iSCAT microscopy with speckle illumination is interferometrically sensitive to motion. It harnesses the higher sensitivity that can be achieved in reflective schemes and features common-path rejection of vibrations and a freely tunable illumination wavelength.

Our results also demonstrate that living cells are interferometrically stable for at least a few seconds, evidenced by the fact that the off-diagonal peaks in Figure 4A ("cross-correlation decay") persist for several seconds. APs repeating within this time indeed trigger the same interferometric pattern, which opens a window in which algorithms can be devised to search for repeating signals rather than a known pattern.

The signal-to-noise ratio of our algorithm is inferior to algorithms searching for a known spatial pattern and scales as $\sqrt[4]{N_{px}}$; that is, for a realistic setup having 100 × 100 pixels ChiSCAT will be 10 times less sensitive than matched filtering. The theory predicts that decreasing the number of pixels will improve the SNR, achieving optimality in the limiting case of $N_{px} = 1$. However, this would make distinguishing between an AP signal and random fluctuations impossible, since both of them will exhibit exactly the same spatial pattern (consisting of 1 pixel). This trade-off leads to the existence of an optimal number of pixels for the given experiment, which will need more investigation in future work.

Recovery of signal with the ChiSCAT algorithm depends not only on the number of pixels but also on the density of spikes: the low rank approximation minimizes the sum of squares of residuals; that is, the algorithm will converge to a component that dominates the Gramian matrix. Increasing the number of spikes quadratically increases the number of off-diagonal peaks in the Gramian matrix, helping the algorithm recover the real AP signal. Thus, the theory predicts that the ChiSCAT algorithm can recover even weaker signals if cells spike more often, e.g., in primary neurons.

While our demonstration is based on a speckle-based variant of iSCAT microscopy, the algorithm is agnostic against the imaging scheme employed and could also operate on visually interpretable imaging data sets obtained by, for example, quantitative phase microscopy, ROCS, refractive index tomography, or coherence tomography.[21,31−33] Importantly, it could identify any repeating motion correlating with action potentials, not only motion of the plasma membrane. It could thus discover additional intrinsic signals, such as motion of organelles in response to Ca release, or a lateral motion in the axoplasm which is predicted by a nonstandard theory of action potentials.[34] Still, it is notable that our algorithm can operate even on speckle patterns. This paves the way to detecting action potentials even in scattering tissue including the living brain.

All the experiments have been performed with a custom-built microscope (see SI for details). The commercially available iPS cell line SC950A-1 (Biocat) was cultivated in StemMACS iPS-Brew (Miltenyi Biotech). Once the cells had reached 80% confluence, they were split as aggregates using ReLeSR (Stemcell Technologies) according to the manufacturer's instructions and seeded at a cell density of 20,000 cells/cm^2. For the selection of cardiomyocytes, clones with the αMHC promoter[35] and, for the selection of pacemaker cells, double transfected clones with the TBX3 and αMHC promoter[36] were generated. Four days before the start of differentiation, 20,000 cells/cm^2 were seeded into one well of a six-well plate in StemMACS iPS-Brew. A differentiation protocol was applied. After the end of differentiation, cells were dissociated using the Multi Tissues Dissociation Kit 3 (Miltenyi Biotech) and seeded as single cells for further analyses. See the SI for detailed information about methods.

■ ASSOCIATED CONTENT

Supporting Information

The Supporting Information is available free of charge at https://pubs.acs.org/doi/10.1021/acs.nanolett.4c02425.

Optical setup description, details about numerical and analytical estimation of ChiSCAT algorithm performance (PDF)

■ AUTHOR INFORMATION

Corresponding Author

Friedemann Reinhard − *Institute of Physics, University of Rostock, 18059 Rostock, Germany; Department of Life, Light, and Matter of the Interdisciplinary Faculty at Rostock University, 18059 Rostock, Germany;* orcid.org/0000-0001-6273-7399; Email: friedemann.reinhard@uni-rostock.de

Authors

Andrii Trelin − *Institute of Physics, University of Rostock, 18059 Rostock, Germany; Department of Life, Light, and Matter of the Interdisciplinary Faculty at Rostock University, 18059 Rostock, Germany;* orcid.org/0009-0001-0183-8601

Sophie Kussauer − *Department of Cardiac Surgery, Rostock University Medical Centre, 18057 Rostock, Germany; Department of Life, Light, and Matter of the Interdisciplinary Faculty at Rostock University, 18059 Rostock, Germany*

Paul Weinbrenner − *Institute of Physics, University of Rostock, 18059 Rostock, Germany; Department of Life, Light, and Matter of the Interdisciplinary Faculty at Rostock University, 18059 Rostock, Germany;* orcid.org/0009-0005-4063-124X

Anja Clasen − *Institute of Physics, University of Rostock, 18059 Rostock, Germany; Department of Life, Light, and Matter of the Interdisciplinary Faculty at Rostock University, 18059 Rostock, Germany*

Robert David − *Department of Cardiac Surgery, Rostock University Medical Centre, 18057 Rostock, Germany; Department of Life, Light, and Matter of the Interdisciplinary Faculty at Rostock University, 18059 Rostock, Germany*

Christian Rimmbach − *Department of Cardiac Surgery, Rostock University Medical Centre, 18057 Rostock, Germany; Department of Life, Light, and Matter of the*

Interdisciplinary Faculty at Rostock University, 18059 Rostock, Germany

Complete contact information is available at: https://pubs.acs.org/10.1021/acs.nanolett.4c02425

Author Contributions

C.R. and F.R. contributed equally

Notes

The authors declare no competing financial interest.

■ ACKNOWLEDGMENTS

The authors wish to thank Marten Möller for expert technical assistance. This work has been supported by the Deutsche Forschungsgemeinschaft (DFG) SFB 1477 "LightMatter Interactions at Interfaces", Project No. 441234705. S.K., C.R., and R.D. received funding from the EU Structural Fund (ESF/14-BM-A55-0024/18) and the Federal Ministry for Economic Affairs and Climate Action (16KN083635). In addition, S.K. is supported by the DFG (VA1797/1-1). Moreover, R.D. is supported by the DFG (DA1296/6-1 and GRK 2901 Sylobio), the DAMP Foundation, the German Heart Foundation (F/01/12), the BMBF (VIP+00240), and the BMEL (FKZ: 281A819B21).

■ REFERENCES

(1) Hill, D. K.; Keynes, R. D. Opacity changes in stimulated nerve. *Journal of Physiology* **1949**, *108*, 278−281.
(2) Cohen, L. B.; Keynes, R. D.; Hille, B. Light Scattering and Birefringence Changes during Nerve Activity. *Nature* **1968**, *218*, 438−441.
(3) Iwasa, K.; Tasaki, I.; Gibbons, R. C. Swelling of Nerve Fibers Associated with Action Potentials. *Science* **1980**, *210*, 338−339. Publisher: American Association for the Advancement of Science.
(4) La Porta, A.; Stepnoski, R.; Raccuia-Behling, F.; Kleinfeld, D.; Slusher, R.; Blonder, G. Recording action potential in cultured Aplysia neurons using intrinsic optical signals. *OSA Annual Meeting* **1990**, MPP3.
(5) Stepnoski, R.; LaPorta, A.; Raccuia-Behling, F.; Blonder, G.; Slusher, R.; Kleinfeld, D. Noninvasive detection of changes in membrane potential in cultured neurons by light scattering. *Proceedings of the National Academy of Sciences* **1991**, *88*, 9382−9386.
(6) MacVicar, B. A.; Hochman, D. Imaging of synaptically evoked intrinsic optical signals in hippocampal slices. *J. Neurosci.* **1991**, *11*, 1458−1469.
(7) Kim, G.; Kosterin, P.; Obaid, A.; Salzberg, B. A mechanical spike accompanies the action potential in mammalian nerve terminals. *Biophysical journal* **2007**, *92*, 3122−3129.
(8) LaPorta, A.; Kleinfeld, D. Interferometric detection of action potentials. *Cold Spring Harb. Protoc* **2012**, *2012*, 307−311.
(9) Badreddine, A. H.; Jordan, T.; Bigio, I. J. Real-time imaging of action potentials in nerves using changes in birefringence. *Biomedical optics express* **2016**, *7*, 1966−1973.
(10) Yang, Y.; Liu, X.-W.; Wang, H.; Yu, H.; Guan, Y.; Wang, S.; Tao, N. Imaging action potential in single mammalian neurons by tracking the accompanying sub-nanometer mechanical motion. *ACS Nano* **2018**, *12*, 4186−4193.
(11) Ling, T.; Boyle, K. C.; Goetz, G.; Zhou, P.; Quan, Y.; Alfonso, F. S.; Huang, T. W.; Palanker, D. Full-field interferometric imaging of propagating action potentials. *Light: Science & Applications* **2018**, *7*, 107.
(12) Ling, T.; Boyle, K. C.; Zuckerman, V.; Flores, T.; Ramakrishnan, C.; Deisseroth, K.; Palanker, D. High-speed interferometric imaging reveals dynamics of neuronal deformation during the action potential. *Proceedings of the National Academy of Sciences* **2020**, *117*, 10278−10285.
(13) Mueller, J. K.; Tyler, W. J. A quantitative overview of biophysical forces impinging on neural function. *Physical biology* **2014**, *11*, 051001.
(14) Mosbacher, J.; Langer, M.; Hörber, J.; Sachs, F. Voltage-dependent membrane displacements measured by atomic force microscopy. *J. Gen. Physiol.* **1998**, *111*, 65−74.
(15) González-Pérez, A.; Mosgaard, L. D.; Budvytyte, R.; Villagrán-Vargas, E.; Jackson, A. D.; Heimburg, T. Solitary electromechanical pulses in lobster neurons. *Biophys. Chem.* **2016**, *216*, 51−59.
(16) Choi, W.; Fang-Yen, C.; Badizadegan, K.; Oh, S.; Lue, N.; Dasari, R. R.; Feld, M. S. Tomographic phase microscopy. *Nat. Methods* **2007**, *4*, 717−719.
(17) Zhang, P.-C.; Keleshian, A. M.; Sachs, F. Voltage-induced membrane movement. *Nature* **2001**, *413*, 428−432.
(18) Howe, C. L.; Webb, K. F.; Abayzeed, S. A.; Anderson, D. J.; Denning, C.; Russell, N. A. Surface plasmon resonance imaging of excitable cells. *J. Phys. D: Appl. Phys.* **2019**, *52*, 104001.
(19) Yaqoob, Z.; Yamauchi, T.; Choi, W.; Fu, D.; Dasari, R. R.; Feld, M. S. Single-shot Full-field reflection phase microscopy. *Opt. Express, OE* **2011**, *19*, 7587−7595.
(20) Singh, V. R.; Yang, Y. A.; Yu, H.; Kamm, R. D.; Yaqoob, Z.; So, P. T. C. Studying nucleic envelope and plasma membrane mechanics of eukaryotic cells using confocal reflectance interferometric microscopy. *Nat. Commun.* **2019**, *10*, 3652.
(21) Hu, C.; Popescu, G. Quantitative phase imaging: principles and applications. *Label-Free Super-Resolution Microscopy* **2019**, 1−24.
(22) Taylor, R. W.; Sandoghdar, V. Interferometric scattering microscopy: seeing single nanoparticles and molecules via Rayleigh scattering. *Nano Lett.* **2019**, *19*, 4827−4835.
(23) Piliarik, M.; Sandoghdar, V. Direct optical sensing of single unlabelled proteins and super-resolution imaging of their binding sites. *Nat. Commun.* **2014**, *5*, 4495.
(24) Küppers, M.; Albrecht, D.; Kashkanova, A. D.; Lühr, J.; Sandoghdar, V. Confocal interferometric scattering microscopy reveals 3D nanoscopic structure and dynamics in live cells. *Nat. Commun.* **2023**, *14*, 1962.
(25) Taylor, R. W.; Mahmoodabadi, R. G.; Rauschenberger, V.; Giessl, A.; Schambony, A.; Sandoghdar, V. Interferometric scattering microscopy reveals microsecond nanoscopic protein motion on a live cell membrane. *Nat. Photonics* **2019**, *13*, 480−487.
(26) Mazaheri, M.; Kasaian, K.; Albrecht, D.; Renger, J.; Utikal, T.; Holler, C.; Sandoghdar, V. iSCAT microscopy and particle tracking with tailored spatial coherence. *Optica* **2024**, *11*, 1030−1038.
(27) Hugonnet, H.; Han, H.; Park, W.; Park, Y. Improving Specificity and Axial Spatial Resolution of Refractive Index Imaging by Exploiting Uncorrelated Subcellular Dynamics. *ACS Photonics* **2024**, *11*, 257.
(28) Kukura, P.; Ewers, H.; Müller, C.; Renn, A.; Helenius, A.; Sandoghdar, V. High-speed nanoscopic tracking of the position and orientation of a single virus. *Nat. Methods* **2009**, *6*, 923−927.
(29) North, D. O. An analysis of the factors which determine signal/noise discrimination in pulsed-carrier systems. *Proceedings of the IEEE* **1963**, *51*, 1016−1027.
(30) Kamphorst, J.-P.; Ruelle, D.; et al. Recurrence plots of dynamical systems. *Europhys. Lett.* **1987**, *4*, 17.
(31) Jünger, F.; Olshausen, P. v.; Rohrbach, A. Fast, label-free super-resolution live-cell imaging using rotating coherent scattering (ROCS) microscopy. *Sci. Rep.* **2016**, *6*, 30393.
(32) Charrière, F.; Marian, A.; Montfort, F.; Kuehn, J.; Colomb, T.; Cuche, E.; Marquet, P.; Depeursinge, C. Cell refractive index tomography by digital holographic microscopy. *Optics letters* **2006**, *31*, 178−180.
(33) Huang, D.; Swanson, E. A.; Lin, C. P.; Schuman, J. S.; Stinson, W. G.; Chang, W.; Hee, M. R.; Flotte, T.; Gregory, K.; Puliafito, C. A.; Fujimoto, J. G. Optical Coherence Tomography. *Science* **1991**, *254*, 1178−1181.
(34) El Hady, A.; Machta, B. B. Mechanical surface waves accompany action potential propagation. *Nat. Commun.* **2015**, *6*, 6697.

(35) Klug, M. G.; Soonpaa, M. H.; Koh, G. Y.; Field, L. J. others Genetically selected cardiomyocytes from differentiating embronic stem cells form stable intracardiac grafts. *J. Clin. Invest.* **1996**, *98*, 216−224.
(36) Jung, J. J.; Husse, B.; Rimmbach, C.; Krebs, S.; Stieber, J.; Steinhoff, G.; Dendorfer, A.; Franz, W.-M.; David, R. Programming and isolation of highly pure physiologically and pharmacologically functional sinus-nodal bodies from pluripotent stem cells. *Stem cell reports* **2014**, *2*, 592−605.

https://doi.org/10.1021/acs.nanolett.4c02425
Nano Lett. 2024, 24, 12374−12381

Supplementary information for: ChiSCAT: unsupervised learning of recurrent cellular micro-motion patterns from a chaotic speckle pattern

Andrii Trelin,[†,‡] Sophie Kussauer,[¶,‡] Paul Weinbrenner,[†,‡] Anja Clasen,[†,‡] Robert David,[¶,‡] Christian Rimmbach,[¶,‡,§] and Friedemann Reinhard[*,†,‡,§]

†*Institute of Physics, University of Rostock, 18059 Rostock, Germany*

‡*Department of Life, Light, and Matter of the Interdisciplinary Faculty at Rostock University, 18059 Rostock, Germany*

¶*Department of Cardiac Surgery, Rostock University Medical Centre, 18057 Rostock, Germany*

§*These authors contributed equally*

E-mail: friedemann.reinhard@uni-rostock.de

Setup details

The setup (Fig. 1 (A) in the main text) consists of an illumination laser (473 nm, CNI Laser), which is used for both fluorescence excitation and speckle imaging. Firstly, the laser beam is expanded (to fill the objective aperture) and illuminates holographic diffuser (Luminit, 5° diffisuing angle). Holographic diffusers possess a well defined angle of diffusion, which minimizes the amount of light not captured by lens. Lens 1 (Thorlabs LB1607) is

a simple relay lens which projects illuminated diffuser image onto the objective backfocal plane (BFP), thus creating Fourier-transformed random field (which is still a random field) in the cell plane. An important aspect of projecting to BFP, is that by changing diffuser angle, it is possible adjust the FOV. Reflected blue laser and excited fluorescence are extracted with 50:50 beamsplitter (Thorlabs BS031), and split according to wavelength with dichroic mirror (DM, Thorlabs MD499). The fluorescence channel is additionally filtered with a bandpass filter corresponding to the dye emission (Thorlabs, MF530-43) and focused into EMCCD camera sensor (Princeton Instruments ProEM HS 512x512) with the Lens 2 (Thorlabs LA1708-A). Speckle channel is imaged onto CMOS camera (KronTech Chronos 2.1-HD) with the Lens 3 (Thorlabs AC-508-150).

All experiments were performed at 2000 FPS CMOS camera at resolution 640x480 and 100 FPS of EMCCD camera, i.e. every fluorescence frame was recorded per 20 speckle frames. Laser power was set to 35 mW.

Correlation computation

The correlation between the reconstructed signal and the fluorescence trace, as depicted in Figure 4 (C) in the main text, was determined as follows: Firstly, the cross-correlation between the fluorescence trace and a chunk of the reconstructed signal was computed, and its maximum value was taken. Then, this process was repeated by sliding the chunk along the reconstructed trace, followed by taking globally maximum correlation value. This is necessary to guarantee that correlation is not biased by small shifts between traces or by random events in the trace. The correlation was only computed for subset of experimental data (69 traces in total) where fluorescence measurement was reliable enough.

Power detection

A naive baseline for detecting motion is frequency filtering followed by power detection, i.e. just calculating the rms power over the frequency-filtered frames. This approach is highly sensitive, does not require knowledge of phase in every pixel, but is not specific to repetitive events. Figure S1 compares the ChiSCAT algorithm and supervised learning to power detection, clearly demonstrating its inferiority for the speckle illuminated cell data.

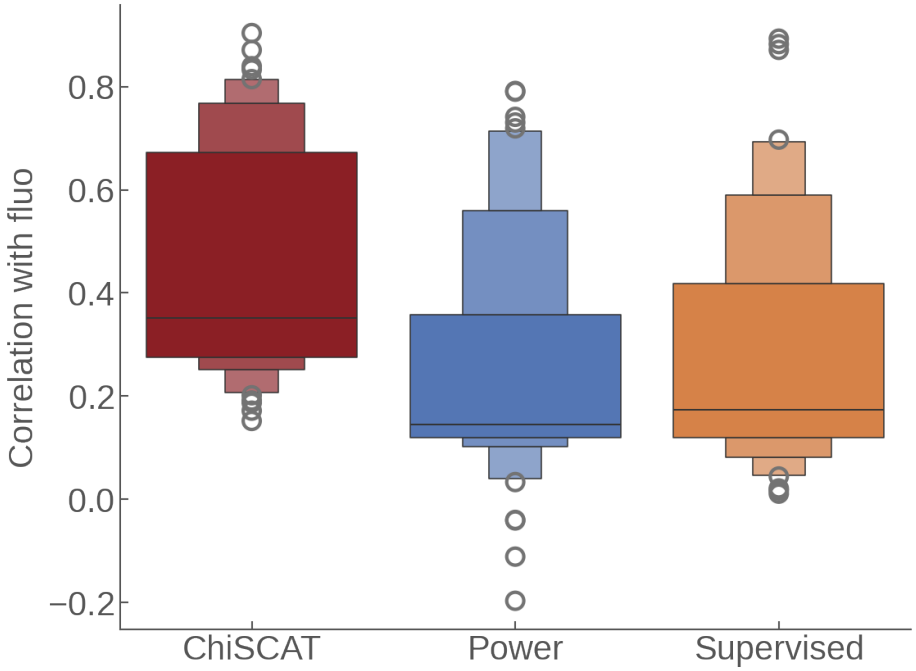


Figure S1: Extended version of Fig. 4 (C) from the main text, including power detection algorithm

Modeling of the signal-to-noise-ratio (SNR) of ChiSCAT

Toy model for SNR analysis (Fig. 4 D main manuscript)

To estimate the signal-to-noise ratio that can be obtained by the ChiSCAT algorithm, we employ a simple toy model of the signal obtained after the initial matched filtering step. We model the matched-filtered speckle movie as a sum of photonic shot noise, represented

by a series of frames where every pixel is drawn from a normal distribution with standard deviation $\sigma = 1$, and synthetic action potentials, modeled by a repeating signal-pattern $\vec{p}$ that is added to specific selected frames. The signal pattern $\vec{p}$ is equally drawn from a normal distribution, which however has a different standard deviation $\sigma = \mathrm{SNR}_{1\mathrm{px}}$ and is moreover identical for all signal frames. Note that action potentials are modeled as delta-function events, which is an approximation. We will denote the frames of the resulting synthetic data movie as $\vec{f}_i$.

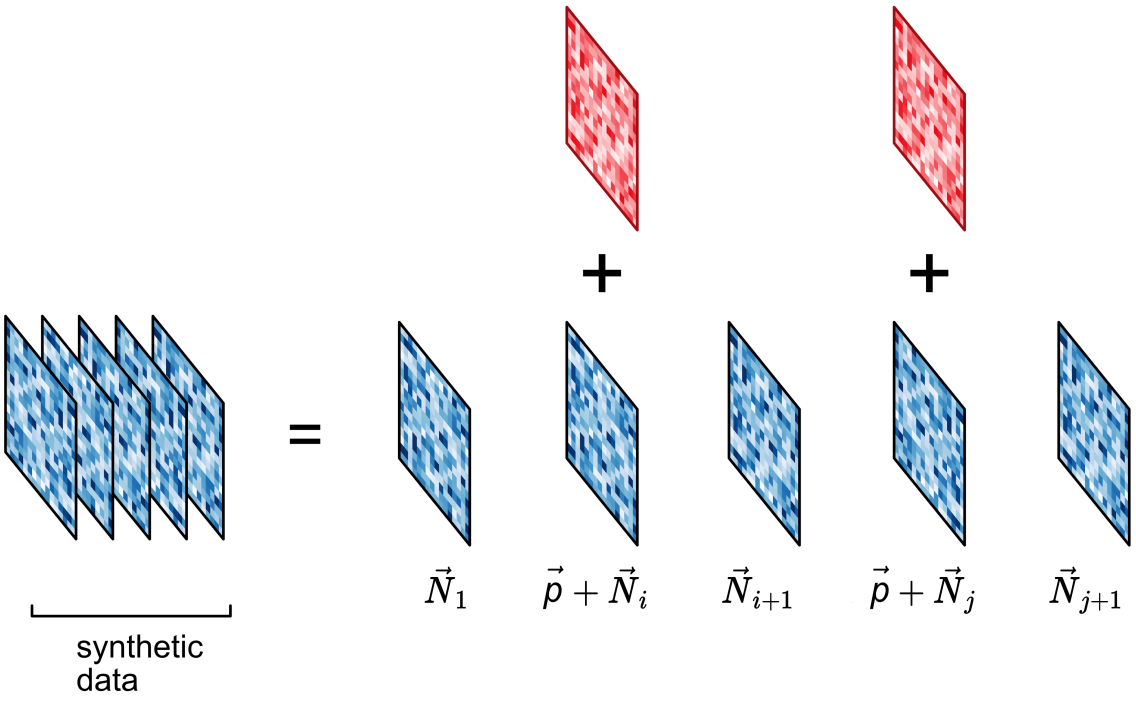


Figure S2: Toy model of data for the signal-to-noise-analysis (Fig. 4 D main text). A matched-filtered speckle movie is approximated as a series of noise frames $\vec{N}_k$, where every pixel is drawn from a normal distribution with variance $\sigma = 1$. A repeating signal-pattern $\vec{p}$ is added to specific selected frames (denoted i and j) to model action potentials. This signal pattern $\vec{p}$ is drawn from a normal distribution with $\sigma = \mathrm{SNR}_{1\mathrm{px}}$ but is identical for all signal frames. Note that pixel values can be negative because we model the movie after an initial step of matched filtering.

We analyze this synthetic data in three ways:

1. by simulated spatial matched filtering with the perfect signal template $\vec{p}$, i.e. computing

the time series $r_i = \vec{f_i} \cdot \vec{p}$.

2. by computing a single column of the Gramian matrix at a signal frame $\vec{f_k}$, i.e. computing the time series $r_i = \vec{f_i} \cdot \vec{f_k}$.

3. by running the full ChiSCAT algorithm, i.e. computing the Gramian matrix $\vec{f_i} \cdot \vec{f_k}$, erasing its diagonal and computing the largest eigenvector as a rank-one approximation.

For each of these time series, we extract the signal strength by calculating $\vec{r_j}$ at a signal frame j, and we extract the background noise by numerically calculating the standard deviation of $\vec{r_i}$ in a signal-free time window.

Analytical estimate of SNR

One explicit design feature of ChiSCAT is to only use minimal *a priori* information. In particular, we do not assume knowledge of the perfect signal pattern $\vec{p}$. This feature comes at a price, which is a performance overhead compared to algorithms like matched filtering, which assume knowledge of the signal pattern. Quantitatively, this loss can be estimated by comparing the SNR of a single off-diagonal peak in the Gramian matrix to the SNR obtained in perfect matched filtering. The strength of an off-diagonal Gramian peak is the scalar product between two signal frames i and j

$$\vec{f_i} \cdot \vec{f_j} = (\vec{p} + \vec{N_i}) \cdot (\vec{p} + \vec{N_j}) \approx \vec{p} \cdot \vec{p} + \vec{N_i} \cdot \vec{p} + \vec{N_j} \cdot \vec{p} + \vec{N_i} \cdot \vec{N_j}$$

where the first term $\vec{p} \cdot \vec{p}$ constitutes the signal, and the latter three terms constitute noise. For the most relevant parameter range $\mathrm{SNR}_{1\mathrm{px}} < 1$, the dominant noise term is the last term $\vec{N_i} \cdot \vec{N_j}$. The strength of a signal peak in matched filtering is the scalar product of a signal frame with the perfect pattern $\vec{p}$

$$\vec{f_i} \cdot \vec{p} = (\vec{p} + \vec{N_i}) \cdot \vec{p} \approx \vec{p} \cdot \vec{p} + \vec{N_i} \cdot \vec{p}.$$

Again, the first term constitutes the signal, the latter term the noise.

We now estimate the strength of all individual terms appearing in the expressions above.

- $\langle \vec{p} \cdot \vec{p} \rangle = \mathrm{SNR}_{1\mathrm{px}}^2 N_{\mathrm{px}}$, because for every pixel p_m of $\vec{p}$, the product p_m^2 is a random variable drawn from a chi-square distribution with mean value $\mathrm{SNR}_{1\mathrm{px}}^2$.
- $\langle \vec{p} \cdot \vec{N}_i \rangle = 0, \sqrt{\left\langle \left(\vec{p} \cdot \vec{N}_i \right)^2 \right\rangle} = \mathrm{SNR}_{1\mathrm{px}} \sqrt{N_{\mathrm{px}}}$. For every pixel the product of $\vec{p}$ and N_i is the product of two uncorrelated Gaussian random variables, with variances $\sigma_p^2 = \mathrm{SNR}_{1\mathrm{px}}^2$ and $\sigma_i^2 = 1$. The variance of the product is known to be $\sigma_{\mathrm{product}}^2 = \sigma_p^2 \sigma_j^2 = \mathrm{SNR}_{1\mathrm{px}}^2$.
- $\langle \vec{N}_i \cdot \vec{N}_j \rangle = 0, \sqrt{\left\langle \left(\vec{N}_i \cdot \vec{N}_j \right)^2 \right\rangle} = \sqrt{N_{\mathrm{px}}}$. Similarly, for every pixel the product of N_j and N_i is the product of two Gaussian random variables, with variances $\sigma_i^2 = 1$ and $\sigma_j^2 = 1$. The variance of the product is thus $\sigma_{\mathrm{product}}^2 = \sigma_i^2 \sigma_j^2 = 1$.

With these expressions, the condition SNR > 1 for matched filtering translates into the equation

$$\vec{p} \cdot \vec{p} > \sqrt{\left\langle \vec{p} \cdot \vec{N}_i \right\rangle^2} \tag{1}$$

$$\mathrm{SNR}_{1\mathrm{px}} > \frac{1}{\sqrt{N_{\mathrm{px}}}} \tag{2}$$

consistent with the intuition that averaging over N_{px} pixels improves the SNR by $\sqrt{N_{\mathrm{px}}}$.

In contrast, the condition SNR > 1 for the initial step of ChiSCAT reads

$$\mathrm{SNR}_{1\mathrm{px}}^2 \sqrt{N_{\mathrm{px}}} > 1 \tag{3}$$

$$\mathrm{SNR}_{1\mathrm{px}} > \frac{1}{\sqrt{N_{\mathrm{px}}}} \cdot \sqrt[4]{N_{\mathrm{px}}} \tag{4}$$

$$\tag{5}$$

Compared to matched filtering, there is an overhead of $\sqrt[4]{N_{\mathrm{px}}}$ in terms of SNR, which can be partially recovered in the final step of ChiSCAT by merging information from multiple

action potentials.

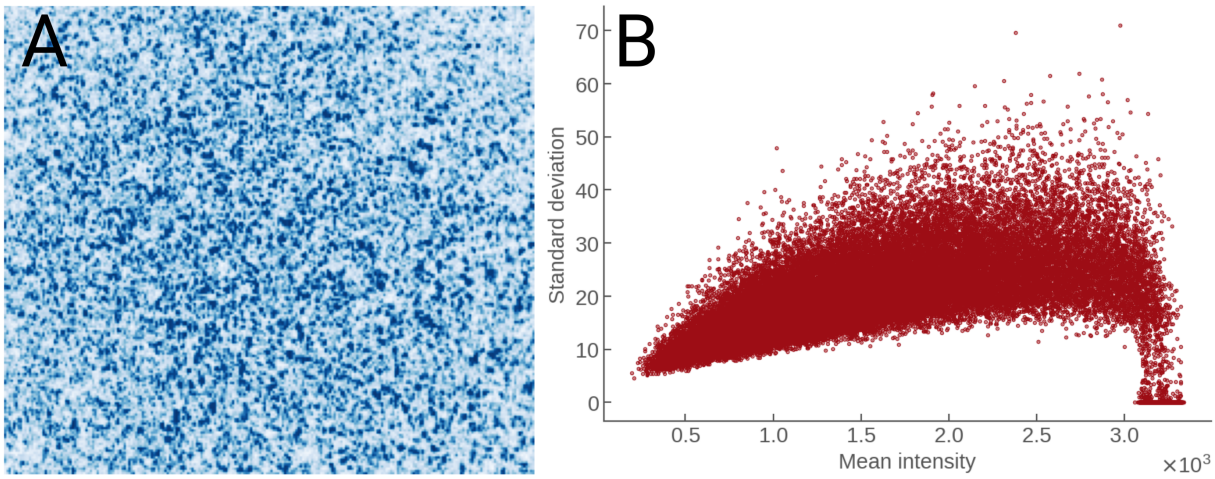


Figure S3: (A) Example of the intensity distribution of a speckle pattern as captured by the camera. (B) Standard deviation of individual pixel intensities over time as a function of pixel intensity. The decrease in standard deviation at higher intensity values is due to pixel saturation.

Numerical estimate of SNR

To estimate the ultimate resolution that can be achieved by our scheme, we calculated the expected signal-to-noise ratio (SNR) for detecting a 1 nm membrane motion using the proposed approach. The following methodology was employed. First, a speckle video of the empty sample was recorded under standard conditions and the relative noise $\sigma_{r,px}$ in the signal of a single pixel was computed. The relative noise is $\sigma_{r,px} = \sigma_{I,\mathrm{BW}}/\langle I \rangle$, where $\sigma_{I,\mathrm{BW}}$ is the variance of the single-pixel intensity in the frequency band corresponding to action potentials (100–500 Hz, note that we assume the shorter timescale of action potentials of a neuron here, as opposed to cardiomyocytes in the main manuscript) and $\langle I \rangle$ the mean intensity of the pixel. While the exact value of $\sigma_{r,px}$ is highly heterogeneous between pixels due to the speckle nature of the signal, its full-frame average value is 0.56% at an illumination power of 1.7 mW.

Next, the relative signal change, $\Delta I_{\mathrm{AP}}/I$, corresponding to a 1 nm motion, was calculated

as

$$\frac{\Delta I_{\mathrm{AP}}}{I} = \frac{\Delta z}{\lambda/(2n_{med})} c_r$$

Here, Δz represents the membrane motion amplitude, n_{med} is the refractive index of the medium, and λ is the laser wavelength. The factor of 1/2 accounts for the double pass of the light beam in the reflection geometry. The term $c_r = 2\sqrt{\alpha}/(1+\alpha)$ represents the relative contrast, indicating the maximum possible change in reflected signal intensity for given reflectivities. This contrast can be derived from the wave interference equation

$$I = I_1 + I_2 + 2\sqrt{I_1 I_2}\cos(\Delta\phi)$$

by dividing the amplitude of the interference term, $2\sqrt{I_1 I_2}$, by the static intensity, $I_1 + I_2$, and assuming $I_2 = \alpha I_1$, where α is the ratio of the intensities of the signal reflected from the coverslip to that reflected from the cell, allows us to express c_r. The value of $\alpha \approx 0.055$ can be derived from the Fresnel equation, relating reflection coefficient for transition from medium 1 to medium 2 to their refractive indices $r_{12} = (n_1 - n_2)^2/(n_1 + n_2)^2$. In our case, $\alpha = r_{\text{med-cell}}/r_{\text{cs-med}}$ is a ratio of reflectivities r on medium-cell interface ($n_{\mathrm{med}} = 1.34$, $n_{\mathrm{cell}} = 1.38$) and coverslide-medium interface ($n_{\mathrm{med}} = 1.34$, $n_{\mathrm{cs}} = 1.52$). By substituting the corresponding values ($\Delta z = 1$ nm, $n_{\mathrm{med}} = 1.34$, $\lambda = 473$ nm, $c_r = 0.443$ in the equation for $\Delta I_{\mathrm{AP}}/I$, the relative signal intensity change is found to be approximately 0.25%.

Finally, the SNR is calculated as:

$$\mathrm{SNR} = \frac{\Delta I_{\mathrm{AP}}/I}{\sigma_{r,\mathrm{px}}} \sqrt[4]{N_{px}} \approx 4.5$$

It is important to note that due to the slower scalability of the ChiSCAT algorithm compared to the ideal match filtering, the SNR scales with the fourth root of the number of pixels (assuming 100×100 pixels) rather than the square root. Despite that, the SNR remains significantly greater than 1, demonstrating the capability of ChiSCAT to detect 1 nm motion, even without accounting for the ChiSCAT algorithm's ability to aggregate

information from multiple APs.

Methods

Differentiation protocols for human iPS cells to generate CM mainly result in a mixtures of the three subtypes, with ventricular CMs predominating and atrial and pacemaker cells underrepresented. We have focused on the function of cardiac transcription factors that regulate both cardiogenesis during embryonic development and the cardiac differentiation of pluripotent stem cells. The principle of cardiomyocyte subtype-specific stem cell programming by overexpression of transcription factors (forward programing) was used to program pluripotent stem cells into previously unobserved aggregates of pacemaker cells.[1–3] Electrophysiological parameters like the peak voltages of an action potential, its duration, or its delay with respect to Calcium release and contraction, are highly important observables to characterize the cell type and function, but currently require electrophysiology or invasive labels to be observed.

Cultivation of human induced pluripotent cells

The commercially available iPS cell line SC950A-1 (Biocat) was cultivated in StemMACS iPS-Brew (Miltenyi Biotech). Cell culture vessels were coated with Laminin 521 (Biolamina) according to the manufacturer's instructions. Once the cells had reached 80% confluence, they were split as aggregates using ReLeSR (Stemcell technologies) according to the manufacturer's instructions and seeded at a cell density of 20,000 cells/cm2. Medium was changed daily.

Generation of stable IPS clones

For the selection of cardiomyocytes, clones with the αMHC promoter (Klug et al. 1996) and for the selection of pacemaker cells, double transfected clones with TBX3 and αMHC

promoter[1,2] were generated as follows:

One hour before nucleofection, the medium was removed and fresh StemMACS iPS-Brew containing 10 µM Rock inhibitor and 10% Nate (Invivogen) was added.

For nucleofection, the cells were separated in the following way: Medium was removed and cells were washed with PBS. The cells were then detached with Accutase (37°C, 5 min) and separated. After the addition of DMEM, the cells were removed from the culture vessel and transferred to a centrifuge tube. The cell suspension was centrifuged (5 min, 300xg) and the pellet was resuspended in IPS Brew with 10 µM Y-27632.

For nucleofection, 100000 cells were taken up in buffer P3 with supplement 1 (Lonza) and 5 µg endotoxin-free plasmid DNA (αMHC promoter or TBX3) was added.

Transfection was performed in the 4D Nucleofector (Lonza) using the CB150 programme. The cells were seeded at a density of 65,000 cells/cm2 in StemMACS iPS-Brew with 10 % CloneR (Stem cell technologies) and cultured for 24 h. The cells were then selected with 100 µg/ml hygromycin B (cardiomyocytes; αMHC promoter). Subsequently, selection was performed with 100 µg/ml hygromycin B (cardiomyocytes; αMHC promoter) or 100 µg/ml hygromycin B and 10 µg/ml blasticidin (pacemaker cells; TBX3, αMHC promoter). Individual clones were harvested and propagated.

Differentiation

In all steps the medium was changed daily, before each change to a different medium the cells were rinsed twice with PBS. Four days before the start of differentiation, 20000 cells/cm2 were seeded into one well of a 6 well plate in StemMACS iPS-Brew.

On day 1 of differentiation, the medium was changed to RPMI with B27 without insulin (Thermo Fisher), 200 µM ascorbic acid, 5 ng/µl FGF2, 1µM CHIR99021, 5 ng/µl BMP4 and 9 ng/µl Activin A. From day 4, the cells were differentiated in RPMI with B27 with insulin, 200 µM ascorbic acid and 5 µM IWP2. On day 10, a switch was made to RPMI with B27 with insulin and 200 µM ascorbic acid. The selection of cardiomyocytes (beginning on day 14)

was performed in RPMI with B27 with insulin, 200 µM ascorbic acid with 200 µg/ml G418. On day 18, cardiomyocytes were detached using the Cardiomyocyte Isolation Kit (Stemcell technologies), seeded into one well of a 24 well and cultured in Cardiomyocyte Maintenace Medium (Stemcell Technologies). Once these had formed a stable contracting syncytium, they were dissociated using the Multi Tissues Dissociation Kit 3 (Miltenyi Biotech) and seeded as single cells for further analyses.

Nomenclature

Data variables

$\vec{f}$ Single frame of video, represented as 1D vector

a_{el} Elementary AP pattern (single AP spike)

a_{MF} AP trace reconstructed with matched filtering

I_{AP} AP component of single frame of video (), represented as 1D vector

Physical variables

$a(t)$ 1D AP time trace

E_{AP} Field scattered from cellular components varying along the AP

E_{fluct} Field scattered from other moving parts of the cell such as diffusing vesicles

E_{static} Field reflected from the cover slide and static parts of the cell

I_{AP} Static speckle pattern corresponding to spatial distribution of pixel sensitivity to AP-associated cellular movements

I_{el} Dynamic speckle pattern given by tensor product of I_{AP} with a_{el}

I_{noise} Dynamic speckle pattern corresponding to non-AP-associated cellular movements and random noise

I_{static} Static background in light intensity observed by camera

References

(1) Jung, J. J.; Husse, B.; Rimmbach, C.; Krebs, S.; Stieber, J.; Steinhoff, G.; Dendorfer, A.; Franz, W.-M.; David, R. Programming and isolation of highly pure physiologically and pharmacologically functional sinus-nodal bodies from pluripotent stem cells. *Stem cell reports* **2014**, *2*, 592–605.

(2) Rimmbach, C.; Jung, J. J.; David, R. Generation of murine cardiac pacemaker cell aggregates based on ES-cell-programming in combination with Myh6-promoter-selection. *JoVE (Journal of Visualized Experiments)* **2015**, e52465.

(3) Yavari, A.; Bellahcene, M.; Bucchi, A.; Sirenko, S.; Pinter, K.; Herring, N.; Jung, J. J.; Tarasov, K. V.; Sharpe, E. J.; Wolfien, M.; others Mammalian γ2 AMPK regulates intrinsic heart rate. *Nature communications* **2017**, *8*, 1258.

5.2 *When can we see micromotion? Experimental and theoretical analysis of the ChiSCAT scheme*

Authored by **Andrii Trelin**, Jette Abel, Christian Rimmbach, Robert David, Andreas Hermann, and Friedemann Reinhard
Journal: ArXiv, Applied Optics (under review at the moment of writing)
Published: under review
DOI: 10.48550/arXiv.2412.03365
Reference: [180]

When can we see micromotion? Experimental and theoretical analysis of the ChiSCAT scheme

ANDRII TRELIN,[1,2] JETTE ABEL,[3] CHRISTIAN RIMMBACH,[2,4] ROBERT DAVID,[2,4] ANDREAS HERMANN,[3,5] FRIEDEMANN REINHARD,[1,2,*]

[1] *Institute of Physics, University of Rostock, 18059 Rostock, Germany*
[2] *Department of Life, Light, and Matter of the Interdisciplinary Faculty at Rostock University, 18059 Rostock, Germany*
[3] *Translational Neurodegeneration Section „Albrecht Kossel", Department of Neurology, University Medical Center Rostock, University of Rostock, Rostock, Germany*
[4] *Department of Cardiac Surgery, Rostock University Medical Centre, 18057 Rostock, Germany*
[5] *Center for Transdisciplinary Neurosciences Rostock (CTNR), University Medical Center Rostock, Rostock, Germany*
[*] *friedemann.reinhard@uni-rostock.de*

Abstract: We present an in-depth analysis of ChiSCAT, a recently introduced interferometric microscopy scheme to detect recurring micromotion events in cells. Experimentally, we demonstrate that illumination with low-coherence sources can greatly improve the robustness of the scheme to vibrations. Theoretically, we analyze the performance of ChiSCAT under various noise models, in particular photon shot noise and noise dominated by cellular motions other than the signal. We finally propose ways to improve performance, especially in a setting dominated by cell motions, and conclude with an outlook on potential future directions.

1. Introduction

Some evidence suggests that action potentials of electro-active cells like neurons or cardiomyocytes can be detected by label-free interferometric microscopy, because they are accompanied by "intrinsic optical signals", such as a nanometer-scale motion of the cell membrane [1–15].

Recently, we proposed ChiSCAT [16], a combination of interferometric microscopy scheme with eigendecomposition-based algorithm, which allowed experimental detection of APs in a non-neuronal cell culture of blebbistatin-paralyzed cardiomyocytes.

In this article we aim to analyze the technical and fundamental limits of this scheme, with insights from the latter that generalize to a wide range of other interferometric microscopy schemes.

Our work is organized as follows: we firstly analyze the experimental noise in our setup, finding that a major improvement is possible by using low-coherence light for the illumination. We go on to theoretically analyze the sensitivity that ChiSCAT can reach. Since this depends critically on the type of noise the scheme is subjected to, we explicitly compare two prototypical settings: photonic shot noise and noise from cellular background motions other than the signal. We find that cell noise presents a more serious challenge than shot noise, and propose ways to improve the robustness of the ChiSCAT scheme in this setting.

2. Experimental characterization of noise sources

The task of detecting action potentials (APs) in electrically active cells from an interferometric microscopy recording is complicated by various noise sources. Shot noise, originating from the inherent statistics of photon detection, defines a fundamental limit of motion sensitivity for any interferometric scheme. Even if detection is possible within the shot noise limit, other noise sources can dominate and mask an AP signal. For example, cell motion noise, which arises from the inherent random micromotion of the cellular structures can mask a sub-nanometer AP signal, and so can vibrations of the setup. The ChiSCAT setup (Fig. 1), used in our experiments

is based on wide-field interferometric scattering microscopy (iSCAT [17]) and uses coherent light to illuminate the cell. The light wavefront is randomized by a holographic diffuser to create a 3D random light field in the cell volume and to employ the full numerical aperture (NA) of the microscope for illumination. The observed signal is recorded by the high-speed camera (KronTech Chronos 2.1-HD) and consists of a superposition of speckle patterns arising from different components of the cell, interfering with light reflected at the cover slide interface, making it interferometrically sensitive to cellular motion.

Thus, it is critical to develop an understanding of the different noise components and their properties. To obtain such an understanding, we will now compare ChiSCAT measurements with and without cells, in order to gauge cell noise, and using different illumination sources, in order to gauge their intensity fluctuations and their sensitivity to vibrations. The impact of vibrations is expected to depend on the illumination source. A source with a short coherence length will only create interference between closely spaced surfaces, i.e. the cell and the cover slide. In contrast, a source with a long coherence length interference can occur even between widely separated vibrating surfaces, such as different optical elements in the beam path.

Specifically, the ChiSCAT setup (Fig. 1) was utilized to perform measurements with different illumination sources, namely a diode-pumped 473 nm laser (DPSS, CNI Lasers MBL-FN-473-50mW, coherence length ≈25 mm), a 450 nm laser diode (Thorlabs LP450-SF25, coherence length ≈50 μm), and a 650 nm superluminescent diode (SLD, Thorlabs SLD650T, coherence length ≈25 μm). To manage vibrations, the whole setup was built on top of high-quality optical table (Thorlabs T1020Q) and every equipment that might generate vibrations was mechanically decoupled. Three measurements were conducted for each type of laser: directly illuminating the camera sensor (direct), ChiSCAT microscopy without the cell but with a Petri dish containing water (setup), and with a living neuron that was not electrically active (cell). Induced pluripotent stem cells (iPSC) derived human neurons have been used in this experiment. All measurements were performed by continuously running the lasers at full power, allowing a 10-minute warm-up period before measurement to minimize noise. Appropriate illumination intensity was set using neutral density and polarization filters. Results of these experiments are presented in Fig. 2.

In the upper row, the temporal standard deviation of every pixel of the high-speed recording is plotted against the corresponding pixel intensity. It can be observed that direct illumination of the camera sensor results in an almost perfect narrow band, demonstrating a $\sqrt{I}$ behavior, as predicted by the properties of shot noise. When the laser passes through the complete microscopy setup without a cell, the standard deviation increases. This is attributed to the sensitivity of the interferometric setup to vibrations, which is evident in the Fourier-transformed time traces (bottom row) as narrow peaks corresponding to different vibrational modes of the setup. The increase in noise for the blue DPSS laser illumination is the most pronounced, due to the long coherence length of that laser, which captures interference between reflections from more distant surfaces, such as between lenses in the objective.

However, an even more significant difference occurs when a living cell is introduced into the setup. The scatter plots demonstrate an increase in the pixel standard deviation by an order of magnitude. Additionally, the spectra indicate the presence of a Brownian noise-like background, reflecting the actual Brownian motion occurring within the cell. This leads to the conclusion that while the setup operates close to the shot noise limit, the noise introduced by the cell is considerably higher than this limit.

3. Theoretical limits for AP detection

3.1. Shot noise limited case

To understand the fundamental limitations of ChiSCAT approach, it is necessary to derive theoretical criteria of signal recovery. We will first consider the simplest case, that the AP detection performance of ChiSCAT is limited by shot noise. In this assumption, the AP signal is

the only micromotion produced by the cell, and the only noise source present is the photon shot noise in the video recording. In this subsection, we will develop a model to analyze under which conditions the AP signal can be recovered from the measurements in this setting.

Signal model and assumptions

1. In ChiSCAT the reflected laser intensity is recorded as a video F. By flattening the frame dimension, this video can be represented as matrix of size $(N_{\text{fr}}, N_{\text{px}})$, that consists of a static background B, an action potential pattern P that occurs recurrently, and shot noise N:

$$F = B + P + N$$

   To simplify analysis, it can be assumed that the video is centered by subtracting the constant background ($B = 0$).

2. The action potential signal P can be decomposed into a spatial pattern $\boldsymbol{p}$ of size (N_{px}) and a temporal pattern $\boldsymbol{a}$ of size (N_{fr}):

$$P = \boldsymbol{a}\boldsymbol{p}^\intercal$$

   The video is supposed to be scaled such that the amplitude of $\boldsymbol{a}$ is 1. The spatial pattern is assumed to be binary, with $p_i \in \{-1, 1\}$, where both values have an equal probability of 0.5. This reflects the varying sensitivity of the pixels to cellular motion. The pattern is zero-centered as it does not affect the total intensity of the observed signal.

3. Every element of the noise matrix N_{ij} is independently and identically distributed (i.i.d.), approximately Gaussian, with a variance of σ^2_{1px}. Due to the above rescaling to unit signal amplitude, $1/\sigma_{\text{1px}}$ is the signal-to-noise ratio (SNR) obtained if the AP is reconstructed from a single-pixel time trace, whereas σ_{1px} is the noise in this single-pixel trace.

Algorithm The ChiSCAT algorithm, proposed in [16], relies on the eigendecomposition of the Gram or covariance matrix $G = FF^\intercal$ (both terms used interchangeably). Note that the original algorithm contains an additional step of erasing the diagonal of G, which we will neglect in the following derivation. The algorithm makes an assumption that the first eigenvector $\boldsymbol{v}$ of G approximates the true temporal pattern $\boldsymbol{a}$. To demonstrate this, the matrix G can be decomposed into components as follows:

$$\begin{aligned} G = FF^\intercal &= (P + N)(P + N)^\intercal \\ &= PP^\intercal + PN^\intercal + NP^\intercal + NN^\intercal. \end{aligned} \tag{1}$$

In the absence of the noise ($N = 0$), it holds that

$$G = PP^\intercal = (\boldsymbol{a}\boldsymbol{p}^\intercal)(\boldsymbol{a}\boldsymbol{p}^\intercal)^\intercal = \boldsymbol{a}\boldsymbol{p}^\intercal\boldsymbol{p}\boldsymbol{a}^\intercal = \|\boldsymbol{p}\|^2\boldsymbol{a}\boldsymbol{a}^\intercal$$

i.e. that G is essentially the outer product of $\boldsymbol{a}$ with itself, a rank-1 matrix for which the first eigenvector corresponds to $\boldsymbol{a}$ (up to a scaling constant). However, this ideal scenario does not hold when noise is present. Under such conditions, the first eigenvector might or might not correlate with the true signal $\boldsymbol{a}$. We will refer to the random matrix theory to understand conditions at which largest eigenvector actually bears information about true AP.

Recovery criterion In scenarios where the observed matrix is the sum of a low-rank matrix and random noise, spiked random matrix theory [18] can be utilized to establish criteria for signal recovery, specifically criteria for when the signal-to-noise ratio (SNR) of the recovered signal exceeds one. A useful model in this context is the spiked Wigner model, a sum of rank-1 outer product matrix $\boldsymbol{x}\boldsymbol{x}^\intercal$ with noise, given by:

$$Y = \lambda \boldsymbol{x}\boldsymbol{x}^\intercal + \frac{1}{\sqrt{n}} W \tag{2}$$

where $\boldsymbol{x}$ is a unit vector, W represents a symmetric random matrix of size $n \times n$ with independent and identically distributed (i.i.d) random entries with unit variance. This model closely resembles the expression in Eq. 1. Specifically, $\lambda \boldsymbol{x}\boldsymbol{x}^\intercal$ is comparable to PP^T, the noise matrix W is analogous to $NN^\intercal$, while n corresponds to N_{fr}. The cross components $PN^\intercal + NP^\intercal$ are sparse (since $\boldsymbol{a}$ is sparse) and small in the low SNR regime, which is our primary focus. We will thus neglect them, and will later confirm this assumption by a numerical simulation (Fig. 3).

The most important finding from [18] indicates that recovery is possible when $\lambda > 1$, which *de-facto* answers the question. To explicitly connect Eq. 1 to the spiked Wigner model one can multiply both sides of by $\frac{1}{\sqrt{N_{\mathrm{fr}}}} \frac{1}{\sqrt{N_{\mathrm{px}}}\sigma_{\mathrm{1px}}^2}$, leading to

$$\frac{1}{\sqrt{N_{\mathrm{fr}}}} \frac{1}{\sqrt{N_{\mathrm{px}}}\sigma_{\mathrm{1px}}^2} G = \frac{1}{\sqrt{N_{\mathrm{fr}}}} \frac{\|\boldsymbol{p}\|^2 \|\boldsymbol{a}\|^2}{\sqrt{N_{\mathrm{px}}}\sigma_{\mathrm{1px}}^2} \Big(\frac{\boldsymbol{a}}{\|\boldsymbol{a}\|} \frac{\boldsymbol{a}^\intercal}{\|\boldsymbol{a}\|} \Big) + \frac{1}{\sqrt{N_{\mathrm{fr}}}} \frac{1}{\sqrt{N_{\mathrm{px}}}\sigma_{\mathrm{1px}}^2} NN^\intercal .$$

Then, the matrix $\frac{1}{\sqrt{N_{\mathrm{px}}}\sigma_{\mathrm{1px}}^2} NN^\intercal$ is a random symmetric matrix with unit standard deviation (which follows from the fact that entries in $NN^\intercal$ have standard deviation $\sqrt{N_{\mathrm{px}}}\sigma_{\mathrm{1px}}^2$ since it's a sum of N_{px} products of independent random variables in N, each having standard deviation σ_{1px}). Note that $\frac{\boldsymbol{a}}{\|\boldsymbol{a}\|}$ is a unit vector, thus the rescaled equation can be identified with Eq. 2. That translates the recovery criterion to:

$$\lambda = \frac{1}{\sqrt{N_{\mathrm{fr}}}} \frac{\|\boldsymbol{p}\|^2 \|\boldsymbol{a}\|^2}{\sqrt{N_{\mathrm{px}}}\sigma_{\mathrm{1px}}^2} = \frac{\|\boldsymbol{p}\|^2 \|\boldsymbol{a}\|^2}{\sqrt{N_{\mathrm{px}}}\sigma_{\mathrm{1px}}^2} > 1$$

which under the assumptions $\|\boldsymbol{p}\|^2 = N_{\mathrm{px}}$, $\|\boldsymbol{a}\|^2 = N_{\mathrm{ap}}$ can be reformulated as

$$\sigma_{\mathrm{1px}} < \frac{\sqrt{N_{\mathrm{ap}}} \sqrt[4]{N_{\mathrm{px}}}}{\sqrt[4]{N_{\mathrm{fr}}}} =: \sigma_{\mathrm{crit}}. \tag{3}$$

which also matches the empirically observed one in [16].

Numerical simulation To further verify the validity of the derivation, a numerical simulation was performed to analyze dependence of the SNR of signal, recovered with ChiSCAT algorithm on σ_{1px}. Specifically, a vector $\boldsymbol{p}$ of length N_{px} was randomly generated from a $\{-1, 1\}$ distribution. A vector $\boldsymbol{a}$ was simulated by randomly setting N_{ap} entries to 1 in an array composed of N_{fr} zeros. The video F was then created as the outer product of the spatial and temporal patterns $F = \boldsymbol{a} \otimes \boldsymbol{p} + N$, where each element of the matrix N follows a normal distribution $\sim \mathcal{N}(0, \sigma_{\mathrm{1px}})$. With the matrix F obtained, the Gram matrix was computed as $G = FF^\intercal$, from which the first eigenvector $\boldsymbol{v}$ was determined. To calculate the numerical SNR, the eigenvector was decomposed into the linear basis of $\boldsymbol{a}$ and the remaining noise as $\boldsymbol{v} = \alpha \boldsymbol{a} + \boldsymbol{\varepsilon}$. Consequently, the final simulation result, SNR, is expressed as $\mathrm{SNR} = \alpha / \mathrm{std}(\boldsymbol{\varepsilon})$.

To assess the validity of Eq. 3, simulations were performed for randomly sampled parameters with N_{ap} ranging from 3 to 200, N_{fr} from 100 to 2000, and N_{px} from 2000 to 5000. For each combination of $N_{\mathrm{ap}}, N_{\mathrm{px}}, N_{\mathrm{fr}}$, the value σ_{1px} was varied from $0.25\sigma_{\mathrm{crit}}$ to $2\sigma_{\mathrm{crit}}$. The results of this simulation are illustrated in Fig. 3, which clearly show a transition happening around $\sigma_{\mathrm{1px}} = \sigma_{\mathrm{crit}}$.

Implications For a realistic scenario one can assume $N_{\mathrm{ap}} = 10, N_{\mathrm{fr}} = 1000$ (given that the speckle signal is stable on the timescale on the order of 1 s and the camera framerate is on the order of 1000 FPS), $N_{\mathrm{px}} = 2000$, where N_{px} is defined by the number of resolved points in a 10 μm cell. In this case, $\sigma_{\mathrm{crit}} \approx 3.7$. ChiSCAT could thus reveal an action potential even if its amplitude is 3.7 times less than the noise in a single-pixel time trace. For larger cells, such as Purkyně cells which range in size from 60 to 80 μm [19] and correspond to approximately 60,000 resolved points, signal detection is achievable when $\sigma_{1\mathrm{px}} < 8.8$.

3.2. Cell noise limited case

Shot noise defines the ultimate fundamental limit of sensitivity, but might not be reached in practice, since cellular motions other than the AP (arising from the random movement or active transport of scatterers within the cell) can potentially mask the signal. To assess the effect of such cell noise, we will now study a modified signal model where shot noise in the detection is completely neglected, but multiple motion patterns are present in the cell, aiming to analyze recovery criteria in this case.

Signal model and assumptions The model outlined previously considers only shot noise as the primary noise source. To take into account contributions from randomly moving scatterers, we model cell noise similar to the representation of the action potential signal as the outer product of a spatial pattern vector and a temporal amplitude vector. Each particle contributes a unique random spatial pattern, $\boldsymbol{p}_i$, and a temporal amplitude, $\boldsymbol{a}_i$. It is assumed that the action potential signal corresponds to the first component $\boldsymbol{a}_1$, so that the components $i > 2$ are arbitrary time series, not limited to sparse signals of discrete spikes. Consequently, the observed video F is the sum of the contributions from all patterns:

$$F = \sum_{i=1}^{N_{\mathrm{c}}} \boldsymbol{a}_i \boldsymbol{p}_i^{\intercal} = AP$$

where N_{c} represents the total number of signal components, matrix A ($N_{\mathrm{fr}} \times N_{\mathrm{c}}$) contains temporal amplitudes in its columns, and matrix P ($N_{\mathrm{c}} \times N_{\mathrm{px}}$) contains spatial patterns in its rows. The Gramian is then expressed as

$$G = (AP)(AP)^{\intercal} = APP^{\intercal}A^{\intercal}.$$

Since each pattern is independent and zero-centered, assuming $N_{\mathrm{px}} > N_{\mathrm{c}}$, the following approximation holds:

$$PP^{\intercal} \approx kI$$

where the scaling constant $k = \mathbb{E}\|\boldsymbol{p}_i\|^2 = N_{\mathrm{px}}$ represents the expected magnitude of the patterns. Thus, the Gramian matrix approximates the covariance matrix of the amplitudes (up to a constant factor):

$$G \approx N_{\mathrm{px}} AA^{\intercal} \tag{4}$$

This implies that the outcome of the ChiSCAT algorithm is essentially a principal component analysis (PCA) of the matrix A. We will refer to the principal components as PCi in the further text. It is safe to assume that motion of every particle in the cell is independent, which implies that the amplitude vectors $\boldsymbol{a}_i$ are approximately orthogonal. It is further assumed that the total variance of the noise is known (since it can be measured experimentally):

$$\sigma_{\text{tot}}^2 = \sum_{i=2}^{i=N_c} \sigma_i^2$$

where σ_i^2 represents the variance of $\boldsymbol{a}_i$.

Recovery criterion Let us firstly focus on the case of $N_c = 2$, i.e., to have just one noise component. In this case the problem becomes relatively straightforward. The matrix $A = [\boldsymbol{a}_1, \boldsymbol{a}_2]$ is composed of the AP signal $\boldsymbol{a}_1$ and a noise vector $\boldsymbol{a}_2$. To faithfully recover the signal, the signal has to define the direction of the first eigenvector, i.e. the direction of the largest variance. The recovery criterion thus reads

$$\text{var}(\boldsymbol{a}_1) > \text{var}(\boldsymbol{a}_2) = \sigma_{\text{tot}}^2$$

$\text{var}(\boldsymbol{a}_2)$, meant to be the temporal variance of the components of $\boldsymbol{a}_2$ thus defines a limit of detection, which can be larger than the photon shot noise. It is important to note that this criterion is putting a condition on the variance of $\boldsymbol{a}_1$, not on the peak-to-peak amplitude a_{pp}. Since $\boldsymbol{a}_1$ is a sparse signal of N_{ap} unit peaks in an otherwise zero vector, $\sqrt{\text{var}(\boldsymbol{a}_1)} = \sqrt{\frac{N_{\text{ap}}}{N_{\text{fr}}}} a_{\text{pp}}$, and the criterion for successful signal recovery becomes:

$$\sigma_{\text{tot}} < \sqrt{\frac{N_{\text{ap}}}{N_{\text{fr}}}} a_{\text{pp}}.$$

Here a_{pp} is peak-to-peak amplitude of AP signal. Note that we still assume this to be one, so that σ_i denotes the strength of cell noise relative to an action potential.

In a realistic scenario where $N_{\text{ap}} = 10$ and $N_{\text{fr}} = 1000$, this implies that amplitude of AP signal must even be 10 times higher than the cell noise to recover the signal.

When σ_{tot} is distributed among multiple components ($N_c > 2$), a higher total amount of σ_{tot} can be tolerated, if the noise is spread sufficiently evenly across all modes of motion. Still, the signal has to be the largest eigenvector for recovery, and the recovery criterion becomes:

$$\max(\sigma_i) < \sqrt{\frac{N_{\text{ap}}}{N_{\text{fr}}}} a_{\text{pp}}.$$

Additional insights can be obtained from a geometrical intuition. The high-dimensional noise can be seen seen as a "blob" in high-dimensional space, where total variance is a sum of variances along every dimension, while the first principal component is the longest axis of that "blob". Both coincide when $N_c = 2$, but the variance of largest noise direction is getting smaller as number of dimensions increases and the total noise σ_{tot} is distributed among them (as a consequence of the triangle inequality). It is difficult to determine the exact lower bound for the largest noise variance, but if variance is distributed highly unevenly evenly among components, it will be on the order of t he largest component variance, resulting in the recovery criterion above.

4. Beyond the dominant eigenvector: ideas for an improved algorithm

Does the signal have to be the largest eigenvector to be recovered? Interestingly, this might not be strictly required, as can be seen in the case $N_c = 2$.

Here, even if the noise vector has greater variance and thus makes up the first principal component (PC1), the orthogonality of the signal and noise ensures that the second principal component (PC2) will capture the remaining variability, thus perfectly reconstructing the signal. This principle is illustrated in Fig. 4. More precisely, the signal can be completely restored when its variance is different from the variance of other components, a principle known as eigengap. A

significant eigengap, such as when all noise components are substantially larger than the signal, allows the removal of noise by subtracting $N_c - 1$ principal components, leading to a perfect restoration of the signal. If shot noise is taken into account, the signal will be corrupted by it. In this case, however, the problem is basically reduced to the one described in the previous section, as all of the cell noise components can be perfectly subtracted.

In practical scenarios involving cells containing numerous scatterers of varying sizes and motion amplitudes, some scatterers have the same variance as the signal, making the recovery much more difficult. Thus, it can be concluded that effective signal detection using a PCA-like approach requires opening the eigengap, i.e. ensuring that cell noise components have significantly different amplitude that AP signal. Counterintuitively, one of the ways to do it is to artificially increase the cell noise components to have variance above the signal variance.

5. Outlook of other potential approaches

So far it has been demonstrated that while PCA-like approaches are highly effective when only shot noise is present (or, more generally, in presence of i.i.d. uncorrelated noise), their performance deteriorates for when cell noise is present. Other approaches can potentially be more beneficial under assumption of cell noise dominance. Below we summarize the most promising approaches, detailed analysis of which are beyond the scope of this article.

Independent component analysis (ICA) ICA is looking for a projection of high-dimensional signals which would maximize non-Gaussianity of the recovered signals. There are physics-motivated reasons to assume that the only highly non-Gaussian component of signal is action potential, since all other noises should have approximately Gaussian distribution. Moreover, it should be possible to use variation of ICA which maximizes skewness as a metric of non-Gaussianity instead of usually used kurtosis or negentropy [20]. This version of algorithm [21] is expected to better reflect the nature of the signal, since AP is highly non-symmetric. Another property of the signal which can be exploited is it's sparsity, suggesting usage of ICA variations that specifically optimize for sparsity [22].

Computer vision algorithms In contrast to ChiSCAT, which compromises visual interpretability for enhanced spatial resolution, iSCAT provides visually interpretable images. It was observed during experiments that, sometimes, a naked eye can recognize a fringe-like pattern caused by light reflecting off an entire cell. Just as the classical iSCAT algorithm [23] can track individual particles, it should be feasible to track fringes from the cell outer membrane, thereby selecting the action potential (AP) signal using prior knowledge of the spatial patterns associated with it. This tracking can be accomplished using classical computer vision techniques such as the Hough transform [24] and wavelet transform [25], or by employing modern deep learning methods that are capable of both detecting fringe patterns [26] and reconstructing full wavefronts (unwrapping) [27]. Ultimately, a full refractive index tomography could be performed, so that individual objects in a cell could be tracked.

6. Conclusion

This article provides a theoretical analysis of the criteria for AP detection together with experimental findings about noise properties of different laser sources. We found that use of low-coherence illumination strongly reduces vibrational noise and that a well-optimized setup can indeed operate close to the fundamental photon shot noise limit. However, our theoretical investigation also highlights that the noise from cellular motions is a much more significant challenge for AP detection than shot noise. Theoretical analysis suggests that detection of AP with ChiSCAT can be achieved by opening the eigengap, i.e. modifying the amplitude of the noise

to make it significantly different to the amplitude of the signal, which could define a direction for future work. Alternative strategies, such as ICA and advanced computer vision techniques, also have potential to overcome the limitations associated with cellular noise. These methods, which exploit non-Gaussianity and sparseness of action potentials, or *apriori* information about spatial fringe patterns associated with the cell, may allow reliable AP detection. Future research is needed to explore their integration into ChiSCAT and related interferometric microscopy techniques and experimentally evaluate their performance. If successful, label-free and non-invasive AP detection in living tissues will pave the way for new insights in cellular biology and neuroscience.

References

1. D. K. Hill and R. D. Keynes, "Opacity changes in stimulated nerve," The J. Physiol. **108**, 278–281 (1949).
2. L. B. Cohen, R. D. Keynes, and B. Hille, "Light Scattering and Birefringence Changes during Nerve Activity," Nature **218**, 438–441 (1968).
3. K. Iwasa, I. Tasaki, and R. C. Gibbons, "Swelling of Nerve Fibers Associated with Action Potentials," Science **210**, 338–339 (1980). Publisher: American Association for the Advancement of Science.
4. A. La Porta, R. Stepnoski, F. Raccuia-Behling, *et al.*, "Recording action potential in cultured aplysia neurons using intrinsic optical signals," in *OSA Annual Meeting,* (Optica Publishing Group, 1990), p. MPP3.
5. R. Stepnoski, A. LaPorta, F. Raccuia-Behling, *et al.*, "Noninvasive detection of changes in membrane potential in cultured neurons by light scattering." Proc. National Acad. Sci. **88**, 9382–9386 (1991).
6. B. A. MacVicar and D. Hochman, "Imaging of synaptically evoked intrinsic optical signals in hippocampal slices," J. Neurosci. **11**, 1458–1469 (1991).
7. G. Kim, P. Kosterin, A. Obaid, and B. Salzberg, "A mechanical spike accompanies the action potential in mammalian nerve terminals," Biophys. journal **92**, 3122–3129 (2007).
8. A. LaPorta and D. Kleinfeld, "Interferometric detection of action potentials," Cold Spring Harb. Protoc **2012**, 307–311 (2012).
9. A. H. Badreddine, T. Jordan, and I. J. Bigio, "Real-time imaging of action potentials in nerves using changes in birefringence," Biomed. optics express **7**, 1966–1973 (2016).
10. Y. Yang, X.-W. Liu, H. Wang, *et al.*, "Imaging action potential in single mammalian neurons by tracking the accompanying sub-nanometer mechanical motion," ACS nano **12**, 4186–4193 (2018).
11. T. Ling, K. C. Boyle, G. Goetz, *et al.*, "Full-field interferometric imaging of propagating action potentials," Light. Sci. & Appl. **7**, 107 (2018).
12. T. Ling, K. C. Boyle, V. Zuckerman, *et al.*, "High-speed interferometric imaging reveals dynamics of neuronal deformation during the action potential," Proc. National Acad. Sci. **117**, 10278–10285 (2020).
13. J. K. Mueller and W. J. Tyler, "A quantitative overview of biophysical forces impinging on neural function," Phys. biology **11**, 051001 (2014).
14. J. Mosbacher, M. Langer, J. Hörber, and F. Sachs, "Voltage-dependent membrane displacements measured by atomic force microscopy," The J. general physiology **111**, 65–74 (1998).
15. A. González-Pérez, L. D. Mosgaard, R. Budvytyte, *et al.*, "Solitary electromechanical pulses in lobster neurons," Biophys. chemistry **216**, 51–59 (2016).
16. A. Trelin, S. Kussauer, P. Weinbrenner, *et al.*, "Chiscat: Unsupervised learning of recurrent cellular micromotion patterns from a chaotic speckle pattern," Nano Lett. (2024).
17. P. Kukura, H. Ewers, C. Müller, *et al.*, "High-speed nanoscopic tracking of the position and orientation of a single virus," Nat. methods **6**, 923–927 (2009).
18. A. Perry, A. S. Wein, A. S. Bandeira, and A. Moitra, "Optimality and sub-optimality of pca i: Spiked random matrix models," The Ann. Stat. **46**, 2416–2451 (2018).
19. C. Ghez, "The Cerebellum," Princ. Neural Sci. pp. 626–646 (1991).
20. A. Hyvärinen and E. Oja, "Independent component analysis: algorithms and applications," Neural networks **13**, 411–430 (2000).
21. L. Song and H. Lu, "Ecoica: Skewness-based ica via eigenvectors of cumulant operator," in *Asian Conference on Machine Learning,* (PMLR, 2016), pp. 445–460.
22. A. Chichocki, Y. Li, P. Georgiev, and S.-i. Amari, "Beyond ica: Robust sparse signal representations," in *2004 IEEE International Symposium on Circuits and Systems (ISCAS),* vol. 5 (IEEE, 2004), pp. V–V.
23. J.-S. Park, I.-B. Lee, H.-M. Moon, *et al.*, "Label-free and live cell imaging by interferometric scattering microscopy," Chem. Sci. **9**, 2690–2697 (2018).
24. V. A. Shapiro, "On the hough transform of multi-level pictures," Pattern Recognit. **29**, 589–602 (1996).
25. Z. Wang, J. Ma, and M. Vo, "Recent progress in two-dimensional continuous wavelet transform technique for fringe pattern analysis," Opt. Lasers Eng. **50**, 1052–1058 (2012).
26. A. Reyes-Figueroa, V. H. Flores, and M. Rivera, "Deep neural network for fringe pattern filtering and normalization," Appl. Opt. **60**, 2022–2036 (2021).
27. S. Feng, Q. Chen, G. Gu, *et al.*, "Fringe pattern analysis using deep learning," Adv. photonics **1**, 025001–025001 (2019).

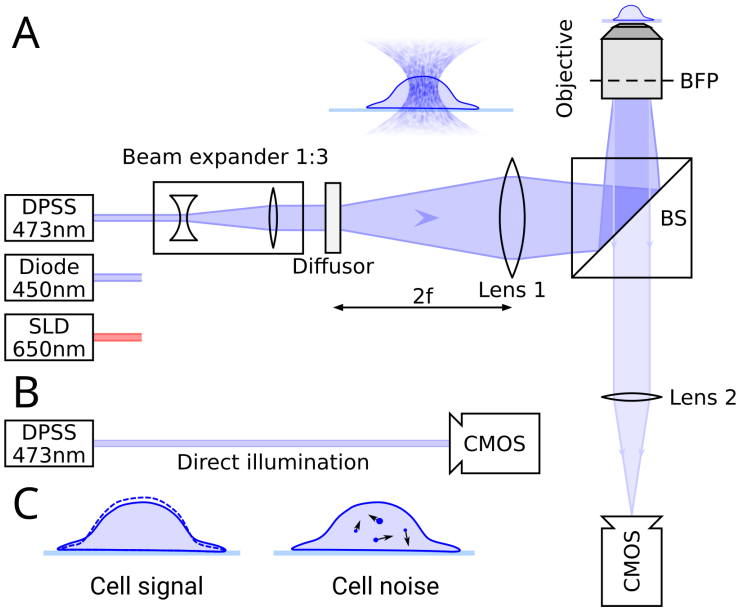


Fig. 1. (a) Interferometric cell imaging setup (ChiSCAT). The beam from one of the sources (DPSS laser at 473 nm, diode laser at 450 nm, or SLD at 650 nm) is expanded and passed through a holographic diffuser to create a random light field in the cell plane. The speckle pattern reflected from the cell and the coverslide interferes to generate the video recorded with a high-speed CMOS camera. (b) To measure inherent laser and camera noise laser was set to illuminate camera directly (Direct illumination). (c) The ultimate goal of this paper is to find criteria at which the cell signal can be reliable disentangled from the cell noise.

<

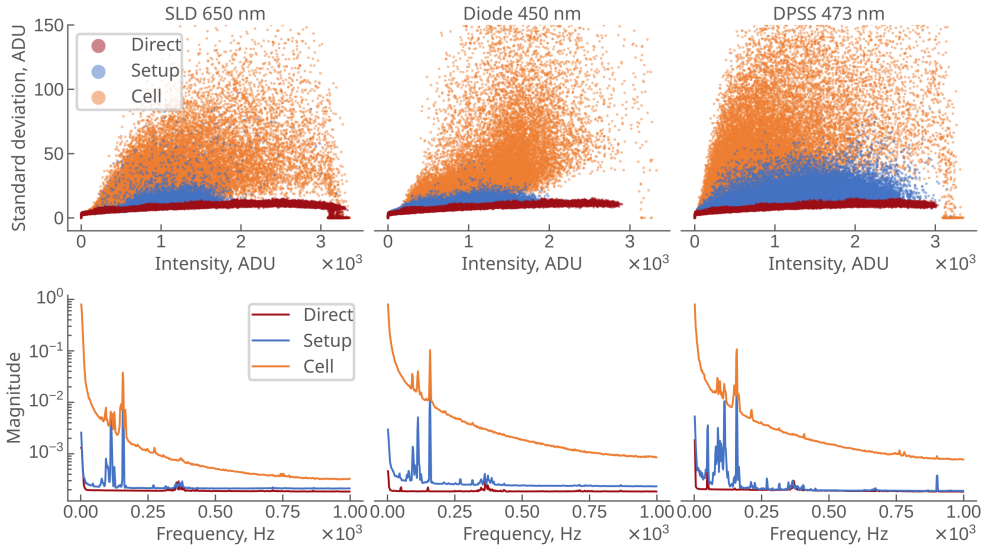


Fig. 2. Results of laser and cell noise characterization. Top row: dependence of the pixel standard deviation on intensity for every pixel of the camera sensor for different kinds of illumination and different versions of experiment. Bottom row: average Fourier transformed time traces from every pixel for different versions of the experiment and kind of illumination. ADU: analog-to-digital units.

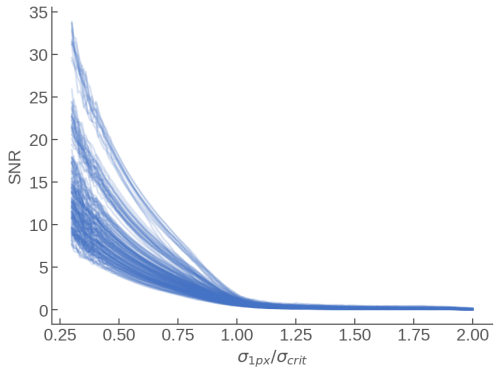


Fig. 3. Numerically simulated SNR of recovered signal at different values of $\sigma_{1\mathrm{px}}/\sigma_{\mathrm{crit}}$

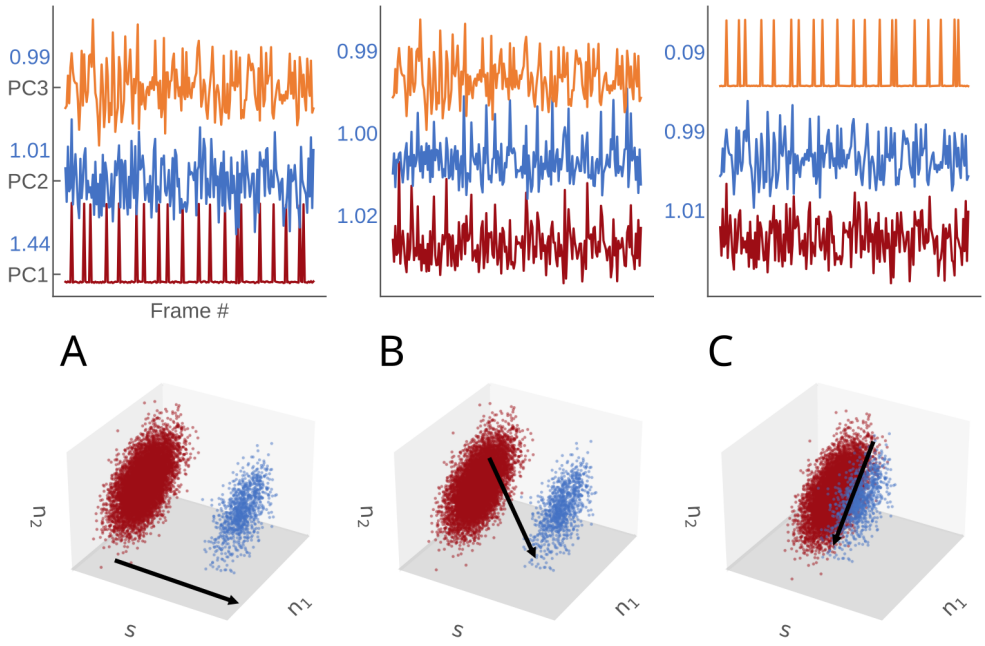


Fig. 4. Numerical simulation for $N_c = 3$, demonstrating signal scale variation. (a) strong signal ($\mathrm{var}(\boldsymbol{a}_1) > \mathrm{var}(\boldsymbol{a}_{2,3})$); (b) moderate signal ($\mathrm{var}(\boldsymbol{a}_1) \approx \mathrm{var}(\boldsymbol{a}_{2,3})$); (c) weak signal ($\mathrm{var}(\boldsymbol{a}_1) < \mathrm{var}(\boldsymbol{a}_{2,3})$). The upper row shows the reconstructed principal components, with explained variance for each PC indicated in blue text. The lower row displays amplitudes of the signal ($\boldsymbol{s} = \boldsymbol{a}_1$) and noise ($\boldsymbol{n}_1 = \boldsymbol{a}_2$, $\boldsymbol{n}_2 = \boldsymbol{a}_3$) as a 3D scatter plot, where each dot represents a frame (i.e. an entry of $\boldsymbol{a}_i$).
The black arrow indicates the alignment of the first principal component (PC1). When the signal variance exceeds the noise variance (a), PC1 aligns with the $\boldsymbol{s}$ axis, allowing for perfect signal reconstruction as PC1. When the signal and noise variances are similar (b), PC1 aligns diagonally, distributing the signal across multiple principal components. When the signal variance is much lower (c), PC1 lies within the $\boldsymbol{n}_1$-$\boldsymbol{n}_2$ plane, restoring the signal as PC3. Data points are color-coded based on AP presence for better visualization.

5.3 Three-dimensional magnetic resonance tomography with sub-10 nanometer resolution

Authored by Mohammad T. Amawi, **Andrii Trelin**, You Huang, Paul Weinbrenner, Francesco Poggiali, Joachim Leibold, Martin Schalk, and Friedemann Reinhard
Journal: npj Quantum Information 10, no. 1 (2024): 16.
Published: 25.12.2024
DOI: 10.1038/s41534-024-00809-w
Reference: [170]

npj | quantum information

www.nature.com/npjqi

ARTICLE OPEN

Check for updates

Three-dimensional magnetic resonance tomography with sub-10 nanometer resolution

Mohammad T. Amawi[1,2,3,4], Andrii Trelin[1,3], You Huang[1,3,5,6], Paul Weinbrenner[1,3], Francesco Poggiali[1,3,4], Joachim Leibold[2,4], Martin Schalk[2,4] and Friedemann Reinhard[1,3,4]✉

We demonstrate three-dimensional magnetic resonance tomography with a resolution down to 5.9 ± 0.1 nm. Our measurements use lithographically fabricated microwires as a source of three-dimensional magnetic field gradients, which we use to image NV centers in a densely doped diamond by Fourier-accelerated magnetic resonance tomography. We also demonstrate a compressed sensing scheme, which allows for direct visual interpretation without numerical optimization and implements an effective zoom into a spatially localized volume of interest, such as a localized cluster of NV centers. It is based on aliasing induced by equidistant undersampling of k-space. The resolution achieved in our work is comparable to the best existing schemes of super-resolution microscopy and approaches the positioning accuracy of site-directed spin labeling, paving the way to three-dimensional structure analysis by magnetic-gradient based tomography.

npj Quantum Information (2024)10:16 ; https://doi.org/10.1038/s41534-024-00809-w

INTRODUCTION

In recent years, various nano-sensors, most prominently magnetic resonance force microscopy (MRFM) and nitrogen-vacancy (NV) centers, have enabled the detection of small ensembles of electron[1,2] and nuclear[3–5] spins, partially down to the level of single spins. Translating this power from a mere detection to a three-dimensional imaging technique promises transformative applications. Three-dimensional imaging of color centers would enable selective addressing and readout of networks of coherently coupled color centers in densely doped samples[6,7], or the detection of elementary particles by high-resolution mapping of the crystal strain they induce upon impact[8]. Applied to electron spins, it would enable three-dimensional imaging of spin-labeled proteins. Such a technique would in particular provide distance constraints for label distances of >80 Å and for proteins labeled with arbitrary many electron spins, filling two blind spots of present electron spin resonance spectroscopy. Applied to nuclear spins, it would provide an ultimate microscope, able to image within opaque samples with label-free chemical contrast.

Conceptually, the step from detection to imaging is straightforward. Applying a magnetic field gradient is all it takes to turn a magnetic resonance spectrum into a one-dimensional image. Multiple gradients along linearly independent directions can encode multi-dimensional images, most beautifully illustrated in the output of clinical magnetic resonance imaging scanners. If the gradients can be switched faster than the duration of the spectroscopy sequence, Fourier-accelerated techniques can acquire extended volumes in reasonable time[9]. In clinical scanners, these comprise thousands of voxels, and similar data volumes are expected for particle detectors or imaging of a densely spin-labeled protein. Yet, three-dimensional Fourier-accelerated imaging at the nanoscale has remained elusive.

Imaging by less scalable techniques has been demonstrated multiple times. Three-dimensional imaging of nuclear spins with atomic resolution has been achieved using the intrinsic field gradient emerging from the magnetic dipole field of a color center[10,11]. However, only the closest few nanometers around a defect can be imaged by this approach so that it is limited to intrinsic spins in the diamond so far. One-dimensional and two-dimensional[12] imaging in static gradients has been demonstrated, including resolving two adjacent centers by the gradient field of a hard-drive write head[13]. Three-dimensional images of intrinsic electron spins in a diamond have been obtained using a static gradient positioned by a scanning probe[14]. Fourier acceleration has remained out of reach of these approaches where gradients cannot be switched within a spectroscopy sequence.

Fourier acceleration of imaging has been demonstrated[7,9] using quickly switchable conductors as gradient sources, but experiments with nanoscale resolution have remained limited to one- and two-dimensional proofs of the concept. One-dimensional imaging in MRFM by current-driven gradients has very recently even achieved sub-Ångstrom resolution[15].

RESULTS AND DISCUSSION

Device

Here we demonstrate Fourier-accelerated three-dimensional imaging with nanometer-scale resolution. The key is a device to produce three linearly independent magnetic field gradients from a two-dimensional layout of conductors (Fig. 1a). Three microfabricated wires, arranged in a U-shape structure, create linearly independent gradient fields in a plane few microns beneath the structure, of around $|\nabla(\mathbf{B}\cdot\mathbf{e}_{111})| \approx 2\ \mathrm{G\mu m^{-1}} = 2\cdot 10^2\ \mathrm{Tm^{-1}}$. This device is fabricated via lift-off photolithography on a diamond substrate hosting a densely doped ensemble of NV centers (Element Six General Grade CVD diamond, $[NV] \approx 0.13$ ppb, Fig. 1a). "Densely" here is to be understood in the sense that NV centers sit closer together than the diffraction limit. The U-microstructure consists of a 200 nm gold film on top of a

[1]Institute of Physics, University of Rostock, Rostock, Germany. [2]Walter Schottky Institut and Physik-Department, Technical University of Munich, Munich, Germany. [3]Department of Life, Light and Matter, University of Rostock, Rostock, Germany. [4]Munich Center for Quantum Science and Technology (MCQST), Munich, Germany. [5]CAS Key Laboratory of Microscale Magnetic Resonance and School of Physical Sciences, University of Science and Technology of China, Hefei 230026, China. [6]CAS Center for Excellence in Quantum Information and Quantum Physics, University of Science and Technology of China, Hefei 230026, China. ✉email: friedemann.reinhard@uni-rostock.de

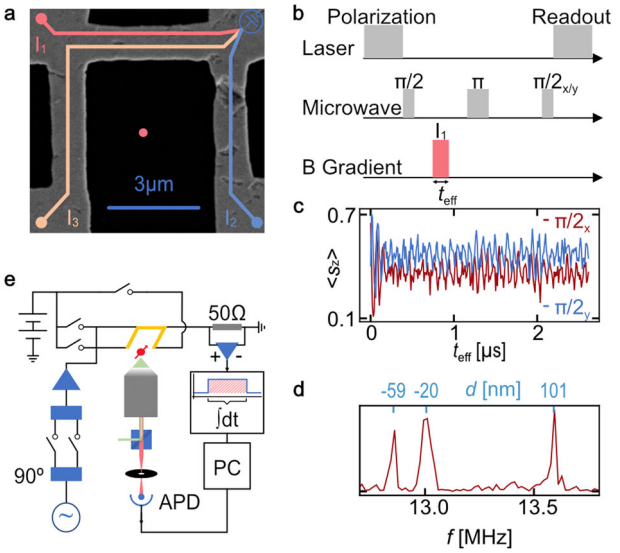


Fig. 1 Experimental setup and one-dimensional magnetic resonance tomography of NV centers. a Electron micrograph of a device as used in the present study. Currents in the three gold wires of a microfabricated U-Structure create three linearly independent magnetic field gradients in the densely doped diamond below the structure. **b** Pulse sequence for one-dimensional imaging. A magnetic gradient pulse (length t_{eff}) inserted into a Hahn echo sequence phase-encodes position. The NV spin state is initialized and the spin projection $\langle \hat{S}_z \rangle$ is read out optically. **c** Measurement result of (**b**). $\pi/2_x$ and $\pi/2_y$ denote the phase of the trailing $\pi/2$ pulse in (**b**). **d** Fourier transform of a dataset like (**c**) extending to $t = 60$ μs. Every NV center gives rise to one peak at the Larmor frequency set by the magnetic field $B_{l_1}(d)$ of the wire. d denotes the distance from the centroid of the NV center's cluster (**e**) Experimental setup. A single microwave generator, a 90° splitter and two microwave switches are used to implement the Hahn Echo sequence. A confocal microscope with an avalanche photodiode (APD) as a detector is used for NV center polarization and readout. The gradient currents I_1, I_2, I_3 are created from a constant voltage source and can be pulsed by a fast switch (ic-Haus HGP), which has a current rising and falling time of 1 ns. The voltage drop across the resistor is recorded by an A/D-converter and the pulse integral $\int Idt$ is saved for every single current pulse.

10 nm thick chromium layer. Each of its three arms is 5 μm long and 500 nm wide. The top arm also serves as a microwave antenna to implement single-qubit gates. We generate switchable magnetic field gradients by sending currents, labeled I_1, I_2, and I_3 in Fig. 1a, into the three arms of the U microstructure. All currents are terminated with a 50 Ω resistance at the same vertex of the U structure. In all measurements a homogeneous bias magnetic field of $B_0 \approx 76$ G is applied along one of the four NV axes. This device is used to implement gradient echo pulse sequences, like the one-dimensional example shown in Fig. 1b–d. A Hahn echo sequences decouples the NV centers from static and slowly fluctuating background fields, to enable T_2-limited sensing. A magnetic field gradient pulse, created by the current I_1, is applied during one half of the echo sequence. This phase-encodes the position, because an NV center at point $\mathbf{x}$ acquires a position-dependent phase shift

$$\phi(\mathbf{x}, t) = \int_0^t \omega(\mathbf{B}_I(\mathbf{x}, \tau))d\tau \approx \omega(\mathbf{B}_I(\mathbf{x}))t \tag{1}$$

where $\omega(\mathbf{B}_I(\mathbf{x}, \tau))$ denotes the shift in the Larmor frequency induced by the current I and the approximation holds for pulses close to a rectangular shape. At the end of the Hahn echo sequence, this phase shift translates into an oscillatory spin signal

$$\langle \hat{S}_z \rangle(t) = \begin{cases} (1 + \cos(\omega(\mathbf{x})t))/2 & \text{trailing } \pi_x/2 \text{ pulse} \\ (1 + \sin(\omega(\mathbf{x})t))/2 & \text{trailing } \pi_y/2 \text{ pulse} \end{cases} \tag{2}$$

For a distribution of N NV centers, the oscillatory signals of all centers will linearly superpose to a characteristic beating pattern

$$\langle \hat{S}_z \rangle(t) = \sum_{\mathbf{x}_{\mathrm{NV}}} (1 + \cos(\omega(\mathbf{x}_{\mathrm{NV}})t))/2N \tag{3}$$

(assuming a trailing $\pi_x/2$ pulse). The various $\omega(\mathbf{x}_{\mathrm{NV}})$ can be recovered from this signal by an inverse Fourier transform, creating a one-dimensional image of the NV centers Fig. 1d. In the terminology of magnetic resonance imaging, the time domain of our experiment is k-space, whereas the frequency domain is real space.

One major challenge of this experiment consists in creating sufficiently rectangular pulses to satisfy the approximation of Eq. (1). This requires a stable current supply that moreover has to be controlled with a fast (100 MHz) bandwidth to ensure that the rising and falling edges are quasi-instantaneous, i.e., much shorter than one period of the current-induced Larmor frequency $\omega(\mathbf{B}_I)$. Stability within every current pulse is required, because any variation of $\omega(\mathrm{B}_I(\mathbf{x}, \tau))$ over the pulse will introduce a chirp in the time domain signal (Fig. 1c), which will blur the image in the frequency domain (Fig. 1d). Stability between successive experimental repetitions is required, because shot-to-shot fluctuations of the magnetic field induce decoherence (see below).

We experimentally address these constraints by two means (Fig. 1e). First, the current pulses are generated by switching a stable voltage source (Keithley 2230G-30-6) using fast switches (ic-Haus HGP), ensuring high stability of the pulse height and a nearly rectangular pulse shape. Second, we correct for residual nonlinearities and fluctuations by measurement and online post-processing. We acquire the current integral $\int_0^t I(\tau)d\tau$ for every pulse of every experimental repetition by hardware-integration on a fast A/D converter (Spectrum M4i.4451-x8), and use this value to define a new time axis for all photonic measurements that removes chirps. Specifically, we make the following approximation (valid for nearly rectangular pulses and a nearly linear Zeeman shift)

$$\int_0^t \omega(\mathbf{B}_I(\mathbf{x}, \tau))d\tau \approx \omega_{\mathrm{I,ref}} \frac{\int_0^t I(\tau)d\tau}{I_0} = \omega_{\mathrm{I,ref}} t_{\mathrm{eff}} \tag{4}$$

Here, $\omega_{\mathrm{I,ref}}(\mathbf{x})$ is the shift in Larmor frequency induced by some reference current I_0 and t_{eff} denotes an "effective pulse duration". We thus absorb minor fluctuations of the current over the pulse into this redefined time coordinate t_{eff}. All time-domain plots in this paper will use t_{eff} as time axis unless noted otherwise. This correction also suppresses shot-to-shot fluctuations, improving coherence[16].

Three dimensional imaging

We now extend this one-dimensional magnetic resonance tomography to three dimensions, employing the three magnetic field gradients provided by the currents I_1, I_2, I_3 of our device. Note that these gradients are linearly independent if the focal spot of the microscope is placed a few micrometers below the plane of the U-structure. This linear independence enables three-dimensional imaging despite the fact that the wire layout is two-dimensional. All following experiments have been performed in the lateral center of the U-structure, and ≈ 6 μm beneath the diamond surface.

During the Hahn Echo sequence the pulses of these three currents are applied consecutively (see Fig. 2a). Since the accumulated phase will add up linearly, the resulting spin signal is given by:

$$\langle \hat{S}_z \rangle(t) = \sum_{\mathbf{x}_{\mathrm{NV}}} (1 + \cos(\omega_{I_1}(\mathbf{x}_{\mathrm{NV}})t_1 + \omega_{I_2}(\mathbf{x}_{\mathrm{NV}})t_2 + \omega_{I_3}(\mathbf{x}_{\mathrm{NV}})t_3))/2N \tag{5}$$

(assuming a trailing $\pi_x/2$ pulse).

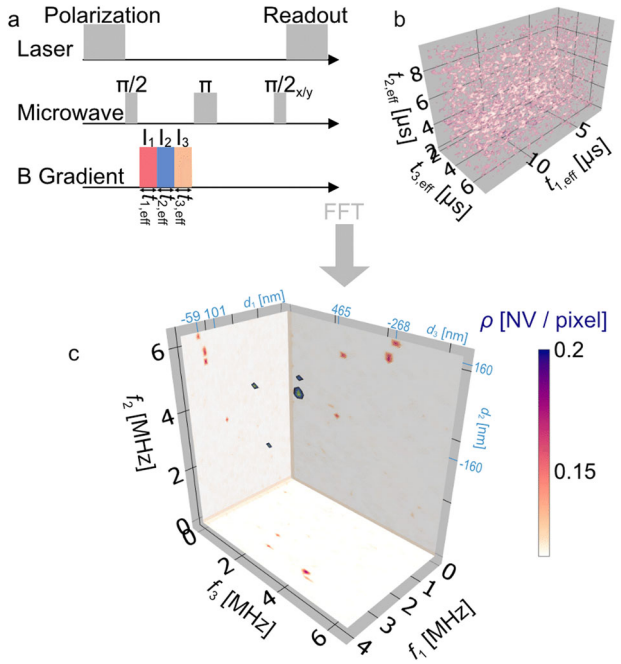


Fig. 2 Three-dimensional magnetic resonance tomography. **a** Pulse sequence. The sequence of Fig. 1 is extended to contain three magnetic gradient pulses from different wires. **b** Time domain data recorded from the sequence of (**a**) ending with $\pi/2_x$. **c** Three-dimensional Fourier transform of the data in (**b**). The plot shows the square of the absolute value (spectral power) of the Fourier transform. d_1, d_2, d_3 denote the distance to the respective wire (see Supplementary Discussion 3). The bottom, left, and back faces show projections of the 3D data.

In analogy to one-dimensional tomography the set of $(\omega_{I_1}(\mathbf{x}_{NV}), \omega_{I_2}(\mathbf{x}_{NV}), \omega_{I_3}(\mathbf{x}_{NV}))$ can be recovered from the three-dimensional time domain data (Fig. 2b) by a 3D inverse Fourier transform, forming a three-dimensional image. We note that this resulting image is distorted because the gradients, while linearly independent, are not fully orthogonal. While this distortion can in principle be corrected by computing and inverting the exact spatial distribution of the frequency shift $\omega_I(\mathbf{x})$, the raw result of the Fourier transform is still a true three-dimensional image. This resulting image reveals individual NV centers in the diamond. Note that only NV centers within the confocal volume of the microscope contribute to the optically detected spin signal and can therefore be imaged. For the given NV density 5−15 centers are expected to be seen.

Sparse sampling

One challenge of such multidimensional measurements is the large number of required data points in Fourier space, e.g., 10^6 points in Fig. 2, which places strong demands on memory and sequencing hardware. This number can be reduced by compressed sensing, where only a subset of points is acquired, and the image is reconstructed by numerical techniques like L_1 minimization, exploiting the a priori knowledge that the signal is a sparse set of discrete points[9]. Interestingly, our experimental setting allows for another compressed sensing approach. It does not require elaborate numerical reconstruction and exploits a different kind of a priori knowledge: that the signal is restricted to a narrow region of interest, i.e., a narrow band in frequency space. In this special case, we can implement an effective "zoom" into this region of interest by undersampling the signal in the time domain, lowering the amount of data points. Undersampling leads to aliasing of the signal in frequency space. For suitable parameters, this will shift the signal frequency band to a contiguous low frequency window where it can still be recovered by the inverse Fourier transform, effectively implementing a zoom. While this idea has already been explored in macroscale magnetic resonance[17], introducing it to nanoscale magnetic resonance addresses two outstanding issues in this field. First, analog techniques for band-pass filtering like heterodyne detection cannot be used at the nanoscale, because the signal here is inherently digital, measuring e.g., the spin state of an NV center detector at one specific moment in time rather than a continuous electric voltage proportional to nuclear magnetization. Second, the sample volume (e.g., a single protein) is frequently much smaller than the volume spanned by the gradient conductors, so the acquisition of the full volume would require excessive resources. We demonstrate a proof of concept of this idea in Fig. 3. The simulated one-dimensional time and frequency domain plots (left part Fig. 3a) display a limited frequency band. When the time-domain signal is undersampled, i.e., sampled at a rate that the Nyquist frequency f_{Nyq} is smaller than the highest signal frequency, any signal at $f > f_{Nyq}$ will be aliased to a frequency

$$f_{obs} = |f - 2N \cdot f_{Nyq}|, \tag{6}$$

where N is the integer minimizing $|f - 2Nf_{Nyq}|$. In (Fig. 3a, middle plot), the signal band (around $f \approx 30$ MHz) is close to twice the Nyquist frequency ($2 \cdot f_{Nyq} = 35$ MHz) and hence aliased to a region close to $f = 0$ MHz. Note that the aliasing involves mirroring of the signal band, because the signal is at a lower frequency than the closest even multiple of f_{Nyq}.

We show this concept by acquiring three separate two-dimensional measurements (Fig. 3b−g), which display NV centers in a limited region of interest (upper right corner in Fig. 3b, c), defined by the confocal volume of the microscope. This process of undersampling and aliasing implements a zoom into the region of interest (Fig. 3d, e). Note that this process requires the signal to be confined to a limited window of frequencies. Since frequencies equal up to an integer multiple of $2f_{Nyq}$ will appear at the same f_{obs} (Eq. 6), signals outside the zoom window will fold back into the signal of interest. To prevent contamination of the resulting image, the signal should be bandpass limited, i.e., values outside the frequency range of the signal should be zero and the Nyquist frequency should not fall below the bandwidth of the NV signal spectrum. For a suitable parameter choice of the undersampling, a zoom can be achieved that exactly covers the region of interest (Fig. 3f, g), allowing for the acquisition of a full image with a greatly reduced number of data points. In the specific example (Fig. 3f, g), the two dimensions are undersampled by a factor of 6 and 3, reducing the number of data points by a factor of 18, i.e., more than an order of magnitude. Note that reconstruction and visualization are still feasible by an inverse Fourier transform (Fig. 3f). L_1 minimization is not required for reconstruction, but can still be implemented to improve the quality of the image and/or further reduce the number of data points required (Fig. 3c, e, g). We finally note a constraint of the technique. The undersampled data points have to be placed equidistantly in time, since any jitter or chirp will lead to a spectral broadening in the frequency-space image. Since a variation of the gradient current over the duration of a pulse is indistinguishable from a variation in timing, this also places higher demands on the constancy of currents, i.e., the requirement of rectangular current pulses discussed above.

Spatial resolution

We finally analyze the spatial resolution that is achieved in our measurement. This is defined by the magnitude of the magnetic field gradient, and the spectral resolution of the spectroscopy. The frequency resolution of Fourier-transformed data is given as the inverse of the length of the time domain signal. Analogous to that, the frequency (and thus spatial) resolution of our magnetic

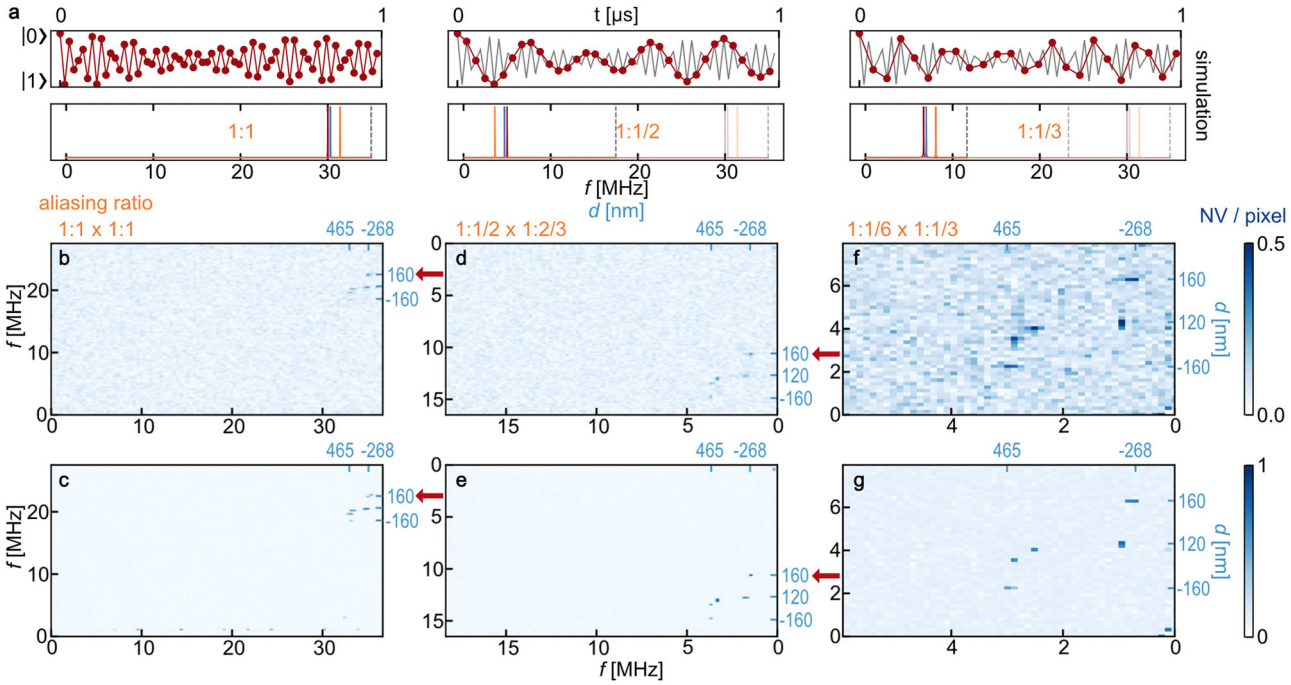


Fig. 3 Aliasing magnification and speed-up of Fourier magnetic imaging. The plots in (**a**) show a simulated signal consisting of three distinct frequency components at (19.0, 20.3, 21.4) MHz, and its Fourier transform. Going through the columns from left to right the sampling rate is reduced resulting in a slower oscillation (red trace) and a lower Nyquist frequency (black-dashed line). Aliasing around the closest even multiple of the undersampled Nyquist frequency shifts the signal to a window close to $f = 0$, but does not change its shape. The Nyquist frequency of the undersampled signal has to be chosen large enough to cover the entire signal bandwidth. The signal is shifted to negative frequencies, and hence appears flipped in a frequency axis using $|f|$, if it sits on the left of the closest even multiple of the Nyquist frequency. Panels (**b**–**g**) display measured 2D images of NV centers acquired by taking the FFT of the time domain signal (**b**, **d**, **f**) or by doing an L1 minimization of the time domain signal (**c**, **e**, **g**, see Supplementary Discussion 5 for details). (**b**, **c**) The Nyquist frequencies for each gradient direction (x and y axes) were set to be larger than the highest frequency in that direction (no aliasing). For (**d**, **e**) and (**f**, **g**) the measurement was done using an aliased grid, the aliased factor for each direction can be read in orange above FFT panel of each measurement. In (**d**, **e**) the undersampling parameters are such that the signal is flipped in both axes. For (**f**, **g**) the signal is flipped in the horizontal axis, but remains unflipped in the vertical axis. The aliased measurement (**f**, **g**) reduces the acquisition time by a factor of 10.

resonance tomography depends on how long we can make the gradient pulse length and still observe an oscillatory spin signal. The longest usable pulse is limited by the fact that the spin signal decays over time on a timescale of ≈ 10 μs (see e.g., Fig. 4a, b) because of shot-to-shot fluctuations of the gradient currents, which result in the decoherence of the NV centers. Denoting the timescale of this decay by $T_{2,I}$ (i.e., the coherence time in the presence of the gradient current), the frequency resolution is

$$\Delta f = \frac{\sqrt{2}}{\pi T_{2,I}} \tag{7}$$

where Δf denotes full width at half-maximum (FWHM) of the peak in frequency space. See Supplementary Discussion 7 for explanation of the $\frac{\sqrt{2}}{\pi}$ factor. We extract $T_{2,I}$ from a long 1D tomography data set, extending to several multiples of $T_{2,I}$. We calculate the Fourier transform for a short time window and "slide" this window over the whole range of the time domain signal. The resulting spectrogram (Fig. 4b) shows the evolution of the NV spectrum with increasing gradient pulse lengths. The signal from a single spin appears as a horizontal line in a specific frequency band. The decaying power of the signal with increasing time in this band defines the SNR over the measurement (see Supplementary Discussion 4). We fit the SNR curve (Fig. 4c) with a Gaussian ($e^{-t_{\mathrm{eff}}^2/2T_{2,I}^2}$) to obtain $T_{2,I}$. For the data of Fig. 4 we thus arrive at a coherence time of $T_{2,I_2} = 8.64 \pm 0.1\,\mu s$. Taking into account the field gradients (described by a Jacobian taken at the centroid of the cluster, see Supplementary Discussion 3 for details about resolution derivation), uncertainties in frequency can be translated into uncertainties in space as $\Delta\vec{x} = (5.9, 9.9, 14.7)$ nm. This resolution could be limited by several effects. First, shot-to-shot fluctuations of the current could shorten $T_{2,I}$. We try to suppress this by hardware integrating every single current pulse (see above) and applying post-processing corrections, but this process is equally limited by electronic noise at a lower level. Second, a spatial drift of the current path between successive experimental repetitions can equally lead to a decrease of $T_{2,I}$. A spatial drift could arise from heat expansion of the diamond and the conductors, but an expansion on the level of 10^{-3} would require a temperature difference of ≈1000 K which seems unlikely. A drift of the current path within the conductor, due to local heating, appears more reasonable. Intriguingly the product of $\omega_{\mathrm{NV}}T_{2,I}$, i.e., the relative stability of the gradient field, differs between the three wires. This tentatively suggests that spatial drifts of the current in the wires are the limiting factor rather than electrical fluctuations, which would be expected to be the same in all wires.

Summary

In summary, we have demonstrated Fourier-accelerated 3D imaging of single spins with nanoscale resolution. We have also presented a compressed sensing scheme, which exploits a limited field of view, rather than sparseness of the data. Our experiments demonstrate that resolution in the sub-10 nm range can be achieved by switchable magnetic field gradients, thus establishing a three-dimensional superresolution imaging method for optically readable spin qubits.

Notably, the resolution we obtain is among the best results ever achieved in superresolution imaging, It outperforms standard methods of localization microscopy (PALM, STORM), which typically

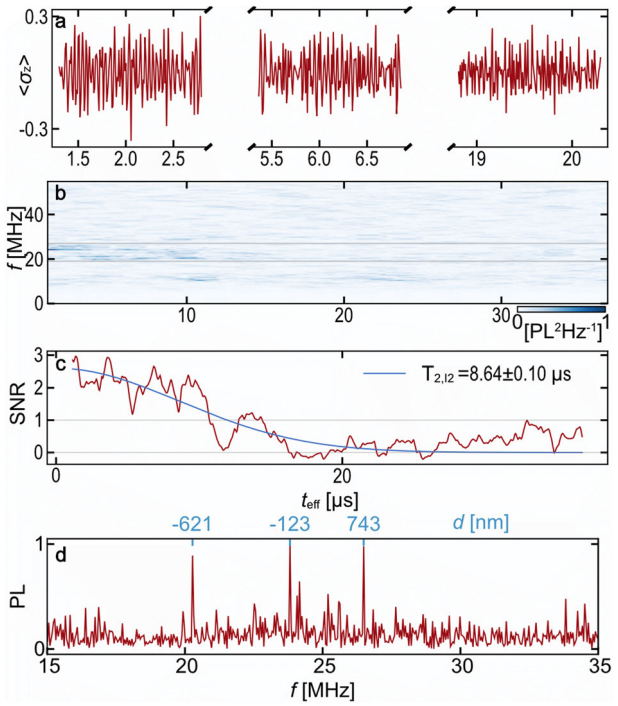


Fig. 4 Benchmarking of the spatial resolution for I_2. a time-domain signal of a one-dimensional tomography (sequence of Fig. 1b). Excerpts at different time windows are shown. **b** Spectrogram (windowed Fourier transform) of (**a**). The signal produced by the NV centers decays over a timescale of ≈10 μs. **c** Signal-to-noise ratio of (**b**), computed by integrating the power in the signal window marked in (**b**) and referencing it to the noise observed outside this window (see Supplementary Discussion 4). **c** A Gaussian fit to the data yields a decay timescale $T_{2,I_2} = 8.64 \pm 0.1\,\mu s$. **d** Fourier transform (absolute value) of the time domain signal in (**a**). Abbreviations in the figure: (*f*) frequency, (t_{eff}) length of a rectangular current pulse, (SNR) signal to noise ratio, (PL) Photoluminescence.

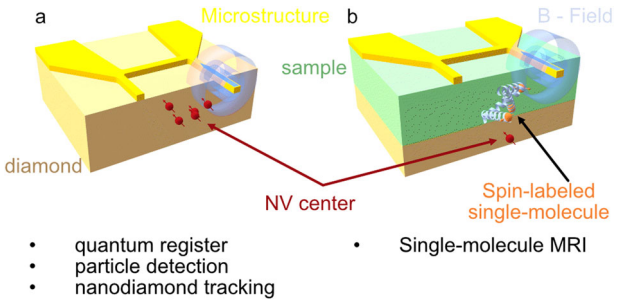


Fig. 5 Possible applications of our technique. a present device. Three-dimensional super-resolution addressing of NV centers can find use in quantum registers, particle detectors, or tracking of nano-diamonds. **b** single-molecule MRI device. Applying gradient imaging to electron spin labels could enable direct real-space imaging of spin-labeled proteins. A single nitrogen vacancy can here be used as a detector for the electron spin signal, but would not be imaged itself.

achieve ≈20 nm lateral and ≈50 nm axial resolution[18]. Only highly sophisticated techniques like MINFLUX[19] and COLD[20] have claimed even higher resolutions, but have not found widespread adoption yet and have partially been criticized for subtle pitfalls[21]. Already at the present level (Fig. 5a), our technique can find numerous applications. It can enable spin manipulation in quantum registers, e.g., by addressing a subset of coherently coupled qubits in a densely doped ensemble of NV centers. Resolving individual NV centers in a densely doped diamond also demonstrates an essential missing component for proposals to use NV centers as particle detectors[8]. Our technique could finally be applied to NV centers in nanodiamonds, e.g., to enable super-resolved tracking to measure and image forces at the nanoscale[22,23].

Moving beyond NV centers inside the diamond, the device and measurement technique could equally be applied to dark spins outside of the diamond (Fig. 5b). Here a single NV center would merely serve as a detector to enable electron/nuclear spin spectroscopy on spins, while the entire process of imaging could be performed by the device presented here. Our compressed sensing technique of "Fourier zooming" will be especially advantageous in this setting where all the spins are confined to the nanoscale detection volume of a shallow NV center. Such a direct 3D imaging technique could image an arbitrary number of spins and constrain inter-spin distances larger than 80 Å, which is not possible by current electron spin resonance spectroscopy. Shrinking the structure by one order of magnitude would even push the resolution into the range of Å. Notably the T_2 of established spin labels is sufficiently long for the spectroscopy presented here[24]. As a final vision, we express our hope that future research will identify a fluorescent molecule with an optically readable electron spin, on which the technique could then be applied without any further modification.

DATA AVAILABILITY

The data that support the findings of this study are available at https://doi.org/10.18453/rosdok_id00004504.

CODE AVAILABILITY

All codes that support the findings of this study are available from the corresponding author upon reasonable request.

Received: 25 July 2023; Accepted: 9 January 2024;
Published online: 25 January 2024

REFERENCES

1. Rugar, D., Budakian, R., Mamin, H. J. & Chui, B. W. Single spin detection by magnetic resonance force microscopy. *Nature* **430**, 329–332 (2004).
2. Shi, F. et al. Single-protein spin resonance spectroscopy under ambient conditions. *Science* **347**, 1135–1138 (2015).
3. Degen, C. L., Poggio, M., Mamin, H. J., Rettner, C. T. & Rugar, D. Nanoscale magnetic resonance imaging. *Proc. Natl. Acad. Sci. USA* **106**, 1313–1317 (2009).
4. Staudacher, T. et al. Nuclear magnetic resonance spectroscopy on a (5-Nanometer)3 sample volume. *Science* **339**, 561–563 (2013).
5. Mamin, H. J. et al. Nanoscale nuclear magnetic resonance with a nitrogen-vacancy spin ensor. *Science* **339**, 557–560 (2013).
6. Zhang, H., Arai, K., Belthangady, C., Jaskula, J. C. & Walsworth, R. L. Selective addressing of solid-state spins at the nanoscale via magnetic resonance frequency encoding. *npj Quantum Inf.* **3**, 31 (2017).
7. Artzi, Y., Zgadzai, O., Solomon, B. & Blank, A. Three-dimensional fourier imaging of thousands of individual solid-state quantum bits - a tool for spin-based quantum technology. *Phys. Scr.* **98**, 035815 (2023).
8. Rajendran, S., Zobrist, N., Sushkov, A. O., Walsworth, R. & Lukin, M. A method for directional detection of dark matter using spectroscopy of crystal defects. *Phys. Rev. D.* **96**, 035009 (2017).
9. Arai, K. et al. Fourier magnetic imaging with nanoscale resolution and compressed sensing speed-up using electronic spins in diamond. *Nat. Nanotechnol.* **10**, 859–864 (2015).
10. Zopes, J. et al. Three-dimensional localization spectroscopy of individual nuclear spins with sub-Angstrom resolution. *Nat. Commun.* **9**, 4678 (2018).
11. Abobeih, M. H. et al. Atomic-scale imaging of a 27-nuclear-spin cluster using a single-spin quantum sensor. *Nature* **576**, 411–415 (2019).
12. da Silva Barbosa, J. F. et al. Determining the position of a single spin relative to a metallic nanowire. *J. Appl. Phys.* **129**, 144301 (2021).
13. Bodenstedt, S. et al. Nanoscale spin manipulation with pulsed magnetic gradient fields from a hard disc drive writer. *Nano Lett.* **18**, 5389–5395 (2018).

14. Grinolds, M. S. et al. Subnanometre resolution in three-dimensional magnetic resonance imaging of individual dark spins. *Nat. Nanotechnol.* **9**, 279–284 (2014).
15. Haas, H. et al. Nuclear magnetic resonance diffraction with subangstrom precision. *Proc. Natl. Acad. Sci. USA* **119**, e2209213119 (2022).
16. Braunbeck, G., Kaindl, M., Waeber, A. M. & Reinhard, F. Decoherence mitigation by real-time noise acquisition. *J. Appl. Phys.* **130**, 054302 (2021).
17. Pérez, P., Santos, A. & Vaquero, J. J. Potential use of the undersampling technique in the acquisition of nuclear magnetic resonance signals. *Magn. Reson. Mater. Phys. Biol. Med.* **13**, 109–117 (2001).
18. Bond, C., Santiago-Ruiz, A. N., Tang, Q. & Lakadamyali, M. Technological advances in super-resolution microscopy to study cellular processes. *Mol. Cell* **82**, 315–332 (2022).
19. Balzarotti, F. et al. Nanometer resolution imaging and tracking of fluorescent molecules with minimal photon fluxes. *Science* **355**, 606–612 (2017).
20. Weisenburger, S. et al. Cryogenic optical localization provides 3D protein structure data with Angstrom resolution. *Nat. Methods* **14**, 141–144 (2017).
21. Prakash, K. At the molecular resolution with MINFLUX? *Phil. Trans. R. Soc. A.* **380**, 20200145 (2022).
22. Cui, Y. et al. Revealing capillarity in AFM indentation of cells by nanodiamond-based nonlocal deformation sensing. *Nano Lett.* **22**, 3889–3896 (2022).
23. Feng, X. et al. Association of nanodiamond rotation dynamics with cell activities by ranslation-rotation tracking. *Nano Lett.* **21**, 3393–3400 (2021).
24. Soetbeer, J., Hülsmann, M., Godt, A., Polyhach, Y. & Jeschke, G. Dynamical decoupling of nitroxides in o-terphenyl: a study of temperature, deuteration and concentration effects. *Phys. Chem. Chem. Phys.* **20**, 1615–1628 (2018).

ACKNOWLEDGEMENTS

This work has been supported by the Deutsche Forschungsgemeinschaft (DFG, grants RE3606/1-2, RE3606/3-1 and excellence cluster MCQST EXC-2111-390814868, SFB 1477 "Light-Matter Interactions at Interfaces" (Project No. 441234705)) and the European Union (ASTERIQS, Grant Agreement No. 820394). Y.H. acknowledges financial support from the China Scholarship Council. The authors acknowledge the help of Regina Lange and Anja Clasen with taking the SEM picture and helpful technical discussions with John Marohn.

AUTHOR CONTRIBUTIONS

M.T.A., A.T. and F.R. conceived the project. M.T.A. fabricated the device. M.T.A. and Y.H. built the setup. M.T.A., A.T., Y.H., J.L. M.S. and F.R. developed the electronics generating the gradient currents. M.T.A., A.T. and F.R. wrote the control code. M.T.A., Y.H. and P.W. performed the experiment under supervision from F.P. and F.R. M.T.A. and A.T. analyzed the data A.T. developed the field simulations and the sparse reconstruction. M.T.A., A.T., P.W. and F.R. wrote the paper. All authors read and commented on the final manuscript.

FUNDING

Open Access funding enabled and organized by Projekt DEAL.

COMPETING INTERESTS

The authors declare no competing interests.

ADDITIONAL INFORMATION

Supplementary information The online version contains supplementary material available at https://doi.org/10.1038/s41534-024-00809-w.

Correspondence and requests for materials should be addressed to Friedemann Reinhard.

Reprints and permission information is available at http://www.nature.com/reprints

Publisher's note Springer Nature remains neutral with regard to jurisdictional claims in published maps and institutional affiliations.

Open Access This article is licensed under a Creative Commons Attribution 4.0 International License, which permits use, sharing, adaptation, distribution and reproduction in any medium or format, as long as you give appropriate credit to the original author(s) and the source, provide a link to the Creative Commons license, and indicate if changes were made. The images or other third party material in this article are included in the article's Creative Commons license, unless indicated otherwise in a credit line to the material. If material is not included in the article's Creative Commons license and your intended use is not permitted by statutory regulation or exceeds the permitted use, you will need to obtain permission directly from the copyright holder. To view a copy of this license, visit http://creativecommons.org/licenses/by/4.0/.

© The Author(s) 2024

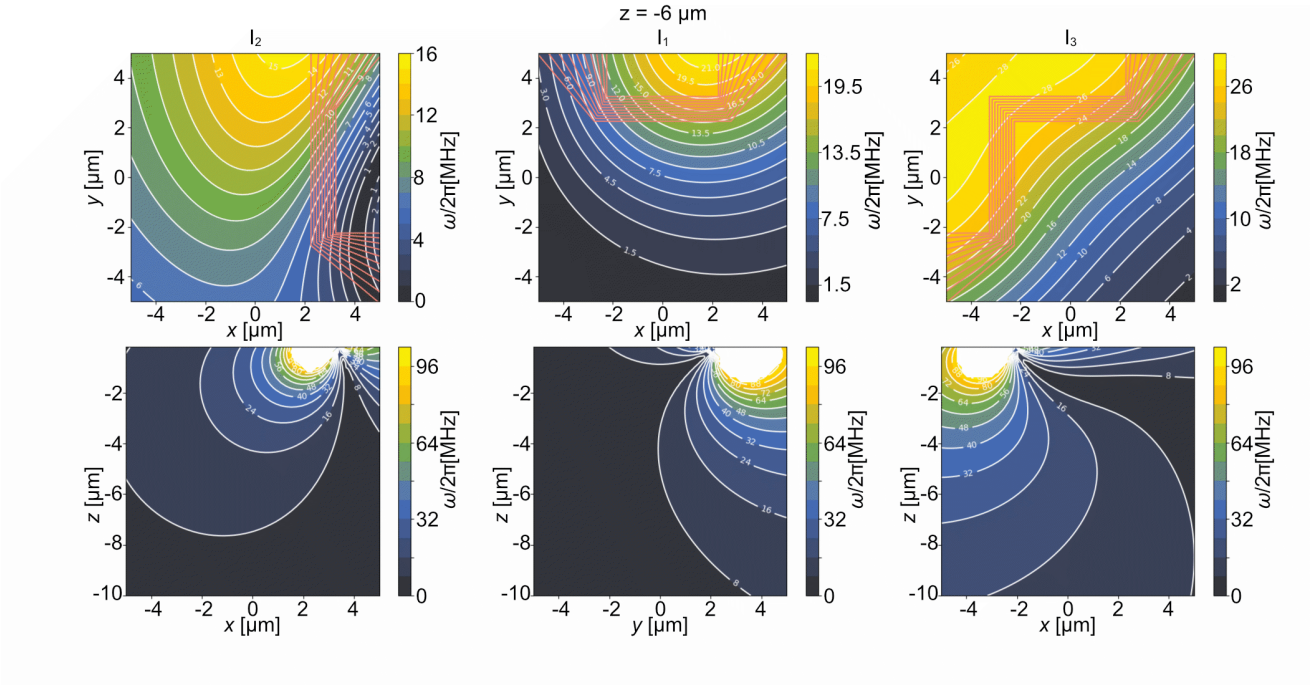
Supporting Information

SUPPLEMENTARY DISCUSSION

1. Magnetic gradient simulation and Gauss to MHz The magnetic field in the figure below is generated from 80 mA, as in the measurement presented in Fig. 4, running through the 5 µm arms of the U microstructure was simulated using Python library "Magpylib". Note that the current for Fig. 2 and Fig. 3 was 64 mA. The simulated area was 2 mm×2 mm large to include the influence of the larger feed lines connected to the U structure. The temperature of the wires was assumed to be constant because of the high heat conductivity of the diamond substrate. The 0.5 µm wide wires were divided into 10 subdivisions each to take their finite width into account. More subdivisions did not lead to a change in the outcome of the simulation. The simulation provided a 3D distribution of the magnetic field, i.e. $\mathbf{B}(x, y, z)$. To get the observed frequencies, the field $\mathbf{B}$ in every point in space was decomposed into parallel $B_{\parallel}$ and perpendicular $B_{\perp}$ component with respect to the NV orientation (-1, 1, 1 in our case). We calculate the transition frequencies by diagonalizing the Hamiltonian

$$\hat{H} = D\hat{S}_z^2 + \gamma_e B_0 \hat{S}_z + \gamma_e B_{\parallel} \hat{S}_z + \gamma_e B_{\perp} \cdot (\hat{S}_x \hat{e}_x + \hat{S}_y \hat{e}_y) \tag{1}$$

and taking the difference of its diagonal elements. Here, D and γ_e are the zero-field splitting and the gyromagnetic ratio, respectively. B_0 is the background magnetic field pointing along the z-axis. The simulation was repeated 3 times (for every one of the wires), an example of the simulation results is shown in supplementary fig. 1.



Supplementary Fig.1. Simulated observed frequencies in units of MHz. The first row of xy-plots from left to right shows the frequencies generated by I_2, I_1 and I_3, respectively, at a depth of 6 µm below the plane of the wires. The plot for I_2 on the left shows the location of the U microstructure as a grey overlay. The second row presents projections to the xz, yz, and xz-plane of the field from currents I_2, I_1, I_3, respectively, taken at $x = 0$ µm (or $y = 0$ µm).

2. From Hertz to meter We use the simulated magnetic field map to convert the frequency domain to a spatial domain. The simulation provides spatial distribution of observed frequencies, i.e. $\boldsymbol{\omega}(x, y, z)/2\pi$, where $\boldsymbol{\omega} = (\omega_1, \omega_2, \omega_3)$ are angular frequencies generated by every wire. To find the exact NV position, we matched the

simulated frequencies to the frequencies of the measured NV center to locate it in three dimensions. This was done by minimizing the sum of squared errors with a minimization algorithm (Nelder-Mead), using the physical position of the measurement point as an initial estimate. The algorithm converged to a point ≈ 6 µm below the Diamond surface (residual sum of squared error is 0 up to a numeric precision). This matches the depth measured optically with the confocal microscope. Supplementary fig. 1 displays the field value in units of MHz at a depth of 6 µm below the wires.

3. From Hertz to meter: resolution To find the resolution of the method, we need to know how uncertainty in frequency measurement translates into uncertainty of position. To do that, we calculated the Jacobian matrix of the $\boldsymbol{\omega}(x, y, z)/2\pi$ at the centroid of the NV cluster. The Jacobian, in our case, is a 3x3 matrix with units of [Hz/m] ([G/m]), representing how observed frequencies are affected by small changes in position. Even though we are not able to find the inverse of $\boldsymbol{\omega}(x, y, z)/2\pi$, according to the inverse function theorem, its Jacobian is equal to the inverse Jacobian of original mapping, which allows us to approximate it in the vicinity of NV cluster centroid $\mathbf{x}_0$ as

$$\mathbf{x} \approx \mathbf{x}_0 + J^{-1}(\boldsymbol{\omega} - \boldsymbol{\omega}_0)/2\pi \tag{2}$$

$$\Delta\mathbf{x} \approx J^{-1}\Delta\boldsymbol{\omega}/2\pi \tag{3}$$

Thus, for given uncertainty in frequency $\Delta\boldsymbol{\omega}/2\pi$, uncertainty in real space is scaled by the inverse Jacobian. In our case, we defined uncertainty in frequency $\Delta\boldsymbol{\omega}/2\pi$ as FWHM of corresponding distribution, which is proportional to standard deviation σ (where the constant of proportionality depends on distribution assumption). Without assuming the exact distribution kind, we use FWHM instead of σ in the following calculations, which will also provide resulting uncertainty as FWHM. The covariance matrix of the random vector multiplied by a deterministic matrix is given by

$$\mathrm{cov}(\Delta\mathbf{x}) = \mathrm{cov}(J^{-1}\Delta\boldsymbol{\omega}/2\pi) = J^{-1}\mathrm{cov}(\Delta\boldsymbol{\omega}/2\pi)(J^{-1})^{\intercal} \tag{4}$$

Since currents in every wire are independent, $\mathrm{cov}(\Delta\boldsymbol{\omega}/2\pi)$ is a diagonal matrix with diagonal elements equal to $\Delta\omega_i^2/(2\pi)^2$. Then FWHM in real space is given by $\sqrt{\mathrm{diag}\,\mathrm{cov}(\Delta\mathbf{x})}$ (along x, y, z coordinate), or by $\sqrt{\lambda_i}$ where λ_i is i-th eigenvalue of $\mathrm{cov}(\Delta\mathbf{x})$ (along the principal axis of uncertainty ellipsoid). For frequency uncertainties (discussed below) equal to 45.6, 52.1, and 99.2 KHz respectively, corresponding real space uncertainties (principal axis of uncertainty ellipsoid) are 14.7, 9.9, and 5.9 nm. To estimate the uniformity of the field gradients, the calculations were repeated for 100 points in the volume around the cluster centroid, corresponding to the expected confocal volume (200x200x1000 nm). Standard deviations of uncertainties were found to be 1.89, 0.58 a 0.31 nm respectively, which shows validity of the constant gradient approximation.

To assess the uncertainty of position approximation through the inverse Jacobian, 1000 points were randomly sampled within the expected confocal volume. The position of each point in real space was determined using a minimization routine and estimated through the Jacobian. The relative uncertainty, defined as the difference between the estimated and actual positions divided by field of view was found to be below 3% for 300x300x300 nm.

4. Signal-to-noise ratio (SNR) The signal-to-noise ratio (SNR) is defined as the ratio of signal power to the power of the background. The power of the signal is calculated by integrating the spectrogram band between the two gray lines seen in Fig. 4 (in the main text) and subtracting the background from it. Here, the background is calculated by integrating the spectrogram band where there is no signal and rescaled it to account for the difference in band size between the two integrated windows. The power of the noise is calculated the same as the background, where the integral of the band outside that of the signal is taken.

5. SNR enhancement by L1 optimization

Performance of L1 optimization for SNR improvement was investigated (as shown in Figure 3 (c, e, g)). The core idea of this approach is noise suppression by exploiting the fact that the signal is sparse in frequency space. The algorithm has been implemented in the PyTorch library, which provides an autograd function for minimizing arbitrary loss functions using the gradient descent algorithm.

The optimization objective consists of two parts: minimization of the difference between the original frequency-domain data and the reconstructed data (reconstruction loss, $\mathcal{L}_{rec}$) and sparsity-inducing L1 regularization on real space data ($\mathcal{L}_{sp}$). For the input raw frequency-domain data $\omega/2\pi$, the losses and solution are given by:

$$\mathcal{L}_{rec} = ||\omega - \omega_{opt}|/2\pi|_2^2 \tag{5}$$

$$\mathcal{L}_{sp} = \Big|\Big|\text{abs}\big[\mathcal{F}(\omega_{opt}/2\pi)\big]\Big|\Big|_1/N \tag{6}$$

$$f_{opt} = \arg\min_{f_{opt}} \mathcal{L}_{rec} + \lambda\mathcal{L}_{sp} \tag{7}$$

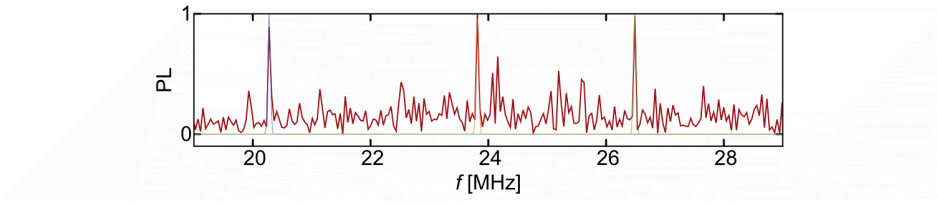
Here N denotes the length of the input data, $\mathcal{F}$ is the discrete Fourier transform operator (note that here direct Fourier transform converts frequency-space data into real space), λ controls the strength of regularization, the abs operator takes the element-wise absolute value of the complex vector, and ω_{opt} is the L1-optimized frequency-domain data, which is initialized to be equal to ω. The optimization required several thousand gradient descent iterations (with a step size set to $0.001N$ and λ set to 6) to converge. The final images show $\text{abs}\big[\mathcal{F}(y_{opt})\big]$.

6. Frequency resolution estimate: time vs frequency space We estimate the resolution of the measurement using the decay time of the signal $T_{2,I}$ rather than fitting the peaks in the frequency domain. The reason for not fitting the frequency domain data is ill-posed boundary conditions. The width of the peaks is on the same order of magnitude as the widths of the frequency bins, this means that the position of the width of the bins varies slightly (due to changes in the time domain bin size or/and number). This strong dependence of the peak width on the binning parameters makes it a bad candidate for estimating the resolution. On the other hand, the signal decay as a function of the applied current ($T_{2,I}$) is not prone to variation in the binning, (To see how we calculate the resolution in frequency space from $T_{2,I}$ refer to the main text). To strengthen our claim we plotted a Gaussian with an FWHM equal to the resolution we extracted on top of the frequency domain signal, see supplementary fig. 2. The figure demonstrates the agreement between the frequency domain signal and the fit, showing that calculating the resolution as a function of T_2 is valid in our case.

7. Frequency resolution estimate: influence of signal envelope The frequency resolution of the method is limited by the decay of the signal, and, in general, is inversely proportional to the lifetime $\Delta f = k/T_2$. The constant of proportionality k is given by the exact shape of decay, which in this case is assumed to be Gaussian:

$$S_z(\tau) = \cos(\omega\tau)e^{-\frac{1}{2}(\frac{\tau}{\sigma})^2} \tag{8}$$

Since only the $\tau > 0$ half of the Gaussian envelope is observed, analytical solution for the k is difficult, thus numerical simulation was performed instead. The idea of simulation is to extract the



Supplementary Fig.2. benchmarking the Resolution definition. The figure shows the frequency domain signal (red) and Gaussian plots (blue, orange, and green) with the FWHM equal to the resolution extracted from the T_2 decay of the time domain signal. The fit between the frequency domain signal and the Gaussians shows that calculating resolution from T_2 is valid in our case.

FWHM of the peak in frequency space and relate it to the $\frac{1}{T_2}$, manually finding a constant until both coincide. The code listing is given below. It was found that for the given signal model the $k = \frac{\sqrt{2}}{\pi}$

Listing 1. Peak width simulation

```
import numpy as np
import matplotlib.pyplot as plt
import scipy.signal

t = np.linspace(0, 2000, 50000) # us
f_max = 1 / (t[1] - t[0]) # MHz
T2_s = np.arange(2, 20) # T2 time
freqs = np.linspace(0, f_max, len(t)) # fft frequencies
df = freqs[1] - freqs[0]

def model(sigma): # signal model, cosine weightes by gaussian envelope
    return np.cos(10*np.pi*t) * np.exp((-1/2)*((t/sigma)**2))

widths = []
for t2 in T2_s:
    y = model(t2) # we define T2 as std of gaussian envelope
    spectrum = np.abs(np.fft.fft(y))[:len(t)//2]**2
    width = scipy.signal.find_peaks(spectrum,width=(None,None))[1]['widths'][0]
    widths.append(width)

widths = np.array(widths) * df # need to multiple by df to get MHz from pixels
k = np.sqrt(2) / np.pi # educated guess

plt.plot(T2_s, k/T2_s, "o-")
plt.plot(T2_s, widths, "o-")
plt.xlabel("T2, us")
plt.ylabel("Peak width, MHz")
```

8. Figures and data acquisition setup We use compress sensing to overcome the acquisition limits of our experimental setup. to give a feel of this we present below in supplementary Table.I the number of k-space points, repetitions, and total measurement time for the data presented in this work.

Figure	quadrature	k-space voxels	averages/point	measurement time [hours]
Fig. 2	2	$100 \times 100 \times 100$	1002	69
Fig. 3	2	$100 \times 100 \times 1$	50050	16
Fig. 4	1	$40 \cdot 10^3 \times 1 \times 1$	100100	95

Supplementary TABLE I. Measurement's setup of presented data. Note that the doubling of the number of k-space points for Fig. 2 and Fig. 3 refers to the sequence ending with $\pi/2_x$ and $\pi/2_y$.

5.4 Author contributions to individual articles

ChiSCAT: Unsupervised Learning of Recurrent Cellular Micromotion

- **Experiment design:** participated in experiments design
- **Cell biology**: performed majority of cell-related work with supplied differentiated cardiomyocytes
- **Experimental setup and data collection**: constructed the experimental setup from scratch, wrote control code, performed measurements, and collected data
- **Computing and analysis**: constructed computing infrastructure, developed and implemented the data processing algorithm, performed data analysis
- **Manuscript:** drafted the manuscript and contributed to revisions (80% of writing)

When can we see micromotion? Experimental and theoretical analysis of the ChiSCAT scheme

- **Experiment design:** participated in experiments design
- **Cell biology**: performed majority of cell-related work with supplied differentiated neurons
- **Experimental setup and data collection:** performed measurements and collected data
- **Computing and analysis:** processed collected data
- **Theory**: defined the models and derived the main theoretical conclusions, wrote the numerical simulation code
- **Manuscript**: drafted the manuscript (90% of writing).

Three-dimensional magnetic resonance tomography with sub-10 nanometer resolution

- **Experimental setup and data collection:** suggested and implemented experimental setup improvement (including control code), participated in data collection strategy development, participated in setup debugging

- **Computing and analysis**: developed theory of using aliasing as alternative to compressed sensing, developed the data processing algorithm, performed data analysis (including writing code for magnetic field simulation and final NV localization)
- **Manuscript:** participated in manuscript drafting (section "Spatial resolution"), drafted data analysis part (majority of supporting information)

References

[1] B. C. Abbott, A. V. Hill, et al. The positive and negative heat production associated with a nerve impulse. *Proceedings of the Royal Society of London. Series B-Biological Sciences*, 148(931):149–187, 1958.

[2] B. P. Abbott, R. Abbott, et al. Observation of gravitational waves from a binary black hole merger. *Phys. Rev. Lett.*, 116:061102, Feb 2016.

[3] M. Aharon, M. Elad, et al. K-svd : An algorithm for designing of overcomplete dictionaries for sparse representation. 2005.

[4] N. Aharon, A. Rotem, et al. Nv center based nano-nmr enhanced by deep learning. *Scientific Reports*, 9, 2018.

[5] A. N. Akansu and R. A. Haddad. *Multiresolution signal decomposition: transforms, subbands, and wavelets*. Academic press, 2001.

[6] B. Ans, J. Hérault, et al. Architectures neuromimétiques adaptatives: Détection de primitives. *Proceedings of Cognitiva*, 85:593–597, 1985.

[7] K. Arai, C. Belthangady, et al. Fourier magnetic imaging with nanoscale resolution and compressed sensing speed-up using electronic spins in diamond. *Nature nanotechnology*, 10(10):859–864, 2015.

[8] Y. Artzi, O. Zgadzai, et al. Three-dimensional fourier imaging of thousands of individual solid-state quantum bits–a tool for spin-based quantum technology. *Physica Scripta*, 98(3):035815, 2023.

[9] F. R. Bach and M. I. Jordan. Kernel independent component analysis. *2003 IEEE International Conference on Acoustics, Speech, and Signal Processing, 2003. Proceedings. (ICASSP '03).*, 4:IV–876, 2003.

[10] G. Balasubramanian, I. Chan, et al. Nanoscale imaging magnetometry with diamond spins under ambient conditions. *Nature*, 455(7213):648–651, 2008.

[11] M. K. Baller, M. K. Baller, et al. A cantilever array-based artificial nose. *Ultramicroscopy*, 82 1-4:1–9, 2000.

[12] R. Baraniuk. Compressive sensing. In *Computer Vision, A Reference Guide*. 2008.

[13] S. Batabyal, S. Satpathy, et al. Label-free optical detection of action potential in mammalian neurons. *Biomedical optics express*, 8 8:3700–3713, 2017.

[14] J. Bereiter-Hahn, C. H. Fox, et al. Quantitative reflection contrast microscopy of living cells. *The Journal of Cell Biology*, 82:767 – 779, 1979.

[15] P. A. Bottomley, H. Hart Jr, et al. Anatomy and metabolism of the normal human brain studied by magnetic resonance at 1.5 tesla. *Radiology*, 150(2):441–446, 1984.

[16] P.-T. Bremer, D. Maljovec, et al. Nd^ 2 av nd 2 av: N-dimensional data analysis and visualization analysis for the national ignition campaign. *Computing and Visualization in Science*, 17:1–18, 2015.

[17] R. Bridson. Fast poisson disk sampling in arbitrary dimensions. *SIGGRAPH sketches*, 10(1):1, 2007.

[18] J. H. Bruning, D. R. Herriott, et al. Digital wavefront measuring interferometer for testing optical surfaces and lenses. *Applied optics*, 13(11):2693–2703, 1974.

[19] R. Budakian, A. Finkler, et al. Roadmap on nanoscale magnetic resonance imaging. *Nanotechnology*, 2024.

[20] J. S. Bunch, A. M. Van Der Zande, et al. Electromechanical resonators from graphene sheets. *Science*, 315(5811):490–493, 2007.

[21] C. F. Caiafa and A. Cichocki. Multidimensional compressed sensing and their applications. *Wiley Interdisciplinary Reviews: Data Mining and Knowledge Discovery*, 3(6):355–380, 2013.

[22] F. Camastra and A. Vinciarelli. *Machine learning for audio, image and video analysis: theory and applications*. Springer, 2015.

[23] E. J. Candes, J. K. Romberg, et al. Stable signal recovery from incomplete and inaccurate measurements. *Communications on Pure and Applied Mathematics: A Journal Issued by the Courant Institute of Mathematical Sciences*, 59(8):1207–1223, 2006.

[24] G. Carleo, I. Cirac, et al. Machine learning and the physical sciences. *Reviews of Modern Physics*, 91(4):045002, 2019.

[25] F. Castells, P. Laguna, et al. Principal component analysis in ecg signal processing. *EURASIP Journal on Advances in Signal Processing*, 2007:1–21, 2007.

[26] E. F. Castillo and J. M. Gutiérrez. Nonlinear time series modeling and prediction using functional networks. extracting information masked by chaos. *Physics Letters A*, 244:71–84, 1998.

[27] H. Cecotti and A. Gräser. Convolutional neural network with embedded fourier transform for eeg classification. *2008 19th International Conference on Pattern Recognition*, pp. 1–4, 2008.

[28] S.-h. Chao, W. M. Dougherty, et al. Nanometer-scale magnetic resonance imaging. *Review of Scientific Instruments*, 75(5):1175–1181, 2004.

[29] H. Chen, D. Garcia-Gonzalez, et al. Computational model of the mechano-electrophysiological coupling in axons with application to neuromodulation. *Physical Review E*, 99(3):032406, 2019.

[30] H.-Y. Chen, C. B. Wilson, et al. Enhanced spatial resolution in magnetic resonance imaging by dynamic nuclear polarization at 5 k. *Proceedings of the National Academy of Sciences*, 119(22):e2201644119, 2022.

[31] A. Chichocki, Y. Li, et al. Beyond ica: Robust sparse signal representations. In *2004 IEEE International Symposium on Circuits and Systems (ISCAS)*, vol. 5, pp. V–V. IEEE, 2004.

[32] W. Choi, C. Fang-Yen, et al. Tomographic phase microscopy. *Nature methods*, 4(9):717–719, 2007.

[33] U. CMA. Ai foundation models: Initial report, 2023.

[34] L. B. Cohen, R. Keynes, et al. Light scattering and birefringence changes during nerve activity. *Nature*, 218(5140):438–441, 1968.

[35] L. B. Cohen, R. D. Keynes, et al. Changes in axon light scattering that accompany the action potential: current-dependent components. *The Journal of Physiology*, 224, 1972.

[36] —. Changes in light scattering that accompany the action potential in squid giant axons: potential-dependent components. *The Journal of Physiology*, 224, 1972.

[37] J. W. Cooley and J. W. Tukey. An algorithm for the machine calculation of complex fourier series. *Mathematics of computation*, 19(90):297–301, 1965.

[38] T. R. Corle. Submicron metrology in the semiconductor industry. *Solid-state electronics*, 35(3):391–402, 1992.

[39] A. Curtis. The mechanism of adhesion of cells to glass: a study by interference reflection microscopy. *The Journal of cell biology*, 20(2):199–215, 1964.

[40] W. Dai and O. Milenkovic. Subspace pursuit for compressive sensing: Closing the gap between performance and complexity. *arXiv preprint arXiv:0803.0811*, 803, 2008.

[41] M. A. Davenport, P. T. Boufounos, et al. Signal processing with compressive measurements. *IEEE Journal of Selected Topics in Signal Processing*, 4:445–460, 2010.

[42] C. Degen, M. Poggio, et al. Nanoscale magnetic resonance imaging. *Proceedings of the National Academy of Sciences*, 106(5):1313–1317, 2009.

[43] S. J. DeVience, L. M. Pham, et al. Nanoscale nmr spectroscopy and imaging of multiple nuclear species. *Nature nanotechnology*, 10(2):129–134, 2015.

[44] T. A. Dickinson, K. L. Michael, et al. Convergent, self-encoded bead sensor arrays in the design of an artificial nose. *Analytical chemistry*, 71 11:2192–8, 1999.

[45] C. Ding, X. He, et al. On the equivalence of nonnegative matrix factorization and spectral clustering. In *Proceedings of the 2005 SIAM international conference on data mining*, pp. 606–610. SIAM, 2005.

[46] F. Dolde, H. Fedder, et al. Electric-field sensing using single diamond spins. *Nature Physics*, 7(6):459–463, 2011.

[47] D. L. Donoho. Sparse solution of underdetermined linear equations by stagewise orthogonal matching pursuit. 2006.

[48] P. J. Durka, A. Matysiak, et al. Multichannel matching pursuit and eeg inverse solutions. *Journal of neuroscience methods*, 148(1):49–59, 2005.

[49] C. Edwards, A. Arbabi, et al. Optically monitoring and controlling nanoscale topography during semiconductor etching. *Light: Science & Applications*, 1(9):e30–e30, 2012.

[50] A. El Hady and B. B. Machta. Mechanical surface waves accompany action potential propagation. *Nature communications*, 6(1):6697, 2015.

[51] K. Engan, S. O. Aase, et al. Method of optimal directions for frame design. *1999 IEEE International Conference on Acoustics, Speech, and Signal Processing. Proceedings. ICASSP99 (Cat. No.99CH36258)*, 5:2443–2446 vol.5, 1999.

[52] R. Fisher. Linear discriminant analysis. *Ann. Eugenics*, 7(0):179, 1936.

[53] D. Foster and S. Seeley. Automatic tuning, simplified circuits, and design practice. *Proceedings of the Institute of Radio Engineers*, 25(3):289–313, 1937.

[54] M. Friedewald. Telefunken vs. marconi, or the race for wireless telegraphy at sea, 1896-1914. *Marconi, or the Race for Wireless Telegraphy at Sea*, 1914:2012, 2014.

[55] T. D. Gebhard, N. Kilbertus, et al. Convolutional neural networks: a magic bullet for gravitational-wave detection? *ArXiv*, abs/1904.08693, 2019.

[56] D. George and E. A. Huerta. Deep learning for real-time gravitational wave detection and parameter estimation with advanced ligo data. *ArXiv*, abs/1711.03121, 2017.

[57] —. Deep learning for real-time gravitational wave detection and parameter estimation: Results with advanced ligo data. *Physics Letters B*, 778:64–70, 2018.

[58] O. Gingerich. *The Eye of Heaven: Ptolemy, Copernicus, Kepler*. No. 66. Springer, 1993.

[59] O. Gingerich and A. Van Helden. How galileo constructed the moons of jupiter. *Journal for the History of Astronomy*, 42(2):259–264, 2011.

[60] P. Goupillaud, A. Grossmann, et al. Cycle-octave and related transforms in seismic signal analysis. *Geoexploration*, 23(1):85–102, 1984.

[61] J. Griesbauer, S. Bössinger, et al. Propagation of 2d pressure pulses in lipid monolayers and its possible implications for biology. *Physical Review Letters*, 108(19):198103, 2012.

[62] E. Griffith and C. Metz. A new area of ai booms, even amid the tech gloom. *New York Times, January*, 7, 2023.

[63] M. Grinolds, M. Warner, et al. Subnanometre resolution in three-dimensional magnetic resonance imaging of individual dark spins. *Nature nanotechnology*, 9(4):279–284, 2014.

[64] A. Grinvald, E. E. Lieke, et al. Functional architecture of cortex revealed by optical imaging of intrinsic signals. *Nature*, 324:361–364, 1986.

[65] U. Grob, M.-D. Krass, et al. Magnetic resonance force microscopy with a one-dimensional resolution of 0.9 nanometers. *Nano letters*, 19(11):7935–7940, 2019.

[66] C. Grojean, A. Paul, et al. Lessons on interpretable machine learning from particle physics. *Nature Reviews Physics*, 4(5):284–286, 2022.

[67] D. Gross, W. S. Williams, et al. Theory of electromechanical effects in nerve. *Cellular and Molecular Neurobiology*, 3:89–111, 1983.

[68] M. Guarascio, G. Folino, et al. A machine learning approach for rainfall estimation integrating heterogeneous data sources. *IEEE Transactions on Geoscience and Remote Sensing*, 60:1–11, 2020.

[69] A. Gulati, J. Qin, et al. Conformer: Convolution-augmented transformer for speech recognition. *ArXiv*, abs/2005.08100, 2020.

[70] M. G. Gustafsson, L. Shao, et al. Three-dimensional resolution doubling in wide-field fluorescence microscopy by structured illumination. *Biophysical journal*, 94(12):4957–4970, 2008.

[71] H. Haas, S. Tabatabaei, et al. Nuclear magnetic resonance diffraction with subangstrom precision. *Proceedings of the National Academy of Sciences*, 119(40):e2209213119, 2022.

[72] T. Häberle, D. Schmid-Lorch, et al. Nanoscale nuclear magnetic imaging with chemical contrast. *Nature nanotechnology*, 10(2):125–128, 2015.

[73] J. Harden, N. Diorio, et al. Chirality of lipids makes fluid lamellar phases piezoelectric. *Physical Review E—Statistical, Nonlinear, and Soft Matter Physics*, 79(1):011701, 2009.

[74] Y. He, X. Wang, et al. Classification of attention deficit/hyperactivity disorder based on eeg signals using a eeg-transformer model. *Journal of Neural Engineering*, 20, 2023.

[75] T. Heimburg and A. D. Jackson. On soliton propagation in biomembranes and nerves. *Proceedings of the National Academy of Sciences*, 102(28):9790–9795, 2005.

[76] H. Hertz. *Electric waves: being researches on the propagation of electric action with finite velocity through space*. Dover Publications, 1893.

[77] A. Hewish, S. J. Bell, et al. Observation of a rapidly pulsating radio source. In *A Source Book in Astronomy and Astrophysics, 1900–1975*, pp. 498–504. Harvard University Press, 1979.

[78] D. Hill and R. Keynes. Opacity changes in stimulated nerve. *The Journal of physiology*, 108(3):278, 1949.

[79] A. L. Hodgkin and A. F. Huxley. Action potentials recorded from inside a nerve fibre. *Nature*, 144:710–711, 1939.

[80] K. Holthoff, H.-U. Dodt, et al. Changes in intrinsic optical signal of rat neocortical slices following afferent stimulation. *Neuroscience Letters*, 180:227–230, 1994.

[81] P. Hosseini, R. Zhou, et al. Pushing phase and amplitude sensitivity limits in interferometric microscopy. *Optics letters*, 41(7):1656–1659, 2016.

[82] H. Hotelling. Analysis of a complex of statistical variables into principal components. *Journal of Educational Psychology*, 24:498–520, 1933.

[83] C. Hu and G. Popescu. Physical significance of backscattering phase measurements. *Optics Letters*, 42(22):4643–4646, 2017.

[84] Y. H. Hu, W. J. Tompkins, et al. Applications of artificial neural networks for ecg signal detection and classification. *Journal of electrocardiology*, 26 Suppl:66–73, 1993.

[85] D. Huang, E. A. Swanson, et al. Optical coherence tomography. *Science*, 254(5035):1178–1181, 1991.

[86] K. Iwasa, I. Tasaki, et al. Swelling of nerve fibers associated with action potentials. *Science*, 210(4467):338–339, 1980.

[87] B. Jawerth and W. Sweldens. An overview of wavelet based multiresolution analyses. *SIAM review*, 36(3):377–412, 1994.

[88] S. J. Julier and J. K. Uhlmann. New extension of the kalman filter to nonlinear systems. In *Signal processing, sensor fusion, and target recognition VI*, vol. 3068, pp. 182–193. Spie, 1997.

[89] T.-P. Jung, T.-P. Jung, et al. Removing electroencephalographic artifacts by blind source separation. *Psychophysiology*, 37 2:163–78, 2000.

[90] R. E. Kalman. A new approach to linear filtering and prediction problems. *Journal of Basic Engineering*, 82(1):35–45, 03 1960. ISSN 0021-9223.

[91] R. E. Kálmán and R. S. Bucy. New results in linear filtering and prediction theory. *Journal of Basic Engineering*, 83:95–108, 1961.

[92] M. E. Kandel, C. Hu, et al. Epi-illumination gradient light interference microscopy for imaging opaque structures. *Nature communications*, 10(1):4691, 2019.

[93] R. Kazama, K. Sekine, et al. Compressed sensing in magnetic resonance imaging using non-randomly under-sampled signal in cartesian coordinates. *IEICE TRANSACTIONS on Information and Systems*, 102(9):1851–1859, 2019.

[94] G. Kim, P. Kosterin, et al. A mechanical spike accompanies the action potential in mammalian nerve terminals. *Biophysical journal*, 92(9):3122–3129, 2007.

[95] K. H. Kim and S. J. Kim. Neural spike sorting under nearly 0-db signal-to-noise ratio using nonlinear energy operator and artificial neural-network classifier. *IEEE Transactions on Biomedical Engineering*, 47:1406–1411, 2000.

[96] P. Kukura, H. Ewers, et al. High-speed nanoscopic tracking of the position and orientation of a single virus. *Nature methods*, 6(12):923–927, 2009.

[97] G. Lai and T. Yatagai. Generalized phase-shifting interferometry. *JOSA A*, 8(5):822–827, 1991.

[98] P. Langehanenberg, B. Kemper, et al. Autofocusing in digital holographic phase contrast microscopy on pure phase objects for live cell imaging. *Applied optics*, 47(19):D176–D182, 2008.

[99] A. S. Lapedes and R. M. Farber. Nonlinear signal processing using neural networks: Prediction and system modelling. 1987.

[100] T.-W. Lee and T.-W. Lee. *Independent component analysis*. Springer, 1998.

[101] A. T. Lefebvre, C. L. Rodriguez, et al. High-resolution transcranial optical imaging of in vivo neural activity. *Scientific Reports*, 14(1):24756, 2024.

[102] R. Legin, A. Adam, et al. Beyond gaussian noise: A generalized approach to likelihood analysis with non-gaussian noise. *The Astrophysical Journal Letters*, 949(2):L41, 2023.

[103] R. M. Lerner. Band-pass filters with linear phase. *Proceedings of the IEEE*, 52(3):249–268, 1964.

[104] H. Leuchtag and H. Fishman. The nonlinear kinetics of an electrodiffusion membrane. *Structure and Function in Excitable Cells*, pp. 415–434, 1983.

[105] H. R. Leuchtag. Indications of the existence of ferroelectric units in excitable-membrane channels. *Journal of theoretical biology*, 127 3:321–40, 1987.

[106] G. Li and J. J. Jung. Deep learning for anomaly detection in multivariate time series: Approaches, applications, and challenges. *Information Fusion*, 91:93–102, 2023.

[107] J. Lien, L. I. G. Olascoaga, et al. A phenomenological ai foundation model for physical signals. 2024.

[108] T. Ling, K. C. Boyle, et al. Full-field interferometric imaging of propagating action potentials. *Light, Science & Applications*, 7, 2018.

[109] —. High-speed interferometric imaging reveals dynamics of neuronal deformation during the action potential. *Proceedings of the National Academy of Sciences*, 117(19):10278–10285, 2020.

[110] G. Liu, M. Chen, et al. Repetitive readout enhanced by machine learning. *Machine Learning: Science and Technology*, 1, 2019.

[111] S. Liu, B. Chen, et al. Compressive confocal microscopy imaging at the single-photon level with ultra-low sampling ratios. *Communications Engineering*, 3(1):88, 2024.

[112] M. Lustig, D. L. Donoho, et al. Sparse mri: The application of compressed sensing for rapid mr imaging. *Magnetic Resonance in Medicine*, 58, 2007.

[113] Luxima Technology LLC. LUXIMA™ LUX330 Image Sensor: High-Speed Global Shutter CMOS Digital Sensor, October 2016. LUX330 brief v1.1.

[114] O. V. Lyulko, G. Randers-Pehrson, et al. Immersion mirau interferometry for label-free live cell imaging in an epi-illumination geometry. In *Imaging, Manipulation, and Analysis of Biomolecules, Cells, and Tissues VIII*, vol. 7568, pp. 448–456. SPIE, 2010.

[115] B. A. Macvicar and D. Hochman. Imaging of synaptically evoked intrinsic optical signals in hippocampal slices. In *Journal of Neuroscience*. 1991.

[116] S. Makeig, A. J. Bell, et al. Independent component analysis of electroencephalographic data. In *Neural Information Processing Systems*. 1995.

[117] S. Mallat and Z. Zhang. Matching pursuits with time-frequency dictionaries. *IEEE Trans. Signal Process.*, 41:3397–3415, 1993.

[118] H. Mamin, M. Kim, et al. Nanoscale nuclear magnetic resonance with a nitrogen-vacancy spin sensor. *Science*, 339(6119):557–560, 2013.

[119] J. Marcum. A statistical theory of target detection by pulsed radar. *IRE Transactions on Information Theory*, 6(2):59–267, 1960.

[120] R. J. Marks. *Handbook of Fourier analysis & its applications*. Oxford University Press, 2009.

[121] J. R. Maze, P. L. Stanwix, et al. Nanoscale magnetic sensing with an individual electronic spin in diamond. *Nature*, 455(7213):644–647, 2008.

[122] C. Messick, K. Blackburn, et al. Analysis framework for the prompt discovery of compact binary mergers in gravitational-wave data. *Physical Review D*, 95:042001, 2016.

[123] S. Mika, G. Rätsch, et al. Fisher discriminant analysis with kernels. *Neural Networks for Signal Processing IX: Proceedings of the 1999 IEEE Signal Processing Society Workshop (Cat. No.98TH8468)*, pp. 41–48, 1999.

[124] M. Mishali and Y. C. Eldar. Blind multiband signal reconstruction: Compressed sensing for analog signals. *IEEE Transactions on Signal Processing*, 57:993–1009, 2007.

[125] E. Moore and R. Tycko. Micron-scale magnetic resonance imaging of both liquids and solids. *Journal of Magnetic Resonance*, 260:1–9, 2015.

[126] J. Moser, A. Eichler, et al. Nanotube mechanical resonators with quality factors of up to 5 million. *Nature nanotechnology*, 9(12):1007–1011, 2014.

[127] R. Nawaratne, D. Alahakoon, et al. Spatiotemporal anomaly detection using deep learning for real-time video surveillance. *IEEE Transactions on Industrial Informatics*, 16(1):393–402, 2019.

[128] T. D. Nguyen, N. Deshmukh, et al. Piezoelectric nanoribbons for monitoring cellular deformations. *Nature nanotechnology*, 7(9):587–593, 2012.

[129] T. D. Nguyen, S. Mao, et al. Nanoscale flexoelectricity. *Advanced Materials*, 25(7):946–974, 2013.

[130] J. M. Nichol, E. R. Hemesath, et al. Nanomechanical detection of nuclear magnetic resonance using a silicon nanowire oscillator. *Physical Review B—Condensed Matter and Materials Physics*, 85(5):054414, 2012.

[131] L. F. Nicolás-Alonso and J. G. Gil. Brain computer interfaces, a review. *Sensors (Basel, Switzerland)*, 12:1211 – 1279, 2012.

[132] G. Nomarski. [from phase contrast to contrast by interference]. *Revue d'hematologie*, 12 4:439–42, 1957.

[133] D. O. North. An analysis of the factors which determine signal/noise discrimination in pulsed-carrier systems. *Proceedings of the IEEE*, 51(7):1016–1027, 1963.

[134] H. Nyquist. Certain topics in telegraph transmission theory. *Transactions of the American Institute of Electrical Engineers*, 47(2):617–644, 1928.

[135] S. Oh, C. Fang-Yen, et al. Label-free imaging of membrane potential using membrane electromotility. *Biophysical journal*, 103 1:11–8, 2012.

[136] M. A. Osborne, S. J. Roberts, et al. Towards real-time information processing of sensor network data using computationally efficient multi-output gaussian processes. *2008 International Conference on Information Processing in Sensor Networks (ipsn 2008)*, pp. 109–120, 2008.

[137] B. J. Owen. Search templates for gravitational waves from inspiraling binaries: Choice of template spacing. *Physical Review D*, 53(12):6749, 1996.

[138] P. Paatero and U. Tapper. Positive matrix factorization: A non-negative factor model with optimal utilization of error estimates of data values. *Environmetrics*, 5(2):111–126, 1994.

[139] D. Patel, D. Canaday, et al. Using machine learning to predict statistical properties of non-stationary dynamical processes: System climate, regime transitions, and the effect of stochasticity. *Chaos: An Interdisciplinary Journal of Nonlinear Science*, 31(3), 2021.

[140] S. Pezzagna and J. Meijer. Quantum computer based on color centers in diamond. *Applied Physics Reviews*, 8(1), 2021.

[141] J. Pine and G. Chow. Moving live dissociated neurons with an optical tweezer. *IEEE Transactions on Biomedical Engineering*, 56(4):1184–1188, 2008.

[142] T. Polischuk, C. R. Jarvis, et al. Intrinsic optical signaling denoting neuronal damage in response to acute excitotoxic insult by domoic acid in the hippocampal slice. *Neurobiology of Disease*, 4:423–437, 1998.

[143] G. Popescu and Y. Park. Quantitative phase imaging in biomedicine. *2012 Conference on Lasers and Electro-Optics (CLEO)*, pp. 1–1, 2012.

[144] G. Popescu, Y. Park, et al. Imaging red blood cell dynamics by quantitative phase microscopy. *Blood Cells, Molecules, and Diseases*, 41(1):10–16, 2008.

[145] G. Puentes, G. Waldherr, et al. Efficient route to high-bandwidth nanoscale magnetometry using single spins in diamond. *Scientific reports*, 4(1):4677, 2014.

[146] H. Purwins, B. Li, et al. Deep learning for audio signal processing. *IEEE Journal of Selected Topics in Signal Processing*, 13:206–219, 2019.

[147] P. Qian, X. Lin, et al. Machine-learning-assisted electron-spin readout of nitrogen-vacancy center in diamond. *Applied Physics Letters*, 118:084001, 2021.

[148] D. M. Rector, K. Carter, et al. Spatio-temporal mapping of rat whisker barrels with fast scattered light signals. *NeuroImage*, 26:619–627, 2005.

[149] D. M. Rector, R. F. Rogers, et al. Scattered-light imaging in vivo tracks fast and slow processes of neurophysiological activation. *NeuroImage*, 14:977–994, 2001.

[150] W. Rose, H. Haas, et al. High-resolution nanoscale solid-state nuclear magnetic resonance spectroscopy. *Physical Review X*, 8(1):011030, 2018.

[151] N. Rossi, F. R. Braakman, et al. Vectorial scanning force microscopy using a nanowire sensor. *Nature nanotechnology*, 12(2):150–155, 2017.

[152] Y. Roy, H. J. Banville, et al. Deep learning-based electroencephalography analysis: a systematic review. *Journal of Neural Engineering*, 16, 2019.

[153] D. Rugar, H. Mamin, et al. Proton magnetic resonance imaging using a nitrogen–vacancy spin sensor. *Nature nanotechnology*, 10(2):120–124, 2015.

[154] D. Rugar, C. Yannoni, et al. Mechanical detection of magnetic resonance. *Nature*, 360(6404):563–566, 1992.

[155] D. Rugar, O. Züģer, et al. Force detection of nuclear magnetic resonance. *Science*, 264:1560 – 1563, 1994.

[156] D. E. Rumelhart, G. E. Hinton, et al. Learning representations by back-propagating errors. *Nature*, 323:533–536, 1986.

[157] M. M. Rvachev. On axoplasmic pressure waves and their possible role in nerve impulse propagation. *Biophysical Reviews and Letters*, 5(02):73–88, 2010.

[158] B. M. Salzberg, A. L. Obaid, et al. Large and rapid changes in light scattering accompany secretion by nerve terminals in the mammalian neurohypophysis. *The Journal of General Physiology*, 86:395 – 411, 1985.

[159] S. Sanei and J. A. Chambers. *EEG signal processing*. John Wiley & Sons, 2013.

[160] V. Sazonova, Y. Yaish, et al. A tunable carbon nanotube electromechanical oscillator. *Nature*, 431(7006):284–287, 2004.

[161] B. Scholkopf, A. Smola, et al. Nonlinear component analysis as a kernel eigenvalue problem. *Neural Computation*, 10:1299–1319, 1998.

[162] R. S. Shankland. Michelson-Morley experiment. *American Journal of Physics*, 32(1):16–35, 1964.

[163] C. E. Shannon. A mathematical theory of communication. *The Bell system technical journal*, 27(3):379–423, 1948.

[164] —. Communication in the presence of noise. *Proceedings of the IRE*, 37(1):10–21, 1949.

[165] J. Sidles. Noninductive detection of single-proton magnetic resonance. *Applied Physics Letters*, 58(24):2854–2856, 1991.

[166] A. Stakia, T. Dorigo, et al. Advances in multi-variate analysis methods for new physics searches at the large hadron collider. *Reviews in Physics*, 7:100063, 2021.

[167] T. Staudacher, F. Shi, et al. Nuclear magnetic resonance spectroscopy on a (5-nanometer) 3 sample volume. *Science*, 339(6119):561–563, 2013.

[168] R. Stepnoski, A. Laporta, et al. Noninvasive detection of changes in membrane potential in cultured neurons by light scattering. *Proceedings of the National Academy of Sciences of the United States of America*, 88:9382 – 9386, 1991.

[169] P. Stoica, R. L. Moses, et al. *Spectral analysis of signals*, vol. 452. Pearson Prentice Hall Upper Saddle River, NJ, 2005.

[170] M. T. Amawi, A. Trelin, et al. Three-dimensional magnetic resonance tomography with sub-10 nanometer resolution. *npj Quantum Information*, 10(1):16, 2024.

[171] P. Tagare. Signal averaging. 1993.

[172] I. Tasaki and K. H. Iwasa. Rapid pressure changes and surface displacements in the squid giant axon associated with production of action potentials. *The Japanese journal of physiology*, 32 1:69–81, 1982.

[173] I. Tasaki, K. Kusano, et al. Rapid mechanical and thermal changes in the garfish olfactory nerve associated with a propagated impulse. *Biophysical journal*, 55(6):1033–1040, 1989.

[174] I. Tasaki and T. Nakaye. Heat generated by the dark-adapted squid retina in response to light pulses. *Science*, 227 4687:654–5, 1985.

[175] Teledyne Princeton Instruments. *BLAZE: Revolutionary High-Speed Cameras for Spectroscopy*, 2017. RevA3.

[176] S. Terakawa. Changes in intracellular pressure in squid giant axons associated with production of action potentials. *Biochemical and biophysical research communications*, 114 3:1006–10, 1983.

[177] —. Potential-dependent variations of the intracellular pressure in the intracellularly perfused squid giant axon. *The Journal of Physiology*, 369, 1985.

[178] K. R. Thurber, L. E. Harrell, et al. 170nm nuclear magnetic resonance imaging using magnetic resonance force microscopy. *Journal of Magnetic Resonance*, 162(2):336–340, 2003.

[179] L. Trachsel, H.-U. Dodt, et al. The intrinsic optical signal evoked by chiasm stimulation in the rat suprachiasmatic nuclei exhibits gabaergic day-night variation. *European Journal of Neuroscience*, 8, 1996.

[180] A. Trelin, J. Abel, et al. When can we see micromotion? experimental and theoretical analysis of the chiscat scheme. 2024.

[181] A. Trelin, S. Kussauer, et al. Chiscat: Unsupervised learning of recurrent cellular micromotion patterns from a chaotic speckle pattern. *Nano Letters*, 24(40):12374–12381, 2024.

[182] J. A. Tropp and A. C. Gilbert. Signal recovery from random measurements via orthogonal matching pursuit. *IEEE Transactions on Information Theory*, 53:4655–4666, 2007.

[183] E. Trucco and K. Plakas. Video tracking: a concise survey. *IEEE Journal of oceanic engineering*, 31(2):520–529, 2006.

[184] S. Tsuji, T. Masumizu, et al. Magnetic resonance imaging of isolated single liposome by magnetic resonance force microscopy. *Journal of Magnetic Resonance*, 167(2):211–220, 2004.

[185] M. Tsukamoto, S. Ito, et al. Accurate magnetic field imaging using nanodiamond quantum sensors enhanced by machine learning. *Scientific Reports*, 12, 2022.

[186] V. Tsytsarev, K. Premachandra, et al. Imaging cortical electrical stimulation in vivo: fast intrinsic optical signal versus voltage-sensitive dyes. *Optics letters*, 33 9:1032–4, 2008.

[187] A. J. Van Der Veen, A. Leshem, et al. Array signal processing for radio astronomy. *Experimental Astronomy*, 17:231–249, 2004.

[188] R. van Schadewijk, J. R. Krug, et al. Mrm microcoil performance calibration and usage demonstrated on medicago truncatula roots at 22 t. *Journal of Visualized Experiments*, 2021(167):1–20, 2021.

[189] S. S. Vasanawala, M. Murphy, et al. Practical parallel imaging compressed sensing mri: Summary of two years of experience in accelerating body mri of pediatric patients. In *2011 ieee international symposium on biomedical imaging: From nano to macro*, pp. 1039–1043. IEEE, 2011.

[190] A. Vaswani, N. M. Shazeer, et al. Attention is all you need. In *Neural Information Processing Systems*. 2017.

[191] E. A. Wan and R. Van Der Merwe. The unscented kalman filter for nonlinear estimation. In *Proceedings of the IEEE 2000 adaptive systems for signal processing, communications, and control symposium (Cat. No. 00EX373)*, pp. 153–158. Ieee, 2000.

[192] A. WATANABE. Mechanical, thermal, and optical changes of the nerve membrane associated with excitation. *The Japanese Journal of Physiology*, 36(4):625–643, 1986.

[193] H. Weber, N. Baxan, et al. Microcoil-based mri: feasibility study and cell culture applications using a conventional animal system. *Magnetic Resonance Materials in Physics, Biology and Medicine*, 24:137–145, 2011.

[194] T. D. Weber, M. V. Moya, et al. High-speed multiplane confocal microscopy for voltage imaging in densely labeled neuronal populations. *Nature Neuroscience*, 26(9):1642–1650, 2023.

[195] J. A. Wepman. Analog-to-digital converters and their applications in radio receivers. *IEEE Communications magazine*, 33(5):39–45, 1995.

[196] J. B. West. Henry cavendish (1731–1810): hydrogen, carbon dioxide, water, and weighing the world. *American Journal of Physiology-Lung Cellular and Molecular Physiology*, 307(1):L1–L6, 2014.

[197] B. Widrow and M. E. Hoff. Adaptive switching circuits. 1988.

[198] N. Wiener. *Extrapolation, interpolation, and smoothing of stationary time series: with engineering applications*. The MIT press, 1949.

[199] Y. Yang, X.-W. Liu, et al. Imaging action potential in single mammalian neurons by tracking the accompanying sub-nanometer mechanical motion. *ACS nano*, 12(5):4186–4193, 2018.

[200] Z. Yang, X. Kong, et al. Two-dimensional nanoscale nuclear magnetic resonance spectroscopy enhanced by artificial intelligence. 2019.

[201] G. Young and P. Kukura. Interferometric scattering microscopy. *Annual review of physical chemistry*, 70(1):301–322, 2019.

[202] D. Yu and L. Deng. Deep learning and its applications to signal and information processing [exploratory dsp]. *IEEE Signal Processing Magazine*, 28:145–154, 2011.

[203] V. Zarzoso, A. K. Nandi, et al. Maternal and foetal ecg separation using blind source separation methods. *IMA journal of mathematics applied in medicine and biology*, 14 3:207–25, 1997.

[204] F. Zernike. Phase contrast, a new method for the microscopic observation of transparent objects part ii. *Physica*, 9(10):974–986, 1942.

[205] M. Zevin, S. B. Coughlin, et al. Gravity spy: integrating advanced ligo detector characterization, machine learning, and citizen science. *Classical and Quantum Gravity*, 34, 2016.

[206] P.-C. Zhang, A. M. Keleshian, et al. Voltage-induced membrane movement. *Nature*, 413(6854):428–432, 2001.

[207] Z. Zhang and S. Aeron. Denoising and completion of 3d data via multidimensional dictionary learning. *arXiv preprint arXiv:1512.09227*, 2015.

[208] H. Zou, T. Hastie, et al. Sparse principal component analysis. *Journal of computational and graphical statistics*, 15(2):265–286, 2006.

[209] O. Züger, S. Hoen, et al. Three-dimensional imaging with a nuclear magnetic resonance force microscope. *Journal of Applied Physics*, 79(4):1881–1884, 1996.

Acknowledgement

First of all, I want to thank my supervisor, Prof. Dr. Friedemann Reinhard, for giving me the chance to work on this challenging yet fascinating project. His scientific guidance and willingness to find solutions, even in difficult situations, were crucial throughout this journey. I'm also very grateful to my research group colleagues — Paul Weinbrenner, Mohammad Amawi, Francesco Poggiali, Nils Le Coutre, and You Huang — for their incredible scientific and personal support. They made this experience easier and more enjoyable. My thanks also go to the Regenerative Medicine in Cardiac Surgery research group for their helpful advices on the biology-related parts of this work. A big thank you to the team at the mechanical workshop of the Institute for Physics, especially its leader Paul Voss, for their invaluable help in solving technical issues and setting up the laboratory. I'm also thankful to Dr. Franklin Martinez for his initiative support in these efforts. I'd like to thank the University for its excellent infrastructure and supportive services, including the Welcome Center and the Physics Graduiertenkolleg. A special thanks to its speaker, Anna Julia Poser, for her many efforts to help me with both personal and organizational matters.

Lastly, I want to thank my family and friends for being there for me throughout this project. Above all, I'm especially grateful to my wife Olena, whose endless support gave me the strength and motivation to complete this work.